AIX MARSEILLE UNIVERSITÉ

ED 352 Physique et Sciences de la Matière

Laboratoire MAtériaux Divisés, Interfaces, Réactivité, ELectrochimie (MADIREL), UMR 7246

Thèse présentée pour obtenir le grade universitaire de docteur

Discipline: Matière Condensée et Nanosciences

Spécialité: Batterie lithium-ion

Alexander Teklit TESFAYE

STUDY AND IMPROVE THE ELECTROCHEMICAL BEHAVIOUR OF NEW NEGATIVE ELECTRODES FOR LI-ION BATTERIES

Soutenue le 14/11/2017 devant le jury:

Hervé MARTINEZ	Université de Pau	Rapporteur
Yair EIN-ELI	Technion-Israel Institute of Technology	Rapporteur
Christophe LETHIEN	Université de Lille 1	Examinateur
Florence VACANDIO	Aix-Marseile Université	Examinatrice
Sébastien MARIA	Aix-Marseille Université	Examinateur
Laure MONCONDUIT	Université de Montpellier	Examintarice
Thierry DJENIZIAN	École National Supérieure des Mines	Directeur de thèse

ACKNOWLEDGMENT

First of all, I would like to express my deepest appreciation to my supervisor Prof. Thierry Djenizian for his guidance, encouragement and providing me with great atmosphere for doing my thesis work. Without his suggestions and constructive critics, I would not have been able to successfully complete my PhD.

I would also like to thank my collaborators Prof. Yury Gogotsi from Drexel University and Prof. Jeff L. Coffer from Texas Christian University for helping and encouraging me during my study.

I would like to thank Dr. Florence Vacandio for teaching me how to perform sputtering experiment and Carine Chassigneux for XRD measurements and every member of MADIREL for their great assistance, kindness and moral support. I also would like to Dr. Renaud Denoyel and Marilyne Barbaroux for helping me settle during the beginning of the thesis work.

I would like to thank Dr. Maissa Barr from CINAM for her great assistance in TEM analysis and Dr. Frédéric Dumur from Institut de Chimie Radicalaire for giving me advices and knowledge about polymer synthesis.

Finally, I deeply appreciate my family. Special thanks go to Salemo, Yirgey and Yaya.

I would like to acknowledge the financial support from ALISTORE-ERI.

ABSTRACT

Currently, commercial lithium ion batteries (LIBs) use carbon based materials as negative electrode; however the technology is reaching its limit because of the low theoretical specific capacity (372 mAh g^{-1}). The objective of this thesis is to study the electrochemical behaviour of three different new high capacity anodes as alternative to graphite, identify the main parameters responsible for the capacity fading, and propose a versatile solution to improve their electrochemical performance.

First, Micron-sized SnSb alloy synthesized by microwave techniques has been investigated. The SnSb anode shows superior electrochemical properties, i.e. a large initial capacity (833 mAh g^{-1}) which is maintained up to 20 cycles. However, the capacity fade very quickly after the 25 cycles suggesting the disintegration of the electrode material due to the mechanical stress caused by the large volume change during lithium alloying/dealloying mechanism. Furthermore, the cracking of the electrode surface create new surfaces which lead to electrolyte decomposition to create solid electrolyte interphase (SEI) film. The loss of electrical contact and active material combined with formation of a passive layer are responsible for the overall poor electrochemical performance.

The second anode material was fabricated by anodization of Ti_3SiC_2 that led to the formation of a porous film containing anatase, a small quantity of free carbon, and silica. By varying the anodization parameters (anodization time, potential, and fluoride content in the aqueous electrolyte), various oxide morphologies were produced. After 140 cycles performed at multiple applied current densities, an areal capacity of 380 µAh cm^{-2} (C-rate of 200 µA cm^{-2}) has been obtained for Ti_3SiC_2 anodized at 60 V. The electrochemical performance has been enhanced by tailoring the morphological properties. Two typical porous structures, nanolayered and mesoporous, were produced at low and high applied potential, respectively. Compared to the mesoporous morphology obtained at 60 V, the power density delivered by the layered structure formed at 10 V is almost tripled. Cyclic voltammetry has been used to explain that this enhanced electrochemical property is related to the higher amount of lithium stored at the surface of the nanolayered structure. The large capacity loss observed after the first

cycle is attributed to the irreversible reaction of lithium ion with trace water molecules, lithium ion trapping within the structural defects of titania, and the formation of SEI layer.

The electrochemical performance of silicon nanotube vertical arrays has been also investigated. Porous silicon nanotubes were fabricated on stainless steel substrates using a sacrificial zinc oxide nanowire template method. The porous Si nanotubes electrode has shown superior discharge capacities and better cycling stability than some reported Si nanostructured anodes. A second discharge capacity of 3095 mAh g^{-1} with a coulombic efficiency of 63 % were attained at a rate of C/20 and a stable gravimetric capacity of 1670 mAh g^{-1} obtained after 30 cycles. This is attributed to the large surface area offered by the porosity of the 3D nanostructures, thereby promoting lithium-ion storage according to a pseudocapacitive mechanism. The capacity fading and the low initial coulombic efficiency is attributed to the formation of a SEI layer. In addition, the large volume change during alloying/dealloying results in the partial detachment of the nanotubes.

These three electrode materials exhibit good electrochemical performance which makes them promising candidates to replace carbon as a negative electrode for LIBs. However, their limitation due to capacity fading and the large initial irreversile capacity loss must be resolved before commercialization. The observed limitations are attributed to many factors, and particularly, to the formation and growth of SEI layer which is the common factor for all the three electrode materials. Because of the strong capacity fade and lack of many detailed studies on the Sn-based materials, specifically SnSb, we focus our study to investigate the formation and growth of SEI layer on SnSb electrode.

The evolution of the electrical, compositional, and morphological properties have been investigated in detail to understand the electrochemical behavior of micron-sized SnSb. Electron microscopy (scanning electron microscopy and transmission electron microscopy), chemical analysis techniques (Fourier transform infrared spectroscopy and nuclear magnetic resonance spectroscopy) and electrochemical impedance spectroscopy have been combined to evidence the electrode modifications and particularly the formation of a thick SEI layer. The primary components of the SEI

formed are LEDC and LiF. Evolution of the SEI resistance and the charge transfer resistance with the cell voltage can be explained by the electrolyte degradation and expansion/contraction of the electrode. Moreover, we show that the SEI formation is not limited at the first discharge/charge of the battery. The continuous growth of the SEI layer up to 50 cycles associated to the electrode pulverization caused by the large volume variations are responsible for the capacity fading.

To limit the capacity fade, we propose the use of a protective film on the electrode surface. The electrochemical performance of micron-sized SnSb electrode coated with thermoplastic elastomer protective film, namely poly(styrene-*b*-2-hydroxyethyl acrylate) PS-*b*-PHEA has been achieved. The PS-*b*-PHEA, was synthesized using controlled/living free-radical polymerization based on polystyrene macroinitiator and 2-hydroxyethyl acrylate (HEA) monomer. The excellent cycle life performance and rate capability obtained for SnSb (PS-*b*-PHEA) electrode is attributed to the high failure strain characteristics of the PS-*b*-PHEA elastomer film. The elastomer film can accommodate the large volume expansion during lithium alloying/dealloying reaction with SnSb and control the SEI growth. As a result the SnSb electrode is mechanically stable for at least 50 cycles. The use of elastomer polymer coating can be extended to other high capacity electrode materials that suffer from large volume changes and SEI formation during cycling.

RÉSUMÉ

Les accumulateurs commerciaux à base de lithium-ion (LIB) utilisent des matériaux à base de carbone (graphite) comme électrode négative; cependant, la technologie atteint sa limite en raison de la faible capacité spécifique théorique (372 mAh g-1). L'objectif de cette thèse est d'étudier le comportement électrochimique de trois nouvelles anodes à haute capacité comme alternatives au graphite, d'identifier les principaux paramètres responsables de la perte de capacité et de proposer une solution commune pour améliorer leurs performances électrochimiques.

Tout d'abord, l'alliage microstruturé SnSb synthétisé par des techniques hyperfréquences a été étudié. Le SnSb présente une importante capacité (833 mAh g-1) qui est obtenue jusqu'au 20^{eme} cycle. Cependant, elle diminue très rapidement après 25 cycles suggérant que l'électrode est dégradée en raison des contraintes mécaniques causées par les grandes variations de volume lors des réactions de l'électrode avec le lithium. En outre, la formation de craquelures à la surface de l'électrode génère de nouvelles zones de surfaces qui favorisent la décomposition de l'électrolyte qui se traduit par une couche mince interfaciale appelée « solid electrolyte interphase » (SEI). La perte de contact électrique avec le matériau actif combinée à la formation de la SEI sont ainsi responsables des mauvaises performances électrochimiques lors du cyclage. Le second matériau d'électrode a été fabriqué par anodisation du Ti3SiC2 pour former des films poreux contenant de l'anatase, une faible quantité de carbone et de la silice. En faisant varier les paramètres d'anodisation (temps d'anodisation, potentiel appliqué et concentration en fluor dans l'électrolyte aqueux), diverses morphologies d'oxyde ont été réalisées. Après 140 cycles effectués à de multiples densités de courant, une capacité de 380 µAh cm-2 (pour un courant appliqué de 200 µA cm-2) a été obtenue pour Ti3SiC2 anodisé à 60 V. La performance électrochimique a été améliorée en jouant sur la morphologie des composés anodisés à différents potentiels. Deux structures poreuses typiques, nano-lamellaires et mésoporeuses, ont été respectivement obtenues à faible et haut potentiel appliqué. Par rapport à la morphologie mésoporeuse générée à 60 V, la densité de puissance délivrée par la structure en couche lamellaire formée à 10 V est presque triplée. La voltammétrie cyclique a été utilisée pour expliquer que cette

amélioration est liée à la plus grande quantité de lithium stockée à la surface de la structure. La perte de capacité observée après le premier cycle est attribuée à la réaction irréversible des ions lithium avec des molécules d'eau résiduelles, le piégeage des ions lithium dans les défauts structurels du dioxyde de titane ainsi que la formation de la SEI.

Les performances électrochimiques de nanotubes de silicium poreux ont également été étudiées. Ces nanotubes de silicium poreux ont été fabriqués sur des substrats en acier inoxydable par un prcédé « template » impliquant des nanofils d'oxyde de zinc sacrifiés. L'électrode poreuse de nanotubes de Si a montré des capacités de décharge élevées et une meilleure stabilité que certaines anodes nanostructurées de Si rapportées dans la literature. Une deuxième capacité de décharge de 3095 mAh g-1 (avec une efficacité coulombique de 63%) a été obtenue à C / 20 qui atteint une valeur stable de 1670 mAh g-1 après 30 cycles. Ceci est attribué à la grande surface générée par la porosité des nanostructures 3D favorisant ainsi le stockage du lithium-ion selon un mécanisme pseudocapacitif. La perte de la capacité durant les premiers cycles est également attribuée à la formation d'une SEI. En outre, les grandes variations de volume des nanotubes réagissant avec les ions lithium entraînent un détachement partiel des nanostructures.

Ces trois matériaux d'électrode présentent globalement une bonne performance électrochimique qui les rend prometteurs pour remplacer le carbone en tant qu'électrode négative pour les accumulateurs Li-ion. Cependant, leur limitation en raison de la perte de la capacité durant les premiers cycles doit être résolue avant leur commercialisation. Les limitations observées sont attribuées à de nombreux facteurs, et en particulier à la formation et à la croissance de la SEI. En raison de la forte perte de la capacité et du manque d’études détaillées sur les matériaux à base d’étain, en particulier le SnSb, nous avons concentré la suite du travail à la formation et la croissance de la cSEI sur cette électrode négative.

L'évolution des propriétés électriques, de la composition chimique et de la morphologie du SnSb microstructuré a été étudiée en détail pour comprendre son comportement électrochimique. La microscopie électronique (microscopie électronique à balayage et la

microscopie électronique à transmission), les techniques d'analyse chimique (spectroscopie infrarouge à transformée de Fourier et spectroscopie à résonance magnétique nucléaire) et la spectroscopie d'impédance électrochimique ont été combinées pour suivre les modifications du SnSb et en particulier la formation d'une SEI épaisse. Les principaux composés de la SEI formée sont du LEDC et du LiF. L'évolution de la sa résistance et la résistance au transfert de charge s'expliquent par la dégradation des électrolytes et l'expansion / contraction de l'électrode qui se produisent au cours du cyclage. De plus, nous montrons que la formation de la SEI n'est pas limitée à la première décharge / charge de la batterie. La croissance de la couche isolante se produit jusqu'à 50 cycles. Combinée à la dégradation des électrodes causée par les grandes variations de volume, ces deux facteurs sont clairement responsables de la perte de la capacité. Pour limiter cet effet, nous avons proposé d'appliquer un film protecteur à la surface de l'électrode. Nous avons évalué les performances électrochimiques du SnSb recouvert d'un film protecteur en élastomère thermoplastique, à savoir de l'acrylate de poly (styrène-b-2-hydroxyéthyle) PS-b-PHEA. Le PS-b-PHEA a été synthétisé en utilisant une polymérisation radicalaire contrôlée à base de macro initiateur de polystyrène et d'un monomère d'acrylate de 2-hydroxyéthyle (HEA). L'excellente performance de cycle et le maintien de la capacité sont attribués aux propriétés de grande déformation de l'élastomère. En effet, celui-ci peut supporter une grande expansion de volume lors des réactions du SnSb avec les ions lithium et inhiber la croissance de la SEI. En conséquence, l'électrode SnSb est mécaniquement stable pendant au moins 50 cycles. L'utilisation d'un revêtement polymère en élastomère peut être ainsi étendue à d'autres matériaux d'électrode qui souffrent d'importants changements de volume et qui sont sujets à la formation d'une SEI.

TABLE OF CONTENTS

LIST OF MAJOR ABBRIVATIONS

LIB	Lithium-ion battery
CV	Cyclic voltammetry
GCPL	Galvanostatic cycling with potential limitation
EIS	Electrochemical impedance spectroscopy
Cdl	Double layer capacitance
Re	Electrolyte resistance
Rct	Charge resistance
Rsei	Solid electrolyte interphase resistance
W	Warburg semi-infinite diffusion
CE	Coulombic efficiency
SEI	Solid electrolyte interphase
TEM	Transmission electron microscope
SEM	Scanning electron microscope
Ic	Pseudocapacitive current
Id	Bulk diffusion current
Ip	Peak discharge current
NMR	Proton nuclear magnetic resonance
FTIR	Fourier Transform Infrared Spectroscopy
SEC	Size Exclusion Chromatography
XRD	X-ray diffraction spectroscopy
XPS	X-ray Photoelectron Spectroscopy
A-Ti_3SiC_2	Anodized titanium silicon carbide
SnSb	Tin antimony alloy
SiNTs	Silicon nanotube arrays
PS-*b*-PHEA	Poly(styrene-*b*-2-hydroxyethyl acrylate)

MAMA-SG1	(*N-tert*-butyl-*N*-(1′-diethylphosphono-2,2′-dimethylpropyl)-*O*-(2-carboxyl-prop-2-yl) alkoxyamine initiator
M_n	Number-average molecular weight
Đ	Dispersity
CFRP	Controlled/living free radical polymerization

LIST OF FIGURES

LIST OF TABLES

CHAPTER 1

INTRODUCTION

1.1 Background

Rapid industrialization over the past few decades due to globalization, increased household energy consumption, and inventions in new technologies has resulted in the unprecedented increase in the demand for energy. The growing demand is mostly met by conventional fossil fuels (i.e. coal, oil and natural gas) which account for 86 % of the total worldwide energy consumption in 2016 [1]. However, the abundant use of fossil fuels has become a cause of concern due to their adverse effects on the environment, particularly related to the emission of carbon dioxide (CO_2), a major contributor of greenhouse gases (GHGs) [2]. In an effort to mitigate the increasing effects of GHGs on climate change, the Conference of Parties (COP) of the United Nations Framework Convention for Climate Change (UNFCCC) has agreed in 2015 to limit the increase of global temperature to 2 °C above pre-industrial levels by 2020 [3]. Furthermore, the non-renewability, susceptibility to price fluctuations and market manipulations, and the serious impact on aquatic life during oil spillage made fossil fuels unsustainable and unviable [4]. Renewable energy resources, such as wind, sun, water, sea, geothermal and biomass, have become better alternatives for conventional energy resources [5, 6].

The intermittency nature of renewable energy sources is a challenge in providing constant and on-demand power delivery. Thus, an energy storage device has become an important part of the renewable energy technology development [7, 8]. Several types of storage system are already in wide use to store and balance variable output from renewable sources: mechanical storage (compressed air energy storage, pumped-storage electricity, Flywheel), thermal storage (molten salt, solar pond), electrical storage (capacitor, supercapacitors), and electrochemical storage (flow battery, rechargeable batteries). In particular, rechargeable batteries have gained great interest recently due to their modularity, portability, and ability to quickly supply electricity on demand [8].

Today, lithium-ion batteries (LIBs) are among the most studied, and widely used, energy storage devices owing to their high energy densities, low self-discharge rates, wide range of operating temperatures, no memory effects, and long cycle lifes [9, 10]. Currently, LIBs are the dominant mobile power sources for portable electronic devices, mostly used in cell phones and laptop computers. Another important expanding market for LIBs is electric and hybrid vehicles [11].

To improve the characteristics of LIBs beyond the current state-of-the-art, it is necessary to develop new electrode and electrolyte materials that can provide better performance with a smaller environmental footprint as possible and improved safety [12]. Currently, LIBs use graphite materials as negative electrode which has a theoretical gravimetric capacity of 372 mAh g^{-1}. Among all negative electrode materials: metals (such as Sn, Sb, Si, Al, Ge) [13-17], metal oxides (such as $Li_4Ti_5O_{12}$, SnO_2, Mn_3O_4, TiO_2, Co_3O_4) [17-20] and alloys (such as SnSb, SbIn, Mg_2Si, SbAl) [21-25] have attracted some attention due to their relatively high potentials compared to Li/Li^+. They can react reversibly with Li^+ via intercalation, conversion, and/or alloying mechanisms.

Unfortunately, many of the metal and alloy negative electrodes suffer from high initial irreversible capacity loss and rapid capacity fade during cycling. The causes of large irreversible capacity for alloy anodes are considered to be the following:

- *Loss of active material and electrical contact*. Because of the large volume change during cycling, leads to cracking and pulverization of active particles and the surrounding matrix result in the disconnection of some alloy particles from the conductive carbon or current collector.
- *Formation of solid electrolyte interphase (SEI) films*. The formation of passive films due to the reduction of electrolyte on the surface of the anode electrode. In addition, the formation of the SEI films consumes irreversibly Li^+ and electrolyte leading to large irreversible capacity loss and low coulombic efficiency. The SEI characteristics such as degradability, film thickness, and Li^+ conductivity dictate the kinetics of the electrochemical reactions and hence the batteries performance.

- *Trapping in the host alloy*. Even though Li insertion/extraction in alloys is generally reversible, some Li^+ may be permanently trapped in the alloys due to (a) slow Li release kinetics, (b) the formation of highly stable lithiated compounds or (c) strong bonding with less coordinated atoms at defect sites.
- *Reaction with surface oxide layers*. Because many metals are reactive with oxygen or water, a passivation oxide layer is normally formed on a metal or alloy particle surface during material preparation. This leads to the irreversible reaction of the oxide impurities with Li^+.
- *Aggregation of alloy particles*. Electrochemical aggregation has been observed in many fine-grained alloy anodes during cycling due to the welding effect induced by the pressure resulting from the large volume expansion. The agglomeration of active particles results in the increase of Li^+ diffusion length and the trapping of SEI films in the particles, leading to irreversible capacity loss.

In an attempt to reduce the initial irreversible capacity loss and improve the electrochemical performance of the battery, various strategies have been proposed to reduce the large volume variation during cycling and to modify the SEI layer. These approaches are classified into the following three major categories.

- *Electrode Modification.*
  - *The use of composites, oxides, intermetallics and alloys.* The use of the host matrix is to buffer the large volume change of the active particles so that the electrode integrity and the electronic contact between the active particles and conductive phase can be maintained. Based on the type of host phase, composite anodes can be described as (i) inactive matrix (Si/TiN) [26], (ii) active matrix (Si/SnSb) [27], and (iii) carbon-matrix composite [28].
  - *Particle size*. It has been reported that voids between nano-objects (nanotubes, nanowires, nanoporous particles, etc.) of metal anodes are able to bear the volume expansion during cycling which is otherwise responsible for the strong capacity fading and the poor electrochemical cycling obtained in the case of bulk materials [29, 30].

- *Binder.* The battery performance is significantly influenced by binders which constitutes 5 – 15 wt. % of the fabricated electrode. The use of sodium carboxymethyl cellulose (CMC) binder instead of polyvinyl fluoride (PVDF) shows better performance for alloy materials [31, 32].

- *Electrolyte Modification.* The chemical modification of the electrolyte by adding additives like vinyl carbonate (VC) and fluroethylene carbonate (FEC) to form a conductive thin layer of SEI film. This thin film can protect the electrode from further electrolyte decomposition resulting in enhanced electrochemical performance [33].
- *Electrode/Electrolyte Interphase Modification.* The inefficient passivation of the anode electrode by the SEI film leads to further electrolyte reduction on the surface of the electrode. The modification of the electrode surface by coating with inorganic (such as Ni, Zn, Ag, Al) [34-36] and organic compounds (such as polythiophene, polypyrrole, self-healing polymer based on polystyrene polyacrylate amide) [37-39] is a good strategy to protect the electrode surface from thick and dynamic SEI film formation as well as to prevent the loss of active material and electrical contact due to the large volume change during cycling [34].

1.2 Objective

The objective of this thesis is to study the electrochemical behaviour of three different new high capacity anodes as alternative to graphite, identify the main parameters responsible for the capacity fading, and propose a versatile solution to improve their electrochemical performance.

- Tin Antimony alloy (SnSb)
- Anodized Titanium Silicon Carbide (A-Ti_3SiC_2)
- Silicon nanotube arrays (SiNTs)

The limitation, such as capacity fading and the large initial irreversible capacity loss, are attributed to many factors, and particularly, to the formation and growth of SEI layer which is the common factor for all the three electrode materials. Because of the strong capacity fade and lack of many detailed studies on the Sn-based materials, specifically SnSb, we focus our study to investigate the formation and growth of SEI layer on SnSb

electrode. To limit the capacity fade we investigate the use of a protective film on the electrode surface. To reach these goals, it is proposed:

- To study the SEI film formation mechanism on SnSb anodes by electrochemical impedance spectroscopy, electron microscopy (scanning electron microscopy and transmission electron microscopy), and chemical analysis techniques (Fourier transform infrared spectroscopy and nuclear magnetic resonance spectroscopy).
- To exploit the advantages of coating of the SnSb electrode surface using stretchable polymers.
- To achieve the synthesis and characterization of stretchable polymers.

1.3 References

[1] W.E. Council, World Energy Resources 2016

https://www.worldenergy.org/wp-content/uploads/2016/10/World-Energy-Resources-Full-report-2016.10.03.pdf.

[2] U.S.E.P. Agency, Global Greenhouse Gas Emissions Data (2017)

https://www.epa.gov/ghgemissions/global-greenhouse-gas-emissions-data.

[3] U.N.F.C.o.C. Change, Historic Paris Agreement on Climate Change 195 Nations Set Path to Keep Temperature Rise Well Below 2 Degrees Celsius

http://newsroom.unfccc.int/unfccc-newsroom/finale-cop21/.

[4] U.S.E.P. Agency, Inventory of U.S. Greenhouse Gas Emissions and Sinks 1990 - 2015, 2017.

[5] T.B. Johansson, L. Burnham, Renewable energy: sources for fuels and electricity, Island press 1993.

[6] N.L. Panwar, S.C. Kaushik, S. Kothari, Role of renewable energy sources in environmental protection: A review, Renew. Sustainable Energy Rev., 15 (2011) 1513-1524.

[7] M. Yekini Suberu, M. Wazir Mustafa, N. Bashir, Energy storage systems for renewable energy power sector integration and mitigation of intermittency, Renew. Sustainable Energy Rev., 35 (2014) 499-514.

[8] X. Luo, J. Wang, M. Dooner, J. Clarke, Overview of current development in electrical energy storage technologies and the application potential in power system operation, Appl. Energy, 137 (2015) 511-536.

[9] D. Linden, T. Reddy, Handbook of Batteries, 3rd ed., McGraw-Hill Inc., New York, 2001.

[10] B. Scrosati, J. Garche, Lithium batteries: Status, prospects and future, J. Power Sources, 195 (2010) 2419-2430.

[11] M. Lowe, S. Tokuoka, T. Trigg, G. Gereffi, Lithium-ion batteries for electric vehicles, Duke University Center on Globalization, Governance and Competitiveness, Tech. Rep., (2010).

[12] V. Etacheri, R. Marom, R. Elazari, G. Salitra, D. Aurbach, Challenges in the development of advanced Li-ion batteries: a review, Energy Environ. Sci., 4 (2011) 3243-3262.

[13] B. Liang, Y. Liu, Y. Xu, Silicon-based materials as high capacity anodes for next generation lithium ion batteries, J. Power Sources, 267 (2014) 469-490.

[14] M.-H. Park, M.G. Kim, J. Joo, K. Kim, J. Kim, S. Ahn, Y. Cui, J. Cho, Silicon Nanotube Battery Anodes, Nano Lett., 9 (2009) 3844-3847.

[15] P. Meduri, C. Pendyala, V. Kumar, G.U. Sumanasekera, M.K. Sunkara, Hybrid tin oxide nanowires as stable and high capacity anodes for Li-ion batteries, Nano Lett., 9 (2009) 612-616.

[16] D. Larcher, S. Beattie, M. Morcrette, K. Edstroem, J.-C. Jumas, J.-M. Tarascon, Recent findings and prospects in the field of pure metals as negative electrodes for Li-ion batteries, J. Mater. Chem., 17 (2007) 3759-3772.

[17] M. Winter, J.O. Besenhard, Electrochemical lithiation of tin and tin-based intermetallics and composites, Electrochim. Acta, 45 (1999) 31-50.

[18] P. Poizot, S. Laruelle, S. Grugeon, L. Dupont, J.M. Tarascon, Nano-sized transition-metal oxides as negative-electrode materials for lithium-ion batteries, Nature, 407 (2000) 496-499.

[19] H. Wang, L.-F. Cui, Y. Yang, H. Sanchez Casalongue, J.T. Robinson, Y. Liang, Y. Cui, H. Dai, Mn3O4− graphene hybrid as a high-capacity anode material for lithium ion batteries, J. Am. Chem. Soc., 132 (2010) 13978-13980.

[20] Y. Li, B. Tan, Y. Wu, Mesoporous Co3O4 nanowire arrays for lithium ion batteries with high capacity and rate capability, Nano Lett., 8 (2008) 265-270.

[21] J. Vaughey, C. Johnson, A. Kropf, R. Benedek, M. Thackeray, H. Tostmann, T. Sarakonsri, S. Hackney, L. Fransson, K. Edström, Structural and mechanistic features of intermetallic materials for lithium batteries, J. Power Sources, 97 (2001) 194-197.

[22] M. Wachtler, J.O. Besenhard, M. Winter, Tin and tin-based intermetallics as new anode materials for lithium-ion cells, J. Power Sources, 94 (2001) 189-193.

[23] H. Tostmann, A. Kropf, C. Johnson, J. Vaughey, M. Thackeray, In situ x-ray absorption studies of electrochemically induced phase changes in lithium-doped InSb, Phys. Rev. B, 66 (2002) 014106.

[24] M. Stjerndahl, H. Bryngelsson, T. Gustafsson, J.T. Vaughey, M.M. Thackeray, K. Edström, Surface chemistry of intermetallic AlSb-anodes for Li-ion batteries, Electrochim. Acta, 52 (2007) 4947-4955.

[25] M.T. Sougrati, J. Fullenwarth, A. Debenedetti, B. Fraisse, J.-C. Jumas, L. Monconduit, TiSnSb a new efficient negative electrode for Li-ion batteries: mechanism investigations by operando-XRD and Mössbauer techniques, J. Mater. Chem., 21 (2011) 10069-10076.

[26] I.s. Kim, P. Kumta, G. Blomgren, Si/TiN nanocomposites novel anode materials for Li-Ion batteries, Electrochem. Solid State Lett., 3 (2000) 493-496.

[27] H. Guo, H. Zhao, C. Yin, W. Qiu, Si/SnSb alloy composite as high capacity anode materials for Li-ion batteries, J. Alloys and Comp., 426 (2006) 277-280.

[28] X.-y. Zhou, J.-j. Tang, J. Yang, J. Xie, L.-l. Ma, Silicon@carbon hollow core–shell heterostructures novel anode materials for lithium ion batteries, Electrochim. Acta, 87 (2013) 663-668.

[29] T. Song, J. Xia, J.-H. Lee, D.H. Lee, M.-S. Kwon, J.-M. Choi, J. Wu, S.K. Doo, H. Chang, W.I. Park, Arrays of sealed silicon nanotubes as anodes for lithium ion batteries, Nano Lett., 10 (2010) 1710-1716.

[30] B.L. Ellis, P. Knauth, T. Djenizian, Three-Dimensional Self-Supported Metal Oxides for Advanced Energy Storage, Adv. Mater., 26 (2014) 3368-3397.

[31] J. Li, R. Lewis, J. Dahn, Sodium carboxymethyl cellulose a potential binder for Si negative electrodes for Li-ion batteries, Electrochem. Solid State Lett., 10 (2007) A17-A20.

[32] B. Lestriez, S. Bahri, I. Sandu, L. Roué, D. Guyomard, On the binding mechanism of CMC in Si negative electrodes for Li-ion batteries, Electrochem. Commun., 9 (2007) 2801-2806.

[33] H.A. Wilhelm, C. Marino, A. Darwiche, L. Monconduit, B. Lestriez, Significant electrochemical performance improvement of TiSnSb as anode material for Li-ion batteries with composite electrode formulation and the use of VC and FEC electrolyte additives, Electrochem. Commun., 24 (2012) 89-92.

[34] L.J. Fu, H. Liu, C. Li, Y.P. Wu, E. Rahm, R. Holze, H.Q. Wu, Surface modifications of electrode materials for lithium ion batteries, Solid State Sci., 8 (2006) 113-128.

[35] P. Yu, J.A. Ritter, R.E. White, B.N. Popov, Ni-Composite Microencapsulated Graphite as the Negative Electrode in Lithium-Ion Batteries I. Initial Irreversible Capacity Study, J. Electrochem. Soc., 147 (2000) 1280-1285.

[36] S.-S. Kim, Y. Kadoma, H. Ikuta, Y. Uchimoto, M. Wakihara, Electrochemical performance of natural graphite by surface modification using aluminum, Electrochem. Solid State Lett., 4 (2001) A109-A112.

[37] S. Kuwabata, N. Tsumura, S.i. Goda, C.R. Martin, H. Yoneyama, Charge-Discharge Properties of Composite of Synthetic Graphite and Poly (3-n-hexylthiophene) as an Anode Active Material in Rechargeable Lithium-Ion Batteries, J. Electrochem. Soc., 145 (1998) 1415-1420.

[38] M. Gaberšček, M. Bele, J. Drofenik, R. Dominko, S. Pejovnik, Improved carbon anode properties: pretreatment of particles in polyelectrolyte solution, J. Power Sources, 97 (2001) 67-69.

[39] C. Wang, H. Wu, Z. Chen, M.T. McDowell, Y. Cui, Z. Bao, Self-Healing Chemistry Enables the Stable Operation of Silicon Microparticle Anodes for High-Energy Lithium-ion Batteries, Nature Chem., 5 (2013) 1042-1048.

CHAPTER 2

LITHIUM-ION BATTERIES: A BRIEF REVIEW

2.1 Lithium-ion Batteries

Rapid development of new technologies, such as portable consumer electronics and electric vehicles, has generated the need for batteries that provide both high energy density and high power capability. Fig. 2.1 shows the energy density per unit volume (Wh l^{-1}) and per unit weight (Wh kg^{-1}) of various rechargeable batteries. Among the various existing technologies nickel metal hydride (Ni-MH) and lithium ion batteries (LIBs) are both excellent in terms of their volume energy density, the LIBs are superior in weight energy density, as it provides 1.5 times as much energy as the Ni-MH battery.

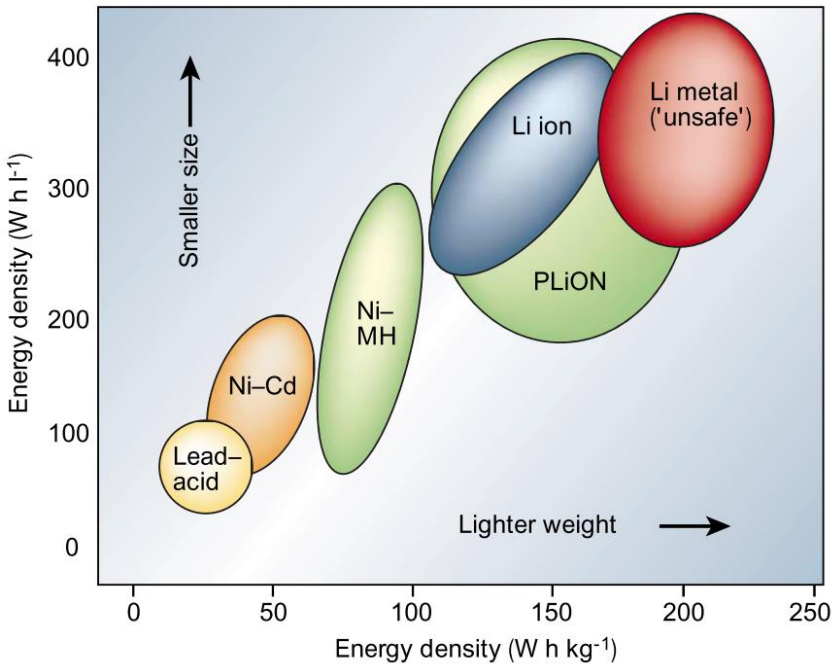

Fig. 2.1 Comparison of the different battery technologies in terms of volumetric (Wh l^{-1}) and gravimetric (Wh kg^{-1}) energy density [1].

Rechargeable lithium-ion batteries, which have been around since the 1990's [2], are an energy storage device that converts chemical energy to electrical energy through redox reactions involving lithium ions (Li^+) [3]. The motivation for using a battery technology based on lithium metal arise from the fact Li is the most electropositive (–3.04 V versus

standard hydrogen electrode) and lightest element, thus fulfilling the need to fabricate a high energy density battery. The early rechargeable lithium cells were plagued with safety problems caused by the tendency of lithium-metal anodes to form dendrites and Li electrodeposition leading to short circuit and explosion [4]. To circumvent the safety issues surrounding the use of Li metal, several alternative approaches were pursued in which either the negative electrode or the electrolyte was modified. Because of the presence of Li in its ionic rather than metallic state, Li-ion cells solve the dendrite problem and are, in principle, inherently safer than Li-metal cells [1, 4].

A lithium-ion rechargeable battery is also known as a swing battery or rocking chair battery since two-way movement of lithium-ions between positive and negative electrode through the electrolyte occurs during the charge and discharge processes. The positive electrode materials are usually layered oxides, spinel or olivine structures that react with Li^+ at high potential [5, 6]. The most common material used is $LiCoO_2$ (LCO), an oxide with Li^+ moving between the layers according to the following reaction [7]:

$$LiCoO_2 \rightleftharpoons Li_{1-x}CoO_2 + xLi^+ + xe^- \quad (2.1)$$

New higher capacity materials are continuously being developed with $LiNiMnCoO_2$, NMC, being one of the more popular recent developments with power capabilities that can be tailored for the application by slight variations in chemistry [8].

On the negative side, the most common electrode material up to now is graphite [5, 9]. The operating principle is very similar to that of the layered positive electrode with Li^+ going between sheets of carbon according to the following reactions:

$$C + xLi^+ + xe^- \rightleftharpoons Li_x C \quad (2.2)$$

Fig. 2.2 shows a schematic illustration of the processes taking place in a LIB during charge and discharge. During discharge, Li^+ are spontaneously released from the negative electrode (according to an oxidation reaction), pass across the electrolyte and intercalate into the positive electrode (according to a reduction reaction) while electrons flow from the negative to the positive electrode through the external circuit. During charge, the reversed processes take place.

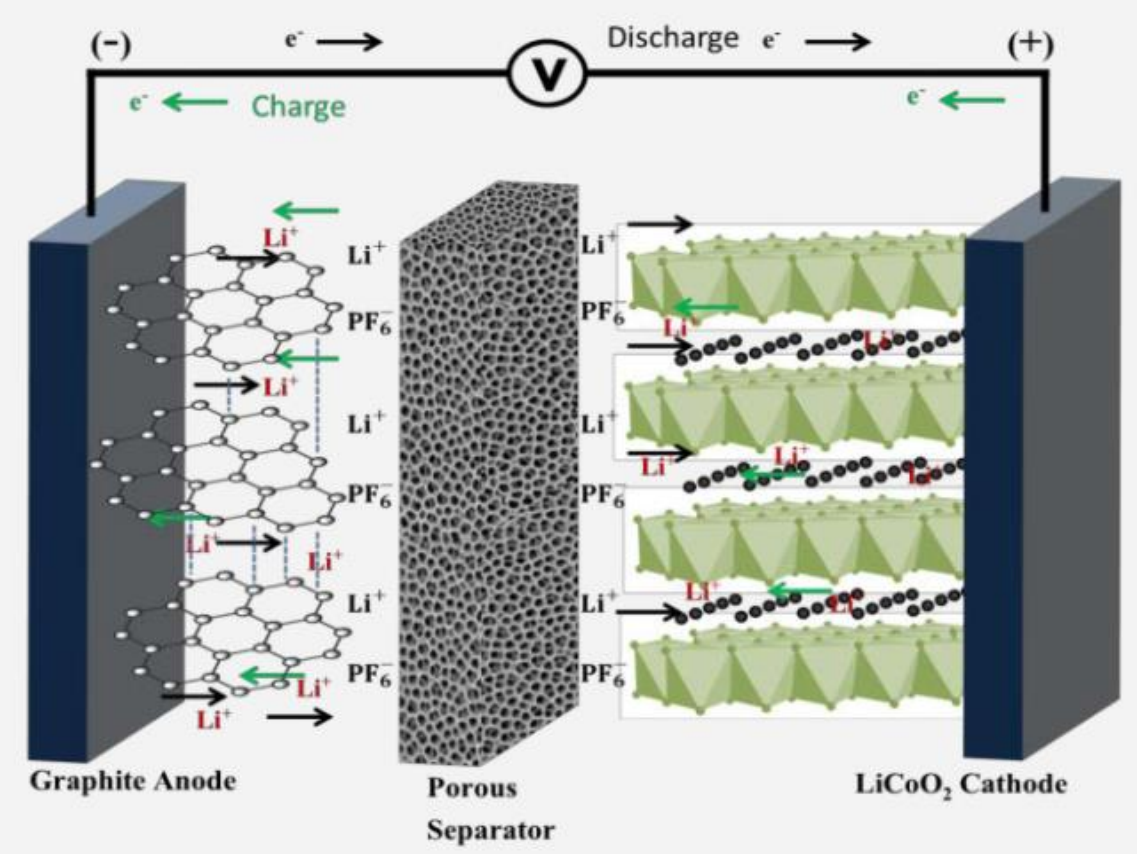

Fig. 2.2 A schematic illustration of a LIB during discharge ( ) and charge ( ).

Currently, commercial rechargeable LIBs widely use carbonaceous materials as negative electrodes, especially graphite carbon. However, the technology reaches a limit because of the low specific capacity offered by graphite (372 mAh g^{-1}) and lithium plating phenomenon at the surface in a fast charge [9, 10]. In order to enhance the energy density of LIBs, various anode materials have been proposed. For the sake of simplicity, anode materials are classified into three main groups depending on their reaction mechanisms.

- *Intercalation/de-intercalation materials* such as carbon based materials, porous carbon, carbon nanotubes, graphene, TiO_2, $Li_4Ti_5O_{12}$, etc… [9, 11-13].
- *Alloying/dealloying materials* such as Si, Ge, Sn, Sb, Al, Bi, SnSb, SnO_2, etc… [14-18].
- *Conversion materials* like transition metal oxides (Mn_xO_y, NiO, Fe_xO_y, CuO, Cu_2O, MoO_2, etc...), metal sulphides, metal phosphides and metal nitrides (M_xX_y; here X = S, P, N) [19-23].

Out of many alternative metal and alloy materials intensive studies have been focused on Si-based and Sn-based anode materials due to their extremely high lithium storage capacity ($Li_{22}Si_5$: 4200 mAh g^{-1}) and ($Li_{22}Sn_5$: 900 mAh g^{-1}), respectively [15, 24-27]. The main problem that hindered the commercialization of these materials is their relatively large volume expansion (~ 400 %) upon lithiation that results in pulverization and the loss of electrical contact at the early stage of cycling [15, 24, 28, 29]. Many efforts has been devoting to solve this problem by utilizing nanostructured materials (such as nanowires, nanotubes, nanopores) [27, 30-34] and by using binary phases like SnSb rather than a single phase material (Sn or Sb) [14, 15, 35, 36].

The Li^+ go back and forth between the anode and cathode through a porous membrane soaked in electrolyte. The liquid electrolyte consists of lithium salt stabilized by organic solution. The electrolyte components have two important selective criteria: (i) Li^+ conductivity for the entire battery life and (ii) they must be safe to be used for the entire potential window at which the battery operates. At higher potential, some of the components of the electrolyte components are oxidized at the cathode, which is a safety concern. On the anode, the low potential results in the reduction of the electrolyte to form the SEI composed of a mixture of organic and inorganic materials. The SEI characteristics such as degradability, film thickness, and Li^+ conductivity dictate the kinetics of the electrochemical reactions and hence, the battery performance.

2.2 Solid Electrolyte Interphase (SEI)

During the first cycle of the LIBs, the electrolyte undergoes reduction at the negatively polarized electrode surface. This cause significant electrolyte decomposition on the surface, which was first discovered in 1979 [37], and still is a major issue on the battery technology development. In an ideal case, this layer prevents further physical contact between the electrode surface and the solvent while concomitantly allowing Li^+ to pass through during cycling. This would protect the electrolyte from further degradation which results in limiting the large irreversible capacity loss due to the reaction of Li^+ with electrolyte decomposition products. However, in practice the SEI layers are dynamic and unstable.

The SEI is a very complex layer comprising of organic and inorganic components as the result of the salt degradation and the partial or complete reduction of the solvent of the electrolyte.

2.2.1 Mechanism of SEI Formation on Graphite Anode

Fig. 2.3 shows a schematic description of the SEI layer on graphite anode. Extensive investigations on graphite anodes using various spectroscopic techniques have identified that the main components of SEI are the decomposed products of electrolyte solvents and salts [40-42]. The current electrolytes use mixtures of alkyl carbonates including ethylene carbonate (EC) (a mandatory component for sufficient negative electrode passivation), dimethyl carbonate (DMC), diethyl carbonate (DEC), propylene carbonate (PC) and ethyl-methyl carbonate (EMC) as well as $LiPF_6$ salt [41, 43-46].

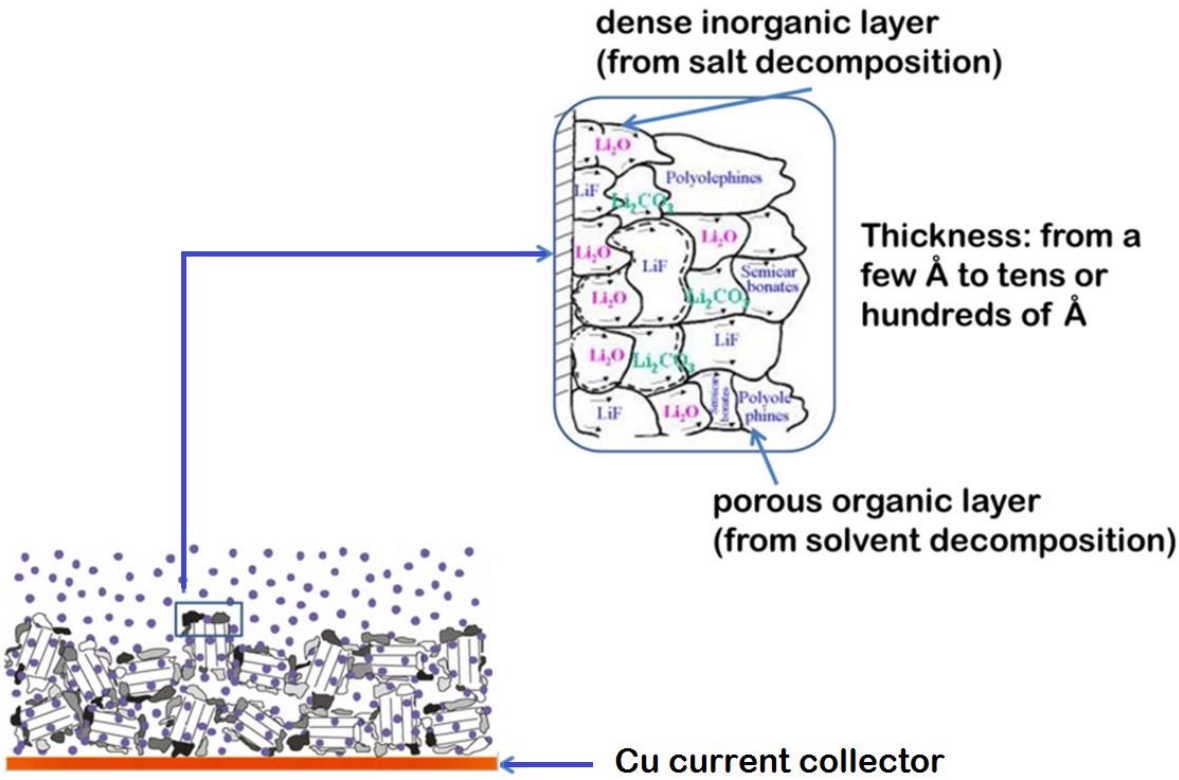

Fig. 2.3 Sketch of a lithiated graphite composite electrode covered by inhomogeneous SEI [38]. The inhomogeneous SEI layer is composed dense inorganic (dark grey) and porous organic (light grey) layer [39].

For carbonate-based solvents, two reduction reaction mechanisms have been proposed: (i) one-electron process as in the case of EMC shown in Eqs. (2.3 and 2.4) ; (ii) two-

electron process as in the case of DMC (Eq. 2.5); the combination of both processes occurs in the case of EC according to Eqs. (2.6 and 2.7) [43, 47-49].

$$CH_3CH_2O(C{=}O)OCH_3 + e^- \rightarrow CH_3CH_2O\left(C^{\bullet} - O^-\right)OCH_3 \quad (2.3)$$

$$CH_3CH_2O\left(C^{\bullet} - O^-\right)OCH_3 + e^- + 2Li^+ \rightarrow LiO(C{=}O)CH_3 + CH_3CH_2OLi \quad (2.4)$$

$$CH_3OCO_2CH_3 + 2e^- + 2Li^+ \rightarrow Li_2CO_3\downarrow + C_2H_{6(g)}\uparrow \quad (2.5)$$

$$(CH_2O)_2CO + 2e^- + 2Li^+ \rightarrow Li_2CO_3\downarrow + C_2H_{4(g)}\uparrow \quad (2.6)$$

$$EC + 2e^- + 2Li^+ \rightarrow (CH_2OCO_2Li)_2\downarrow + CH_2{=}CH_{2(g)}\uparrow \quad (2.7)$$

In EC containing electrolyte, the presence of H_20 traces will lead to the formation of Li_2CO_3, $(CH_2OH)_2$ and CO_2 gas according to Eq. (2.8). To avoid battery venting, it is necessary to maintain the H_20 content well below the minimal levels (< 1000 ppm) [41, 47].

$$(CH_2OCO_2Li)_2 + H_2O \rightarrow Li_2CO_3\downarrow + (CH_2OH)_2\downarrow + CO_{2(g)}\uparrow \quad (2.8)$$

Lithium hexafluorophosphate ($LiPF_6$) is the most commonly used electrolyte salt in LIBs. The degradation of $LiPF_6$ occurs in a two-step process in which the reduction is accompanied by the release of acid (Eq. 2.9) followed by decomposition of the salt according to Eqs. (2.10 – 2.15) [41, 48, 50, 51].

$$LiPF_6 \leftrightarrow LiF + PF_5 \quad (2.9)$$

$$PF_5 + H_2O \rightarrow 2HF + POF_3 \quad (2.10)$$

$$LiPF_6 + Li_2CO_3 \rightarrow 3LiF + POF_3 + CO_{2(g)}\uparrow \quad (2.11)$$

$$PF_5 + Li_2CO_3 \rightarrow 2LiF + POF_3 + CO_{2(g)}\uparrow \quad (2.12)$$

$$PF_5 + H_2O \rightarrow PF_4OH + HF \quad (2.13)$$

$$PF_4OH \rightarrow POF_3 + HF \quad (2.14)$$

$$Li_2CO_3 + 2HF \rightarrow 2LiF + CO_2 + H_2O \quad (2.15)$$

In the presence of EC in the electrolyte, POF_3 can react with EC decomposition products according to Eqs. (2.16 – 2.19) [41].

$$POF_3 + EC \rightarrow CH_2FCH_2OCOOPF_2O \quad (2.16)$$

$$CH_2FCH_2OCOOPF_2O \rightarrow CH_2FCH_2OPF_2O + CO_{2(g)}\uparrow \quad (2.17)$$

$$POF_3 + EC + PF_6^- \rightarrow CH_2FCH_2OCOOPF_3O^- + PF_5 \quad (2.18)$$

$$CH_2FCH_2OCOOPF_3O^- + PF_5 \rightarrow CH_2FCHOCOOPF_2O + PF_6^- \quad (2.19)$$

The SEI layer cracks on the surface of the electrode as the result of difference in thermal expansion between the various deposited products (organic and inorganic layer) and the graphite particles. This leads to further degradation of the electrolyte on the newly created surface.

2.3 Electrochemical Performance Parameters

Generally, the performance of LIBs is related to thecapacity of the cells. Capacity, measured in coulombs (C) or ampere-hours (Ah), refers to the overall amount of electrical charge that a battery can deliver. The theoretical capacity of each electrode material can be calculated according to the Faraday's laws which states that one gram-equivalent of the electrode material will deliver 96487 C or 26.8 Ah. The capacity term is given in Eq. (2.20).

$$Theoretical\ Capacity\ (Ah\ g^{-1}) = \frac{26.8\ (Ah\ mol^{-1}) * x}{M_w} \quad (2.20)$$

Where, x is the mol fraction of Li^+ reacting with the active material and M_w is the molecular mass of the active material in g mol^{-1}. For example, SnSb alloy has a molecular mass of 120.235 g mol^{-1}. The mole fraction of Li^+ alloyed with SnSb is corresping to the theoretical gravimetric capacity of 825 mAh g^{-1}.

Eventually, the energy density can be an interesting parameter to be considered. Its value is easily calculated multiplying the working voltage (V_{cell}) with capacity.

$$Energy\ Density\ (Wh\ g^{-1}) = V_{cell} * Capacity\ (Ah\ g^{-1}) \quad (2.21)$$

Another interesting parameter is the power density which can be calculated by dividing energy density by the operating time of the battery.

$$Power\ Density\ (W\ g^{-1}) = \frac{Energy\ Density\ (Wh\ g^{-1})}{Operating\ Time\ (h)} \quad (2.22)$$

2.4 References

[1] J.-M. Tarascon, M. Armand, Issues and challenges facing rechargeable lithium batteries, Nature, 414 (2001) 359-367.

[2] T. Nagaura, K. Tozawa, Progress in batteries and solar cells, JEC Press, 9 (1990) 209.

[3] D. Linden, T. Reddy, Handbook of Batteries, 3rd ed., McGraw-Hill Inc., New York, 2001.

[4] M. Yoshio, R.J. Brodd, A. Kozawa, Lithium-ion batteries, Springer2009.

[5] V. Etacheri, R. Marom, R. Elazari, G. Salitra, D. Aurbach, Challenges in the development of advanced Li-ion batteries: a review, Energy Environ. Sci., 4 (2011) 3243-3262.

[6] N. Nitta, F. Wu, J.T. Lee, G. Yushin, Li-ion battery materials: present and future, Mater. Today, 18 (2015) 252-264.

[7] E. Antolini, LiCoO 2: formation, structure, lithium and oxygen nonstoichiometry, electrochemical behaviour and transport properties, Solid State Ionics, 170 (2004) 159-171.

[8] S. Liu, L. Xiong, C. He, Long cycle life lithium ion battery with lithium nickel cobalt manganese oxide (NCM) cathode, J. Power Sources, 261 (2014) 285-291.

[9] Y.-P. Wu, E. Rahm, R. Holze, Carbon anode materials for lithium ion batteries, J. Power Sources, 114 (2003) 228-236.

[10] J.B. Goodenough, K.-S. Park, The Li-ion rechargeable battery: a perspective, J. Am. Chem. Soc., 135 (2013) 1167-1176.

[11] B.L. Ellis, P. Knauth, T. Djenizian, Three-Dimensional Self-Supported Metal Oxides for Advanced Energy Storage, Adv. Mater., 26 (2014) 3368-3397.

[12] V. Meunier, J. Kephart, C. Roland, J. Bernholc, Ab initio investigations of lithium diffusion in carbon nanotube systems, Phys. Rev. Lett., 88 (2002) 075506.

[13] J. Wang, H. Zhao, Q. Yang, C. Wang, P. Lv, Q. Xia, Li4Ti5O12–TiO2 composite anode material for lithium-ion batteries, J. Power Sources, 222 (2013) 196-201.

[14] H. Guo, H. Zhao, C. Yin, W. Qiu, Si/SnSb alloy composite as high capacity anode materials for Li-ion batteries, J. Alloys and Comp., 426 (2006) 277-280.

[15] M. Wachtler, J.O. Besenhard, M. Winter, Tin and tin-based intermetallics as new anode materials for lithium-ion cells, J. Power Sources, 94 (2001) 189-193.

[16] S. Needham, G. Wang, H. Liu, Electrochemical performance of SnSb and Sn/SnSb nanosize powders as anode materials in Li-ion cells, J. Alloy. Compd., 400 (2005) 234-238.

[17] P. Meduri, C. Pendyala, V. Kumar, G.U. Sumanasekera, M.K. Sunkara, Hybrid tin oxide nanowires as stable and high capacity anodes for Li-ion batteries, Nano Lett., 9 (2009) 612-616.

[18] D. Larcher, S. Beattie, M. Morcrette, K. Edstroem, J.-C. Jumas, J.-M. Tarascon, Recent findings and prospects in the field of pure metals as negative electrodes for Li-ion batteries, J. Mater. Chem., 17 (2007) 3759-3772.

[19] J. Jiang, Y. Li, J. Liu, X. Huang, C. Yuan, X.W.D. Lou, Recent advances in metal oxide-based electrode architecture design for electrochemical energy storage, Adv. Mater., 24 (2012) 5166-5180.

[20] Y. Jiang, D. Zhang, Y. Li, T. Yuan, N. Bahlawane, C. Liang, W. Sun, Y. Lu, M. Yan, Amorphous Fe 2 O 3 as a high-capacity, high-rate and long-life anode material for lithium ion batteries, Nano Energy, 4 (2014) 23-30.

[21] S. Boyanov, K. Annou, C. Villevieille, M. Pelosi, D. Zitoun, L. Monconduit, Nanostructured transition metal phosphide as negative electrode for lithium-ion batteries, Ionics, 14 (2008) 183-190.

[22] Z. Wang, L. Zhou, Metal Oxide Hollow Nanostructures for Lithium-ion Batteries, Adv. Mater., 24 (2012) 1903-1911.

[23] J. Cabana, L. Monconduit, D. Larcher, M.R. Palacin, Beyond Intercalation-Based Li-Ion Batteries: The State of the Art and Challenges of Electrode Materials Reacting Through Conversion Reactions, Adv. Mater., 22 (2010).

[24] H. Mukaibo, T. Osaka, P. Reale, S. Panero, B. Scrosati, M. Wachtler, Optimized Sn/SnSb lithium storage materials, J. Power Sources, 132 (2004) 225-228.

[25] C.K. Chan, H. Peng, G. Liu, K. McIlwrath, X.F. Zhang, R.A. Huggins, Y. Cui, High-performance lithium battery anodes using silicon nanowires, Nat. Nanotechnol 3(2008) 31-35.

[26] B. Liang, Y. Liu, Y. Xu, Silicon-based materials as high capacity anodes for next generation lithium ion batteries, J. Power Sources, 267 (2014) 469-490.

[27] A.T. Tesfaye, R. Gonzalez, J.L. Coffer, T. Djenizian, Porous silicon nanotube arrays as anode material for Li-ion batteries, ACS Appl. Mater. Interfaces, 7 (2015) 20495-20498.

[28] U. Kasavajjula, C. Wang, A.J. Appleby, Nano-and bulk-silicon-based insertion anodes for lithium-ion secondary cells, J. Power Sources, 163 (2007) 1003-1039.

[29] L. Beaulieu, T. Hatchard, A. Bonakdarpour, M. Fleischauer, J. Dahn, Reaction of Li with alloy thin films studied by in situ AFM, J. Electrochem. Soc., 150 (2003) A1457-A1464.

[30] D. Wang, Z. Yang, F. Li, X. Wang, D. Liu, P. Wang, D. He, Performance of Si–Ni nanorod as anode for Li-ion batteries, Mater. Lett., 65 (2011) 3227-3229.

[31] X.-y. Zhou, J.-j. Tang, J. Yang, J. Xie, L.-l. Ma, Silicon@carbon hollow core–shell heterostructures novel anode materials for lithium ion batteries, Electrochim. Acta, 87 (2013) 663-668.

[32] M.-H. Park, M.G. Kim, J. Joo, K. Kim, J. Kim, S. Ahn, Y. Cui, J. Cho, Silicon Nanotube Battery Anodes, Nano Lett., 9 (2009) 3844-3847.

[33] J. Jiang, Y. Li, J. Liu, X. Huang, Building one-dimensional oxide nanostructure arrays on conductive metal substrates for lithium-ion battery anodes, Nanoscale, 3 (2011) 45-58.

[34] T. Song, J. Xia, J.-H. Lee, D.H. Lee, M.-S. Kwon, J.-M. Choi, J. Wu, S.K. Doo, H. Chang, W.I. Park, Arrays of sealed silicon nanotubes as anodes for lithium ion batteries, Nano Lett., 10 (2010) 1710-1716.

[35] M.T. Sougrati, J. Fullenwarth, A. Debenedetti, B. Fraisse, J.-C. Jumas, L. Monconduit, TiSnSb a new efficient negative electrode for Li-ion batteries: mechanism investigations by operando-XRD and Mössbauer techniques, J. Mater. Chem., 21 (2011) 10069-10076.

[36] M. Winter, J.O. Besenhard, Electrochemical lithiation of tin and tin-based intermetallics and composites, Electrochim. Acta, 45 (1999) 31-50.

[37] E. Peled, The electrochemical behavior of alkali and alkaline earth metals in nonaqueous battery systems—the solid electrolyte interphase model, J. Electrochem. Soc., 126 (1979) 2047-2051.

[38] P. Verma, P. Maire, P. Novák, A review of the features and analyses of the solid electrolyte interphase in Li-ion batteries, Electrochim. Acta, 55 (2010) 6332-6341.

[39] G. Ramos-Sanchez, F. Soto, J.M. de la Hoz, Z. Liu, P. Mukherjee, F. El-Mellouhi, J. Seminario, P. Balbuena, Computational studies of interfacial reactions at anode materials: initial stages of the solid-electrolyte-interphase layer formation, Journal of Electrochemical Energy Conversion and Storage, 13 (2016) 031002.

[40] L. Huang, Z. Min, Q. Zhang, Solid electrolyte inter-phase on graphite anodes in Li-ion batteries, Rev. Adv. Mater. Sci, 36 (2014) 13-20.

[41] V.A. Agubra, J.W. Fergus, The formation and stability of the solid electrolyte interface on the graphite anode, J. Power Sources, 268 (2014) 153-162.

[42] S. Zhang, M.S. Ding, K. Xu, J. Allen, T.R. Jow, Understanding solid electrolyte interface film formation on graphite electrodes, Electrochem. Solid State Lett., 4 (2001) A206-A208.

[43] C. Huang, S. Zhuang, F. Tu, Electrode/Electrolyte Interfacial behaviors of LiCoO2/mixed graphite Li-Ion cells during operation and storage, J. Electrochem. Soc., 160 (2013) A376-A382.

[44] S.S. Zhang, A review on electrolyte additives for lithium-ion batteries, J. Power Sources, 162 (2006) 1379-1394.

[45] A. Du Pasquier, F. Disma, T. Bowmer, A. Gozdz, G. Amatucci, J.M. Tarascon, Differential Scanning Calorimetry Study of the Reactivity of Carbon Anodes in Plastic Li-Ion Batteries, J. Electrochem. Soc. , 145 (1998) 472-477.

[46] H. Bryngelsson, M. Stjerndahl, T. Gustafsson, K. Edström, How dynamic is the SEI?, J. Power Sources, 174 (2007) 970-975.

[47] R. Dedryvère, H. Martinez, S. Leroy, D. Lemordant, F. Bonhomme, P. Biensan, D. Gonbeau, Surface film formation on electrodes in a LiCoO 2/graphite cell: A step by step XPS study, J. Power Sources, 174 (2007) 462-468.

[48] Y. Okamoto, Ab initio calculations of thermal decomposition mechanism of LiPF6-based electrolytes for lithium-ion batteries, J. Electrochem. Soc., 160 (2013) A404-A409.

[49] P. Novák, F. Joho, M. Lanz, B. Rykart, J.-C. Panitz, D. Alliata, R. Kötz, O. Haas, The complex electrochemistry of graphite electrodes in lithium-ion batteries, J. Power Sources, 97 (2001) 39-46.

[50] H. Wang, Y.I. Jang, B. Huang, D.R. Sadoway, Y.M. Chiang, TEM study of electrochemical cycling-induced damage and disorder in LiCoO2 cathodes for rechargeable lithium batteries, J. Electrochem. Soc., 146 (1999) 473-480.

[51] Z. Lu, L. Yang, Y. Guo, Thermal behavior and decomposition kinetics of six electrolyte salts by thermal analysis, J. Power Sources, 156 (2006) 555-559.

CHAPTER 3

CHARACTERIZATION TECHNIQUES

3.1 Characterization of Electrode Materials

3.1.1 X-ray diffraction (XRD)

The structure and purity of the negative electrodes were investigated by X-ray diffraction (XRD) analysis using a Siemens D5000 diffractometer (Germany) equipped with a copper anticathode (Cu Kα of λ = 1.5406 Å). The diffractograms were recorded with a 0.02° step size and a 4 s dwelling time. The diffractograms were analyzed using JCPDS-ICDD (Joint Committee on Powder Diffraction Standards−International Center for Diffraction Data) database.

3.1.2 Scanning Electron Microscopy (SEM)

The morphology of the negative electrode materials were investigated using a field-emission scanning electron microscope (FE-SEM, Philips XL-30 FEG SEM, The Netherlands) and (Ultra-55 Carl Zeiss) using an electron beam energy of 15 kV.

3.1.3 Transmission Electron Microscopy (TEM)

The morphology of the negative electrode materials were investigated using by JEOL 3010 at 300 kV. TEM images were acquired by dispersing the negative electrode materials in ethanol and sonicating for 5 minute before putting on TEM grids.

3.1.4 Energy Dispersive X-ray Spectrometry (EDS)

The chemical composition of the negative electrode materials were assessed using an energy-dispersive X-ray spectrometer (EDS; Oxford, U.K.).

3.1.5 X-ray Photoelectron Spectroscopy (XPS)

The chemical composition of the negative electrode materials were assessed using X-ray photoelectron spectroscopy (XPS; VersaProbe 5000, Physical Electronics Inc., U.S.A.). XPS spectra were taken at pass energy of 23.50 eV, with a step size of 0.2 eV for survey

and 0.025 eV for high-resolution spectra, employing a 100 µm monochromatic Al Kα X-ray beam to irradiate the sample surface. XPS peak fitting was carried out using Casa XPS version 2.3.16 RP 1.6.

3.1.6 Raman Spectroscopy

The vibrational, rotational, and other low-frequency modes in a system are used to provide a structural fingerprint of the negative electrode materials. Raman spectroscopy was carried out at room temperature (RT) on a Renishaw inVia (Gloucestershire, U.K.) microspectrometer using a He−Ne laser (632.8 nm), a 63× magnification, and 0.7 numerical aperture objective. The laser spot size was ∼ 1 µm in the focal plane. A grating with 1200 lines/mm was used to direct the reflected beam from the sample to the charge-coupling device (CCD). Thus, the system possessed a spectral resolution of ∼ 4 cm^{-1}.

3.1.7 Mercury Intrusion Porosimetry (MIP)

The porosity and pore size of the negative electrodes were investigated by the Pore Master 60 mercury injector (QuantaChrome Instruments). The samples were weighted and placed in dilatometer. After air-leakage tests and evacuation, mercury was first intruded into the dilatometer under a pressure of up to 20 psi to allow the mercury to fill the interspace between the larger particles. Then, the dilatometer was transferred to a high-pressure station to intrude mercury into the samples up to a maximum pressure of 35000 psi. The experimental pressure utilized was converted to a pore-throat diameter using the Washburn equation.

3.2 Polymer Characterization

3.2.1 Fourier Transform Infrared Spectroscopy (ATR-FTIR)

The chemical composition of the SEI film and the synthesized polymer was investigated using ATR-FTIR. Infrared analysis was carried out on a Perkin Elmer Spectrum 2 equipped with a single reflection diamond module (ATR). IR spectrum was recorded in the 400 – 4000 cm^{-1} range, at 4 cm^{-1} resolution.

3.2.2 Nuclear Magnetic Resonance (NMR)

Synthesized Polymers were characterized by ^{1}H NMR. Moreover, ^{1}H and ^{19}F NMR was used to investigate the chemistry of the SEI films. NMR experiments were performed with a Bruker Avance III 400 MHz Nanobay spectrometer. ^{1}H NMR spectra were recorded at frequency of 400 MHz with a 11.3 µs 30° pulse, a repetition time of 4 s and 16 scans. ^{19}F NMR spectra were recorded at frequency of 376 MHz at a repetition time of 0.7 s and 32 scans. All the NMR spectra were obtained at RT. NMR chemical shifts were reported in standard format as values in ppm relative to deuterated solvents. For NMR characterization, the sample was immersed during approximately 1 h in $CDCl_3$, unless stated otherwise. Then the solution was recovered and concentrated to reach the minimum volume for analysis (≈ 0.5 mL).

3.2.3 Size Exclusion Chromatography (SEC)

Polymer molecular weights and dispersities were determined by size exclusion chromatography. The SEC experiments were performed on EcoSEC apparatus an from PSS, equipped with a dual flow cell refractive index detector. The following columns were used: one pre-column and two PL Resipore columns. The injection loop, the columns and the RI detector were in the same oven thermostated at 70 °C. The eluent was a solution of 0.1 M LiBr in dimethylformamide and the flow rate was fixed at 0.7 mL min^{-1}. The samples were prepared in a mixture of eluent and toluene (0.25 vol. %) as flowmarker, filtered through a 0.2 µm Nylon filter (Interchim) and placed in an auto-sampler preheated at 50 °C. Samples concentration was 0.25 wt. %. Calibration curves were established with either polystyrene (PS) standards or poly(methyl methacrylate) (PMMA) standards, both purchased from PSS polymers.

3.3 Electrochemical Characterization

3.3.1 Cell Assembly

The two-electrode Swagelok test cells (Fig. 3.1) were assembled in Argon filled glovebox. Most of the electrochemical performance tests were done in the half-cell system, were the negative electrode are assembled against metallic Li foil using the liquid electrolyte

($LiPF_6$ in EC:DEC), unless stated otherwise. The Li foil was cut in a circular shape with the diameter of 9 mm. Two circular sheets (10 mm in diameter) of the Whatman glass microfiber papers were soaked with a commercial 1 M $LiPF_6$ in EC:DEC electrolyte and placed between the anode electrode and Li foil.

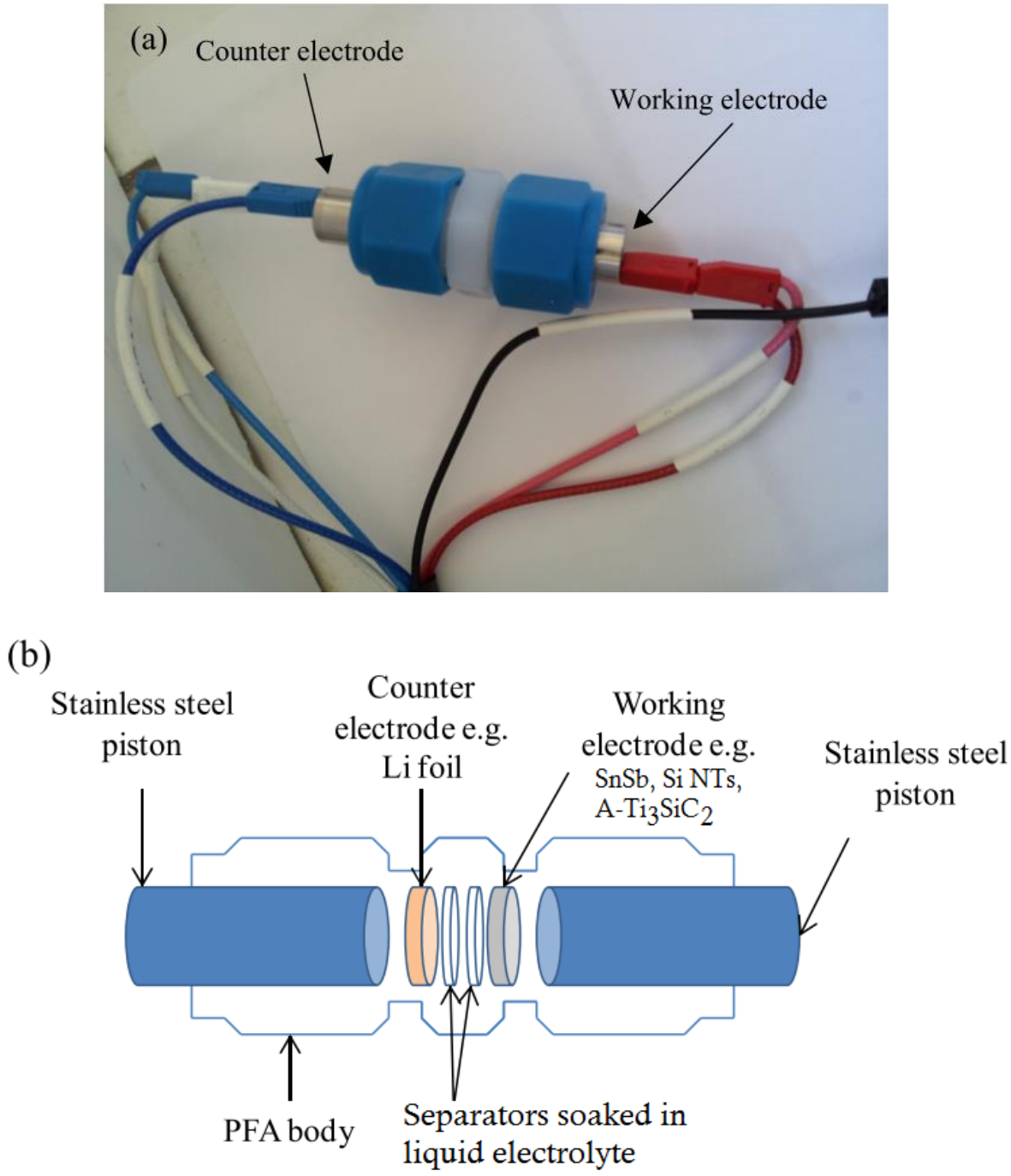

Fig. 3.1 (a) A two-electrode Swagelok test cell and (b) the schematic representation of the inner components.

The three-electrode Swagelok test cells (Fig. 3.2) for the EIS measurement were assembled using the negative electrode as working electrode, Li foil as counter electrode and another Li foil as a reference. Two circular sheets (10 mm in diameter) of the Whatman glass microfiber papers were soaked with a commercial 1 M $LiPF_6$ in EC:DEC electrolyte was used as a separator.

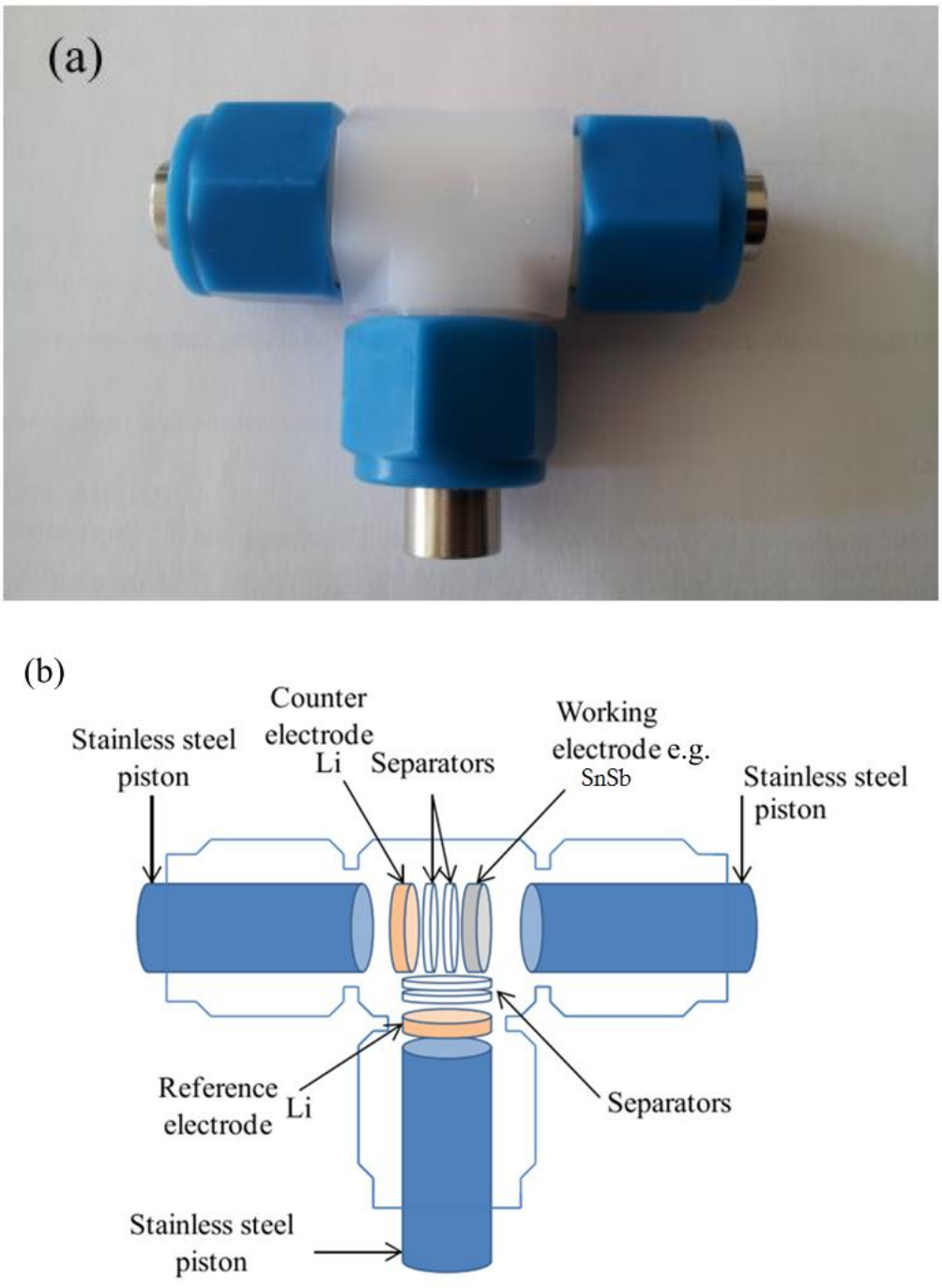

Fig. 3.2 (a) A three-electrode Swagelok test cell and (b) the schematic representation of the inner components.

3.3.2 Electrochemical Techniques

3.3.2.1 Chronoamperometric (CA)

CA was used to record the response current as function of time by applying potential at the working electrode. The CA curves were recorded using PARSTAT 2273.

3.3.2.2 Cyclic Voltammetry (CV)

The CV was used to observe the oxidation/reduction peaks of the system. The CV curves were recorded using VersaSTAT (AMETEK) or VMP3 (Bio-Logic).

3.3.2.3 Galvanostatic Measurement

The charge/discharge capacity, also the shapes of the charge/discharge profiles of the cells were investigated by the galvanostatic technique. The experiments were performed using VersaSTAT or VMP3 cycler.

3.3.2.4 Electrochemical Impedance Spectroscopy (EIS)

The EIS measurement was performed to observe the resistance of the cell. The impedance spectra were recorded at the end of the discharge state in the frequency range of 200 kHz to 10 mHz at 7 mV of amplitude using VMP3. The obtained spectra were fitted by "Z-fit" in the EC-Lab software (Bio Logic).

Electrochemical impedance spectroscopy (EIS) is a powerful technique for characterizing a wide variety of electrochemical systems, such as battery, and for determining the contribution of electrode or electrolytic processes in these systems. Electrochemical impedance is normally measured using a small excitation signal (E), so that the response signal (I) is pseudo-linear. In a linear (or pseudo-linear) system, the current response to a sinusoidal potential will be a sinusoid at the same frequency but shifted in phase. To achieve linearity in EIS analysis the excitation potential signal has to be in the range of 1 – 10 mV. The cell impedance (Z) is given according to Eq. (2.23)

$$Z = \frac{E}{I} = \frac{E_0 \sin(\omega t)}{I_0 \sin(\omega t + \emptyset)} = Z_0 \frac{\sin(\omega t)}{\sin(\omega t + \emptyset)} \qquad (2.23)$$

Where, E_0 amplitude of the signal, I_0 is the response signal, ω is the radial frequency, f is the frequency, and ∅ is the shifted phase.

Equivalent electrical circuit models are used to interpret the acquired impedance spectra.

I. *Electrolyte resistance (Re, Ω)* represents the resistance of the electrolyte solution and the electrode surface. Re depends on ionic concentration, type of ions, temperature and the geometry of the area in which the current pass.

II. *Double Layer Capacitance (Cdl, μF)* represents the capacitance of an electrical double layer exists on the interface between the electrode and its surrounding electrolyte. Cdl depends on electrode potential, ionic concentrations, temperature, electrode roughness, and impurity adsorption.

III. *Charge Transfer Resistance (Rct)* represents the charge transfer resistance at the electrode surface. Rct depends on number of electron transferred and exchange current density.

IV. *Solid Electrolyte Interphase Resistance (Rsei)* represents the resistance attributed to the SEI layer.

V. *Solid Electrolyte Interface Capacitance (Csei)* represents a capacitance arise at the interface between the SEI layer and the surrounding electrolyte.

VI. *Warburg Diffusion (W)* represents the semi-infinite diffusion of Li^+ into the electrode.

Impedance spectra can be represented by Nyquist plots which are composed of a real and imaginary parts. Fig. 3.3 shows a Nyquist plot for a given impedance spectrum and its equivalent electrical circuit. It can be noted that the Y-axis is negative and that each point on the Nyquist plot is the impedance recorded at one frequency. Re is represented by the intersection of the impedance spectra at high frequency with the X-axis. The Warburg impedance appears as a line with a slope of 45°.

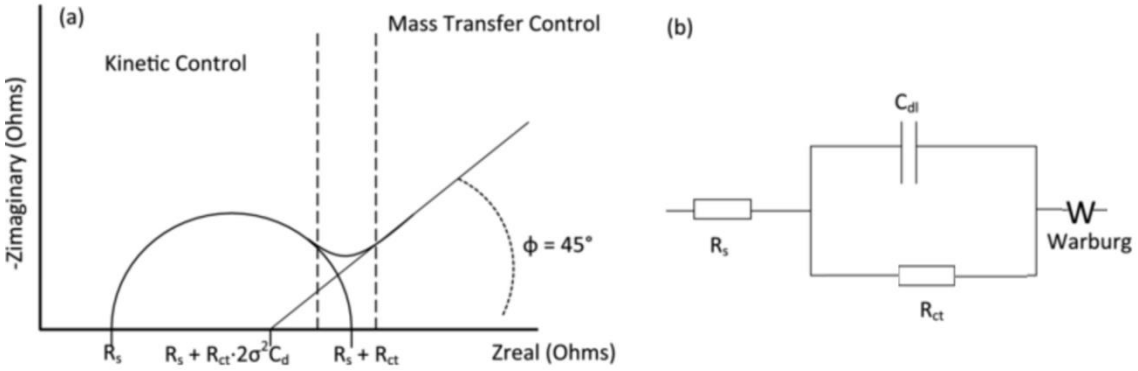

Fig. 3.3 (a) Typical Nyquist plot and (b) equivalent circuit used to interpret the impedance spectra.

CHAPTER 4

HIGH CAPACITY ANODE MATERIALS FOR LI-ION BATTERIES

The objective of this chapter is to investigate the synthesis and electrochemical behaviour of three different high capacity electrode materials to replace graphite as a negative electrode for LIBs. To achieve our goal, the chapter is divided into four sections.

- ***Section 4.1***. Investigations on micron-sized SnSb alloy as an anode electrode.
- ***Section 4.2***. An anode material for LIBs has been fabricated by anodizing Ti_3SiC_2 (MAX phase). Various anode structures were obtained by varying the fabrication parameters. A detail electrochemical study has been performed to explain the enhanced electrochemical performance by tailoring the morphology of the anode material (anodized Ti_3SiC_2).
- ***Section 4.3***. Silicon nanotubes were studied as anode material for LIBs. The advantage of nano-structuring is discussed to explain the improved electrochemical performance.
- ***Section 4.4***. Conclusion.

4.1 Tin-Antimony Alloy (SnSb)

4.1.1 Introduction

Li-ion batteries (LIBs) are currently the most important energy storage devices for a wide variety of applications such as cell phones, laptops and other portable electronic devices [1, 2]. However, the demand for high energy, power capability, longer cycle life, and a fast discharge–charge rate drives the research for new electrode and electrolyte materials [3, 4]. Antimony and tin have long been considered as an attractive replacement for graphite anodes (372 mAh g^{-1}) in LIB systems due to their superior lithium storage capacities of 660 and 994 mAh g^{-1}, respectively. Unfortunately, the reaction of these materials with Li^+ is accompanied by large volume expansion, which results in electrode disintegration and dynamic formation of solid electrolyte interphase (SEI) that reduce the battery life [5-7]. The key challenge is to improve the cycle life without sacrificing the high capacity afforded by the use of these elements.

A promising approach to this problem is to produce alloys and composite electrodes in which all components will react with lithium ions but at different stages in the charge and discharge cycles. For example for SnSb, in the electrochemical process, one component of the electrode alloys with lithium with the concomitant displacement of the second component from the intermetallic alloy; then, also this second component alloys with lithium. This two-step process is highly beneficial since it leads to a composite of two finely inter-dispersed lithiated phases and in course, the non-reacting component can “buffer” the volume changes of the reacting one during its alloying with lithium, this finally leading to a good operational stability [8-10].

The other strategy is to reduce the particle size of the host material to a nano-scale. Nano-structuring is beneficial to tolerate the mechanical stress caused due to the large volume change, more uniform stress distribution, and thus improve the cycling stability of the electrode [11, 12]. Unfortunately, the nano-scaled particles, due to their huge surface area, easily result in a considerable amount of surface oxide, which will lead to a significant irreversible capacity owing to the oxide reduction [13, 14]. The SnSb multiphase anode has demonstrated initial capacities exceeding 800 mAh g^{-1}. In this

section, the mechanism and the electrochemical performance of micron-sized SnSb alloy material has been studied as a negative electrode for high performance LIBs.

4.1.2 Experimental Sections

SnSb powder was synthesized using elemental Sn (99 % purity) and Sb (99.5 % purity) powders by microwave solid-state synthesis [15]. After microwave (MW) irradiation and natural cooling to room temperature, a spherical ingot of SnSb was obtained. Electrodes were prepared by using the micrometric SnSb powder obtained by grinding the as-prepared ingot in a mortar.

SnSb anode electrodes were fabricated using slurry cast method by mixing a SnSb powder, binding agent (polyvinylidene fluoride, PVDF), and conducting agent (Carbon black Sp) with mass ratio of 70:15:15 in vibrational ball milling for 25 min at 20 Hz. The slurry was tape casted on Cu current collector at room temperature for 12 h and then further dried at 110 ^{0}C for 12 h under vacuum.

Cyclic voltammetry (CV) and galvanostatic cycling with potential limitation (GCPL) were performed using standard two-electrode Swagelok cells assembled in a glove box filled with high purity argon. The half-cells were consisted of SnSb as the working electrode and Li foil served as the counter electrode. The two electrodes were separated by a Whatman glass microfiber soaked in the liquid organic electrolyte (1 M $LiPF_6$ in EC:PC:3DEC with 1% vol. VC and 5% vol. FEC). The cyclic voltammograms was performed in potential window of 0.01 − 1.75 V vs Li/Li^+ at a scan rate of 0.1 mV s^{-1}. The galvanostatic tests of the assembled cells were done at C/20, where C/n means the battery is fully charged or discharged up to its total storage capacity in n hours (for this work 1 C = 0.825 A g^{-1}).

4.1.3 Results and Discussion

The XRD patterns for pure SnSb powders are shown in Fig. 4.1.1a. The diffraction patterns of SnSb and of the β-Sn impurity were indexed to the $R\bar{3}m$ and $I4_1/amd$ space groups, respectively. The cell parameters of SnSb, refined by profile matching with a = b = 8.6563(4) Å, c = 10.7190(6) Å are in good agreement with the literature (ICSD 52294).

There was no measurable evidence of oxide contamination such as SnO, although it is expected that micron-sized metal or alloy particles will contain an oxide layer [16, 17]. Further TEM imaging is used to investigate the structure of SnSb powders. The selected

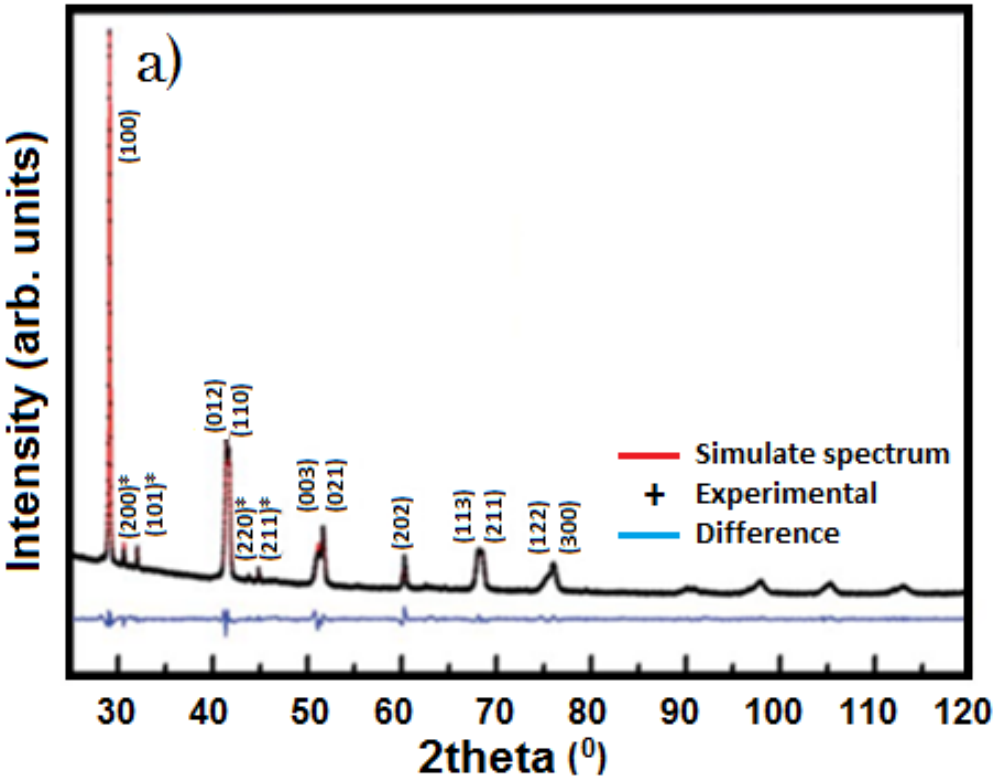

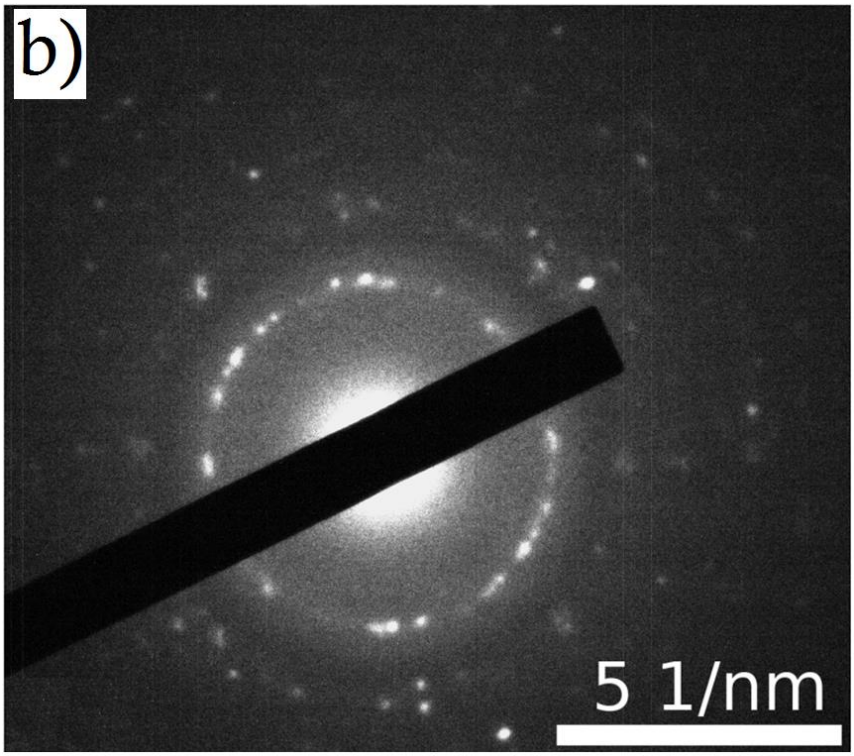

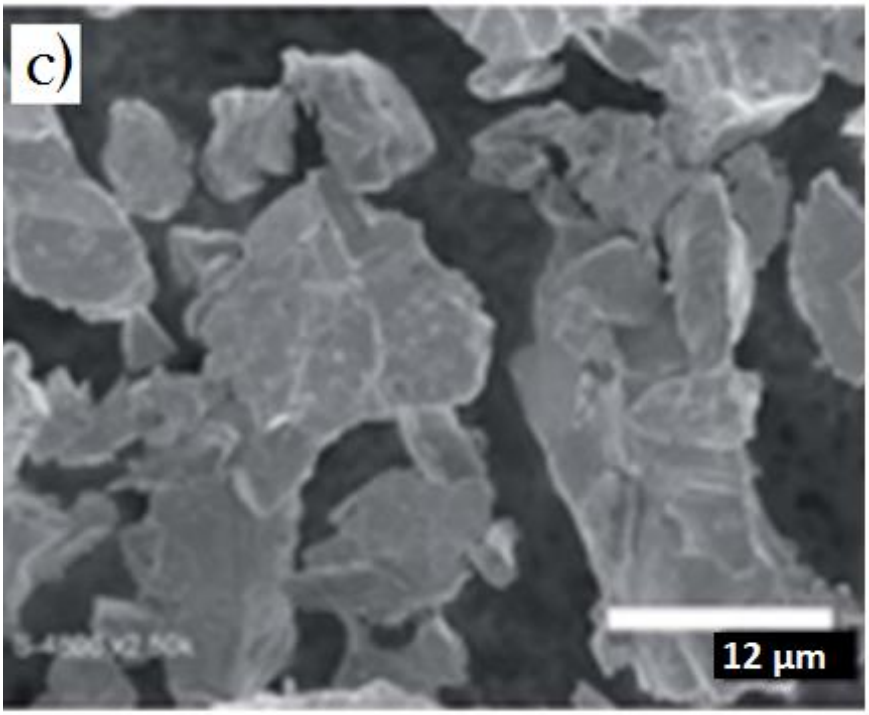

Fig. 4.1.1 (a) XRD patterns, (b) SAED pattern and (c) SEM image of SnSb prepared by microwave synthesis. β-Sn XRD peaks are indicated by stars.

area electron diffraction (SAED) pattern (Fig. 4.1.1b) shows two rings: the inner ring corresponds to the (200) plane and the outer ring corresponds to the (220) plane of SnSb (JCPDS No. 33-0118). SEM image revealed a particle size of about 10 – 60 µm, as shown in Fig. 4.1.1c.

Fig. 4.1.2 shows the voltage variations of SnSb/Li cell vs number of Li^+ (x) for the first cycle at C/20 in the potential window of 0.01 – 1.75 V vs Li/Li^+. As described in previous works, Li^+ reacts reversibly with SnSb by alloying/dealloying mechanism according to Eqs. (4.1.1 and 4.1.2) [10, 18-20].

$$3Li^+ + SnSb + 3e^- \rightleftharpoons Li_3Sb + Sn \qquad (4.1.1)$$

$$xLi^+ + Sn + xe^- \rightleftharpoons Li_xSn \qquad (x \sim 4.4) \qquad (4.1.2)$$

During the first discharge, the voltage profile can be divided into three different steps: (i) the initial alloying of SnSb with Li^+ to form Li_3Sb and Sn at potential plateau around 0.8 V [14, 18, 20], (ii) followed by three shorter plateaus at 0.68, 0.58 and 0.44 V corresponding to Li_2Sn_5, LiSn, and $Li_{13}Sn_5$, respectively, (iii) this followed by a less well

defined process between 0.37 and 0.01 V corresponding to Li_7Sn_2, and $Li_{22}Sn_5$, respectively [10, 19, 21].

During the following charge, all processes seem to be reversible, with 5 different steps occurring between 0.01 and 1.75 V, with 3 shorter plateaus from 0.58 to 0.78 V and the last processes from 0.97 to 1.03 V. The length of all the processes is more or less similar to those observed during the first discharge. However, the process at low potential is slightly shortened on charge. This difference is likely due to the irreversible reaction of Li^+ with electrolyte degradation products to form SEI layer. Moreover, while the last plateau on charge has quite the same length of the first one in discharge, a more accurate view shows the presence of two adjacent plateaus at 0.97 V (a-1) and 1.03 V (a-2'), suggesting a two-step dealloying behaviour of Li_3Sb as described recently in the [10].

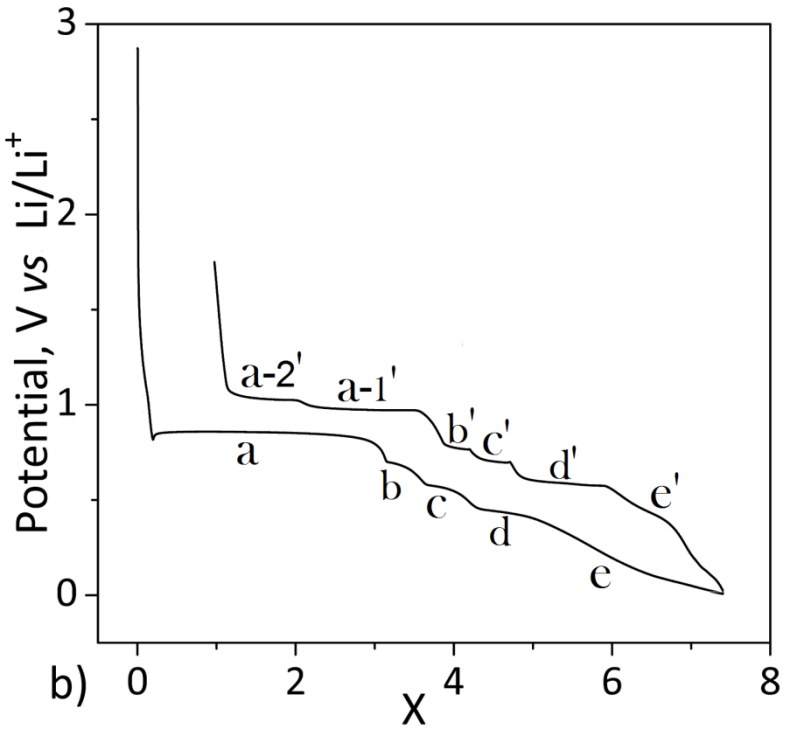

Fig. 4.1.2 Galvanostatic profile of SnSb/Li cell vs number of $Li^+(x)$ at C/20 for the first cycle.

Fig. 4.1.3 shows the cyclic voltammogram (CV) recorded for the first-five and 20th cycle, respectively. In agreement with previous studies, the electrochemical reactivity of the SnSb alloy is confirmed by the presence of five peaks during the first cycle. The broad

peak at 0.7 V is attributed to the first alloying reaction of Li^+ with SnSb to form Li_3Sb and the formation of SEI layer. The peaks at 0.5 V and 0.6 V correspond to the lithiation of Sn to form Li_xSn. Five distinct peaks were obtained during the first anodic scan. The peaks at 0.45 V, 0.7 V, 0.75 V, and 0.8 V are attributed to the delithiation of Li_xSn alloy to form Sn. Delithiation of Li-Sb alloy occur at potential around 1 V. The anodic/cathodic peaks were reversibly obtained for the first five cycles. However, the peak intensity corresponding to lithium reaction with Sb is diminishing resulting in the loss of capacity contribution from Sb. This capacity fading is attributed to the pulverization of the active material (due to the large volume change during cycling) and the formation of SEI layer. The formation mechanism of SEI layer during the first cycle will be described in chapter 5. Furthermore, the disintegration of SnSb electrode and evolution of the SEI layer during cycling have been also studied.

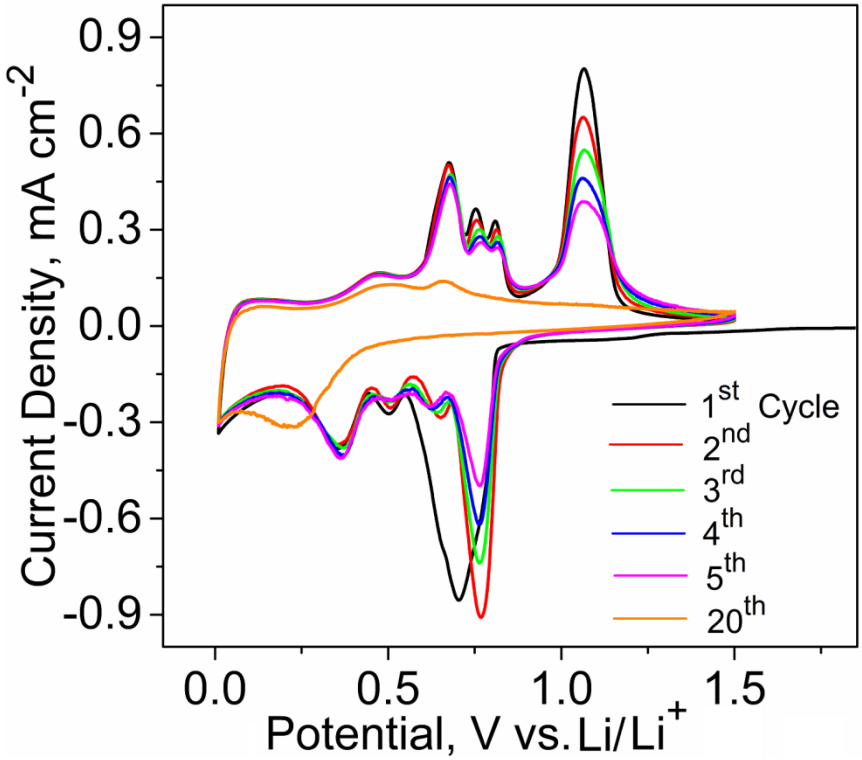

Fig. 4.1.3 Cyclic voltammogram recorded for the SnSb electrode in the potential window of 0.01 – 1.75 V vs Li/Li^+ at the scan rate of 0.1 mV s^{-1}.

Fig. 4.1.4 shows the galvanostatic charge-discharge profiles of the SnSb electrode in a lithium cell for 50 cycles at C/20. The multi-plateau behavior reflects the characteristics

of the electrochemical process which is associated with various lithium alloying–lithium dealloying stages. The voltage profiles of SnSb show distinct plateaus in the first several discharge cycles, reflecting the crystallinity and morphology of SnSb in the starting electrode (Fig.4.1.1). The potential differences between the anodic and cathodic plateaus for the first cycle compared to the second cycle indicate the bigger electrode polarization. This is attributed to the comparatively low lithium diffusion rate in the first discharge process [17, 19]. In the following cycles, the profile tends to be more sloping, indicating the structure transformation of SnSb composite from high-crystallinity to less-crystallinity or amorphous state. The Sb/Li_3Sb alloying/dealloying plateaus are shrinking, while the process ascribable to the lithiation of tin profiles tends to be more sloping, which is attributed to the slower diffusion rates of Li^+ [17].

Fig. 4.1.4b shows the cycle stability of SnSb electrode up to 50 cycles. The values of discharge capacities were found to be 833, 801, and 355 mAh g^{-1} for the 1st, 2nd, and 50th cycle. The low initial capacity loss (32 mAh g^{-1} ~ 4 %) is attributed to the micron sized particle size of the active material which creates lower active surface area for contact with electrolyte leading in less SEI film formation and fewer reaction of Li^+ with surface impurity, especially oxides [9, 17]. In addition, the crystallinity of SnSb particles

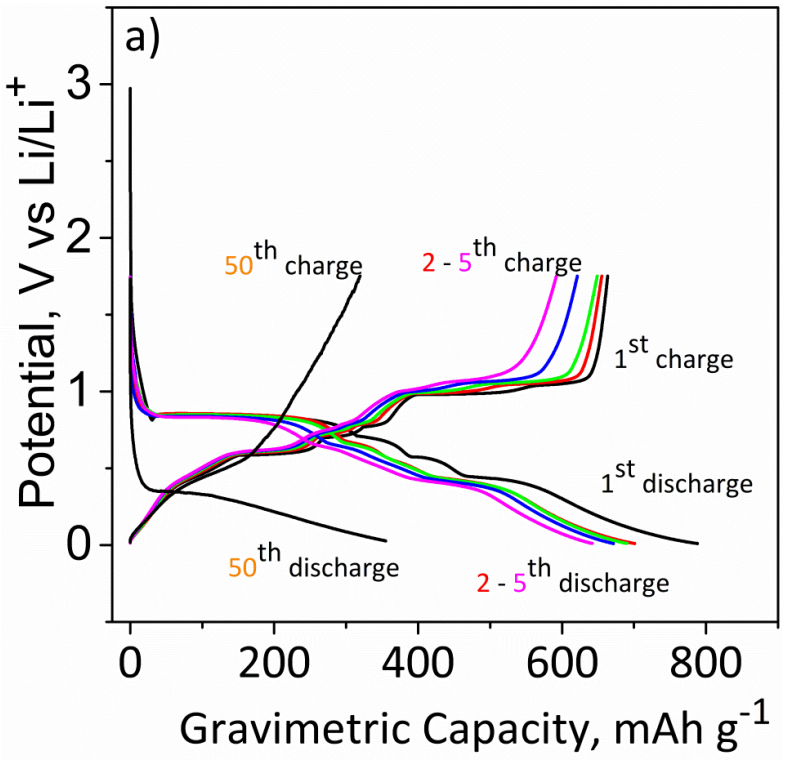

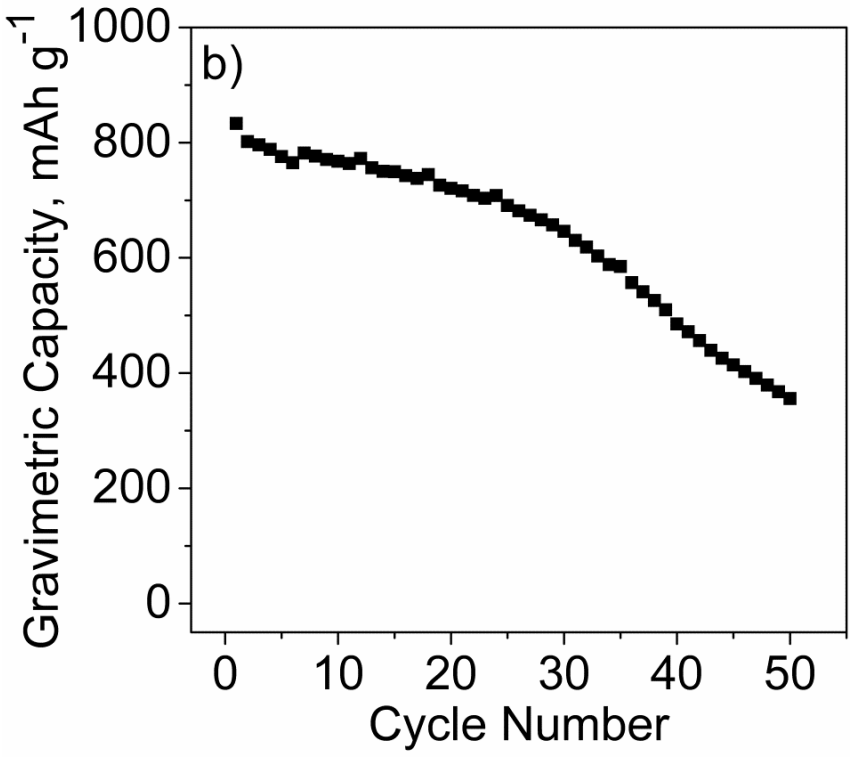

Fig. 4.1.4 (a) Galvanostatic discharge−charge profile and (b) capacity retention of SnSb at C/20.

promotes to some extent the tolerance to the large volume change during alloying/dealloying suggesting the large amount of grain-boundaries inside the particles may relieve the mechanical stress by grain-boundary slipping and thus preventing the complete cracking of larger particles [17, 21-23]. A stable capacity upon cycling can be observed with a reasonable fading of around 13.5 % of the capacity after the first 20 cycles. After the 25th cycle, the capacity starts to fade significantly and a capacity value of 355 mAh g^{-1} is obtained after 50 cycles. The phenomenon of stable capacity for initial stages followed by a strong fading has been observed with other reported SnSb electrodes [10, 16, 24].

4.1.4 Conclusion

The electrochemical performance of micro-sized SnSb alloy was studied. A high-specific capacity (ca. 833 mAh g^{-1}) and a good cycling stability up to 20 cycles were obtained. The initial irreversible capacity as low as ~ 4 % is attributed to the low-specific surface area of synthesized SnSb particles. The large amounts of grain boundaries existing inside

the polycrystalline SnSb particles are considered to be able to relieve the mechanical stress caused by the big volume changes, prevent the complete cracking of particles and thus stabilize the structure of electrode. However, the capacity faded very quickly after the 25 cycles attributed to the disintegration of the electrode material due to the mechanical stress caused by the large volume change during lithium alloying and dealloying mechanism. Furthermore, the cracking of the electrode surface create new surfaces, which leads to the electrolyte decomposition promoting the SEI growth. The loss of electrical contact and active material combined with formation of passive layer is responsible for the overall poor electrochemical performance.

4.1.5 References

[1] J.-M. Tarascon, M. Armand, Issues and challenges facing rechargeable lithium batteries, Nature, 414 (2001) 359-367.

[2] M. Armand, J.-M. Tarascon, Building better batteries, Nature, 451 (2008) 652-657.

[3] P. Poizot, S. Laruelle, S. Grugeon, L. Dupont, J.M. Tarascon, Searching for new anode materials for the Li-ion technology: time to deviate from the usual path, J. Power Sources, 97–98 (2001) 235-239.

[4] B.L. Ellis, P. Knauth, T. Djenizian, Three-Dimensional Self-Supported Metal Oxides for Advanced Energy Storage, Adv. Mater., 26 (2014) 3368-3397.

[5] S. Goriparti, E. Miele, F. De Angelis, E. Di Fabrizio, R. Proietti Zaccaria, C. Capiglia, Review on recent progress of nanostructured anode materials for Li-ion batteries, J. Power Sources, 257 (2014) 421-443.

[6] C. Liang, M. Gao, H. Pan, Y. Liu, M. Yan, Lithium alloys and metal oxides as high-capacity anode materials for lithium-ion batteries, J. Alloy. Compd., 575 (2013) 246-256.

[7] C.-M. Park, J.-H. Kim, H. Kim, H.-J. Sohn, Li-alloy based anode materials for Li secondary batteries, Chem. Soc. Rev., 39 (2010) 3115-3141.

[8] S. Needham, G. Wang, H. Liu, Electrochemical performance of SnSb and Sn/SnSb nanosize powders as anode materials in Li-ion cells, J. Alloy. Compd., 400 (2005) 234-238.

[9] M. Wachtler, J.O. Besenhard, M. Winter, Tin and tin-based intermetallics as new anode materials for lithium-ion cells, J. Power Sources, 94 (2001) 189-193.

[10] P. Antitomaso, B. Fraisse, L. Stievano, S. Biscaglia, D. Aymé-Perrot, P. Girard, M.T. Sougrati, L. Monconduit, SnSb electrodes for Li-ion batteries: the electrochemical mechanism and capacity fading origins elucidated by using operando techniques, J. Mater. Chem. A, 5 (2017) 6546-6555.

[11] M. Winter, J.O. Besenhard, Electrochemical lithiation of tin and tin-based intermetallics and composites, Electrochim. Acta, 45 (1999) 31-50.

[12] O. Crosnier, X. Devaux, T. Brousse, P. Fragnaud, D. Schleich, Influence of particle size and matrix in “metal” anodes for Li-ion cells, J. Power Sources, 97 (2001) 188-190.

[13] M. Wachtler, M. Winter, J.O. Besenhard, Anodic materials for rechargeable Li-batteries, J. Power Sources, 105 (2002) 151-160.

[14] J. Yang, M. Wachtler, M. Winter, J.O. Besenhard, Sub-Microcrystalline Sn and Sn-SnSb Powders as Lithium Storage Materials for Lithium-Ion Batteries, Electrochem. Solid-State Lett., 2 (1999) 161-163.

[15] P. Antitomaso, B. Fraisse, M. Sougrati, F. Morato-Lallemand, S. Biscaglia, D. Aymé-Perrot, P. Girard, L. Monconduit, Ultra-fast dry microwave preparation of SnSb used as negative electrode material for Li-ion batteries, J. Power Sources, 325 (2016) 346-350.

[16] L. Simonin, U. Lafont, E. Kelder, SnSb micron-sized particles for Li-ion batteries, J. Power Sources, 180 (2008) 859-863.

[17] H. Zhao, Z. Zhu, C. Yin, H. Guo, D.H. Ng, Electrochemical characterization of micro-sized Sb/SnSb composite anode, Mater. Chem. Phys., 110 (2008) 201-205.

[18] F.J. Fernández-Madrigal, P. Lavela, C.P. Vicente, J.L. Tirado, J.C. Jumas, J. Olivier-Fourcade, X-ray diffraction, ^{7}Li MAS NMR spectroscopy, and ^{119}Sn Mössbauer spectroscopy study of SnSb-based electrode materials, Chem. Mater., 14 (2002) 2962-2968.

[19] H. Zhao, C. Yin, H. Guo, W. Qiu, Microcrystalline SnSb alloy powder as lithium storage material for rechargeable lithium-ion batteries, Electrochem. Solid-State Lett., 9 (2006) A281-A284.

[20] L. Aldon, A. Garcia, J. Olivier-Fourcade, J.-C. Jumas, F.J. Fernández-Madrigal, P. Lavela, C.P. Vicente, J.L. Tirado, Lithium insertion mechanism in Sb-based electrode materials from ^{121}Sb Mössbauer spectrometry, J. Power Sources, 119 (2003) 585-590.

[21] H. Mukaibo, T. Osaka, P. Reale, S. Panero, B. Scrosati, M. Wachtler, Optimized Sn/SnSb lithium storage materials, J. Power Sources, 132 (2004) 225-228.

[22] T. Watanabe, S. Tsurekawa, Toughening of brittle materials by grain boundary engineering, Mater. Sci. Eng., A, 387 (2004) 447-455.

[23] A. Trifonova, M. Wachtler, M. Wagner, H. Schroettner, C. Mitterbauer, F. Hofer, K.-C. Möller, M. Winter, J. Besenhard, Influence of the reductive preparation conditions on the morphology and on the electrochemical performance of Sn/SnSb, Solid State Ionics, 168 (2004) 51-59.

[24] A. Birrozzi, F. Maroni, R. Raccichini, R. Tossici, R. Marassi, F. Nobili, Enhanced stability of SnSb/graphene anode through alternative binder and electrolyte additive for lithium ion batteries application, J. Power Sources, 294 (2015) 248-253.

4.2 Anodized Ti_3SiC_2 As an Anode Material for Li-ion Batteries

The work presented in this section was done in collaboration between Aix-Marseille University and Drexel University (Y. Gogotsi group). The work was published in ACS Applied Materials and Interfaces (DOI: 10.1021/acsami.6b03528) and Electrochemistry Communications (doi.org/10.1016/j.elecom.2017.05.010).

4.2.1 Introduction

Among all negative electrode materials, transition metal oxides have attracted some attention due to their relatively high potentials compared to Li/Li^+. They can react reversibly with Li^+ via intercalation, conversion, and/or alloying mechanisms [1-3]. Their performance in terms of energy and power densities can be drastically improved by using nanomaterials (nanotubes, nanowires, nanoporous particles, etc.) [4-7]. As an example, vertical arrays of titania nanotubes and derivatives, obtained by the anodization of Ti, exhibit high capacity retention and rate capabilities for potential applications in 3D Li-ion microbatteries (μLIBs) [8-15].

The MAX phases ($M_{n+1}AX_n$: where n = 1, 2, or 3; M is an early transition metal; A is an A-group element, mostly elements of group 13 – 14; and the X is carbon and/or nitrogen [16]) are a family of 70+ ternary compounds of carbides and nitrides, with a hexagonal layered structure. These phases combine some properties that are quintessential to both metals and ceramics. Since Barsoum and El-Raghy [17] reported on the synthesis of pure, bulk polycrystalline Ti_3SiC_2 and characterized it, there has been renewed interest in the MAX phases and, more recently, their derivatives MXenes [18]. To convert MAX to MXene, the A element – typically Al – is selectively etched in solutions containing hydrofluoric acid (HF). MXenes have shown good potential for use in energy storage and conversion applications such as LIB electrode materials [19-21], Li–S batteries [22], supercapacitors [23, 24], and fuel cells [25].

Even more recently, it has been demonstrated that, under the right electrochemical conditions, either both the M and A elements can be etched away, leaving behind a

carbide derived carbon [26], or only the M element can be etched away, leaving behind AX 2D materials such as C−S laminates [27].

This section expands on this idea of electrochemical etching. Herein anodization of Ti_3SiC_2 was performed in a HF containing electrolyte to produce a hybrid material based on titania carrying some silica and carbon. The effects of the electrochemical anodization parameters on the morphological, structural and electrochemical properties of the anodized Ti_3SiC_2 (henceforth referred to as A-Ti_3SiC_2) were studied. A detailed electrochemical study has been conducted to explain the enhanced electrochemical performance of A-Ti_3SiC_2 with tailored morphologies.

4.2.2 Experimental Section

A fully dense Ti_3SiC_2 billet was fabricated by mixing titanium, graphite, and silicon carbide powders in a stoichiometric Ti/Si/C ratio of 3:1:2. The mixed powders were then hot pressed at 1600 °C for 4 h under a load corresponding to a pressure of 40 MPa [17].

The anodization took place in a two-electrode electrochemical cell (Fig. 4.2.1) with a Ti_3SiC_2 disc and platinum foil as the working and counter electrodes, respectively. The working Ti_3SiC_2 electrode was sealed with a rubber ring, so that the area exposed to the electrolyte was 0.39 cm^2. The formation of a porous Ti_3SiC_2 was achieved electrochemically by anodizing the fully dense Ti_3SiC_2 at anodic potential in an aqueous electrolyte containing fluoride ions. The latter consisted of a mixture of 1 M sodium hydroxide (99.9 wt. %, Carlo Erba, France) and 1 M phosphoric acid (68 wt. %, Pro-Lab, France) containing hydrofluoric acid (40 wt. %, Pro-Lab, France). Various oxide morphologies were produced by varying the anodization parameters.

(i) *Applied potential:* Anodic applied potentials leading to high electrical fields (> 10 V/µm) are required to ensure the migration of oxidized species and achieve the formation of a thick oxide layer. The effect of applied potential was studied by anodizing Ti_3SiC_2 in aqueous electrolyte containing 0.1 % vol. HF for 3 h at a potential of 10, 30, and 60 V, respectively.

(ii) *Anodization time:* The effect of anodization time was studied by anodizing Ti_3SiC_2 in aqueous electrolyte containing 0.1 vol. % HF at 60 V for 1, 2, and 3 h.

(iii) *Electrolyte fluoride content:* The effect of fluoride content was studied by anodizing Ti_3SiC_2 at 60 V for 3 h in aqueous electrolyte containing 0.1 and 2 vol. % HF.

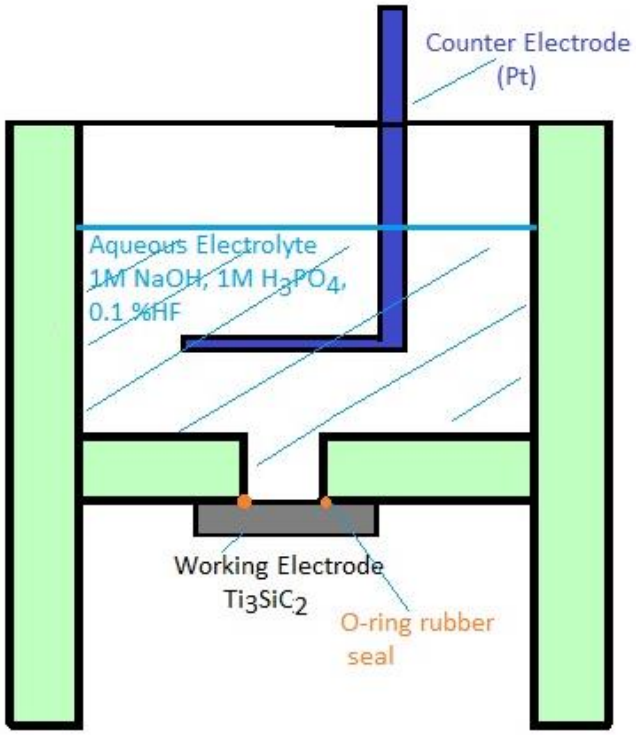

Fig. 4.2.1 Schematic of the electrochemical cell used for the anodization of Ti_3SiC_2.

After anodization, the samples were quickly rinsed with deionized (DI) water and dried at 80 ^{0}C under vacuum using a BUCHI Glass Oven B-585 and a BUCHI Vacuum controller V-800. To form the anatase phase, the A-Ti_3SiC_2 was further annealed in air at 450 ^{0}C for 3 h with a heating rate of 5 ^{0}C min^{-1}.

The electrochemical performance tests (cyclic voltammetry (CV) and galvanostatic charge−discharge) were performed using standard, two-electrode Swagelok cells that were assembled in a glovebox filled with high purity argon (Ar), in which the oxygen and humidity contents were < 2 ppm. A 9 mm diameter Li foil was used as the reference electrode. A Whatman glass microfiber separator (9 mm in diameter) was soaked in the electrolyte of lithium hexafluorophosphate in ethylene carbonate (EC) and diethylene carbonate (DEC) electrolyte (1 M $LiPF_6$ in EC/DEC of 1:1 w/w) before assembling the cell.

For all the electrochemical tests, the Ti_3SiC_2 discs were used as working electrodes with no additives (i.e., neither binder nor carbon additives were needed). Galvanostatic charge/discharge curves were obtained at an applied current density of 200, 300, and 500 µA cm^{-2}, in the 1 – 3 V vs Li/Li^+ potential range. To study the Li^+ storage mechanism, the CV experiments were carried out at various scan rates (0.05 – 1.3 mV s^{-1}) in the potential window of 1 – 3 V vs Li/Li^+.

4.2.3 Results and Discussion

4.2.3.1 Electrode Fabrication

Fig. 4.2.2 shows the chronoamperometric curves of Ti_3SiC_2 anodized for 3 h in aqueous electrolyte containing 0.1 vol. % HF at applied potentials of 10, 30, and 60 V. In agreement with the electrochemical growth of porous titania [28], the anodic current dropped with time as soon as the anodization started due to the formation of an electrical barrier formed by a compact oxide layer. Then, the current density increased slightly, presumably as a result of an increase in surface area as a result of the

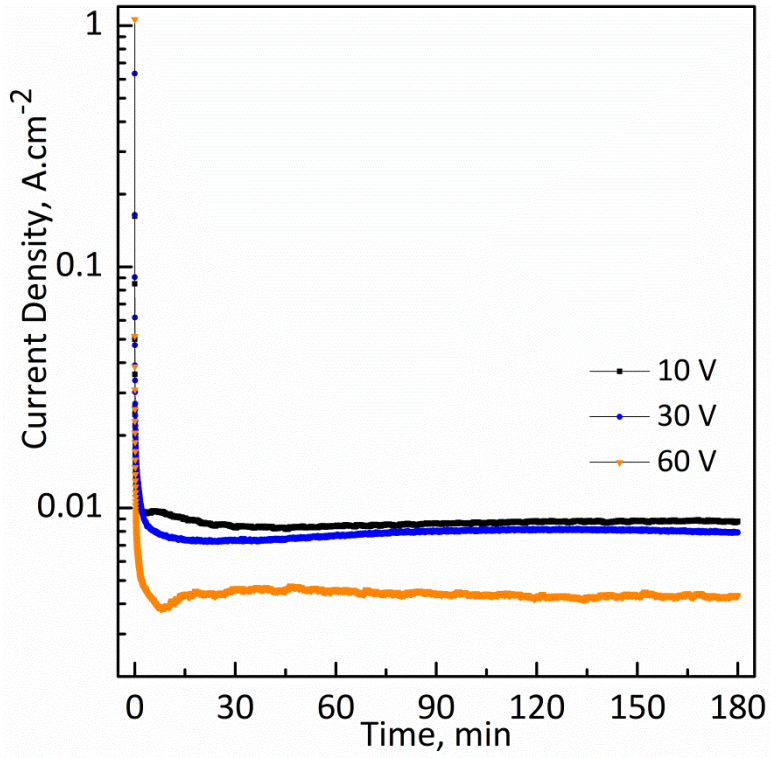

Fig. 4.2.2 Chronoamperometric curves of A-Ti_3SiC_2 at applied potentials of 10, 30, and 60 V.

nucleation and growth of pores. Finally, steady current densities were achieved when equilibrium was established between the growth and dissolution of the oxide layers. Note that the current density decreases with increasing applied potential, suggesting that the higher the potential, the thicker the porous oxide layer. This was indeed confirmed by cross-sectional SEM images (Fig. 4.2.3 a and b) from which the porous layer thicknesses were estimated to be around 3 and 21 µm at 10 and 60 V, respectively. Furthermore, examination of the TEM image in Fig. 4.2.3c revealed that Ti_3SiC_2 was not completely anodized but only covered by a thin oxide layer with a mean thickness of 25 nm on the basal plane of Ti_3SiC_2.

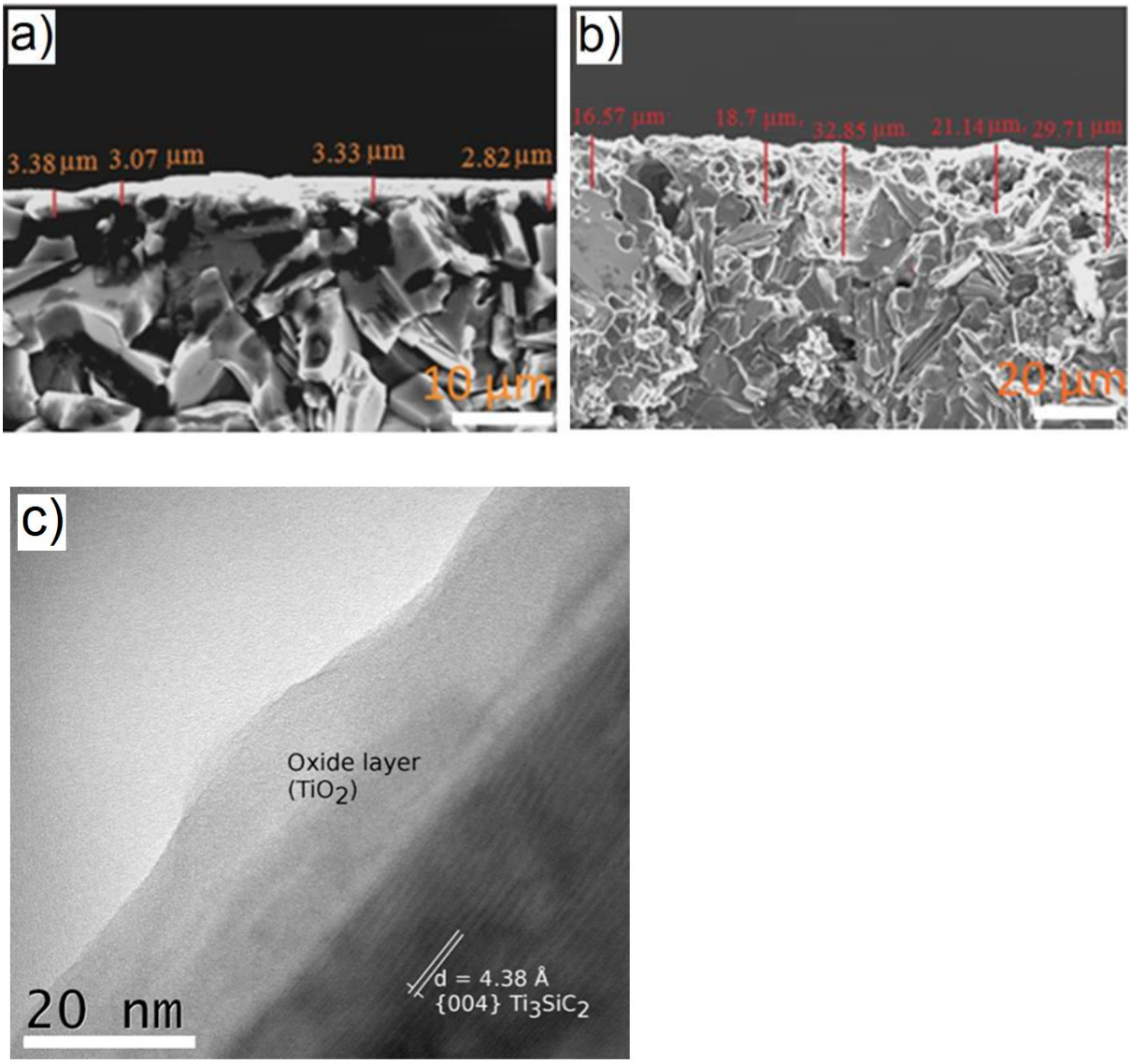

Fig. 4.2.3 Cross-sectional SEM images of Ti_3SiC_2 anodized at potential of 10 V (a) and 60 V (b) for 3h. (c) TEM image of Ti_3SiC_2 anodized at 60 V for 3 h.

Because this is the first report on the anodization of Ti_3SiC_2, there are no other studies with which to compare our results. However, there are some similarities with Ti anodization that are instructive. Similar to Ti, during the anodization process, a porous oxide layer under steady-state conditions becomes of constant thickness, as a result of two competitive reactions, viz. oxide formation and chemical dissolution [28-30]. When Ti_3SiC_2 is anodized in aqueous electrolytes, an oxide layer composed of TiO_2 and SiO_2 grows at the surface according to Eqs. (4.2.1 and 4.2.2).

$$Ti + 2H_2O \rightarrow TiO_2 + 4H^+ + 4e^- \quad (4.2.1)$$

$$Si + 2H_2O \rightarrow SiO_2 + 4H^+ + 4e^- \quad (4.2.2)$$

Simultaneously, slow oxide dissolution occurs due to the presence of fluoride ions [28]. The formation of TiF_6^{2-} and SiF_6^{2-} complexes, which are soluble in aqueous media, occurs according to Eqs. (4.2.3 and 4.2.4).

$$TiO_2 + 4H^+ + 6F^- \rightarrow TiF_6^{2-} + 2H_2O \quad (4.2.3)$$

$$SiO_2 + 4H^+ + 6F^- \rightarrow SiF_6^{2-} + 2H_2O \quad (4.2.4)$$

It is also known that metal atoms can be electrochemically etched out of select MAX structures using dilute HF [26, 27].

As noted above, the morphology and thickness of an oxide formed by anodization are dictated by a competition between its electrochemical growth and its chemical dissolution, both of which are strongly affected by the applied potential, fluoride ion content in the electrolyte and anodization time.

4.2.3.1.1 Effect of Applied Potential

Different potential values of 10, 30, and 60 V were applied to study the effect of thermodynamics on the oxide morphology. High-magnification SEM images of the Ti_3SiC_2 anodized for 3 h at 10, 30, and 60 V, in a 0.1 vol. % HF containing electrolyte are shown in parts a, b, and c of Fig. 4.2.4, respectively. At an applied potential of 60 V, the oxide formation was the predominant process leading to the formation of a mesoporous structure (Fig. 4.2.4c). When the applied potential was lower, the Ti_3SiC_2 surface has

adopted a nanolayered morphology, which might be due to the partial etching of one of its elements (Fig. 4.2.4a and b) [31].

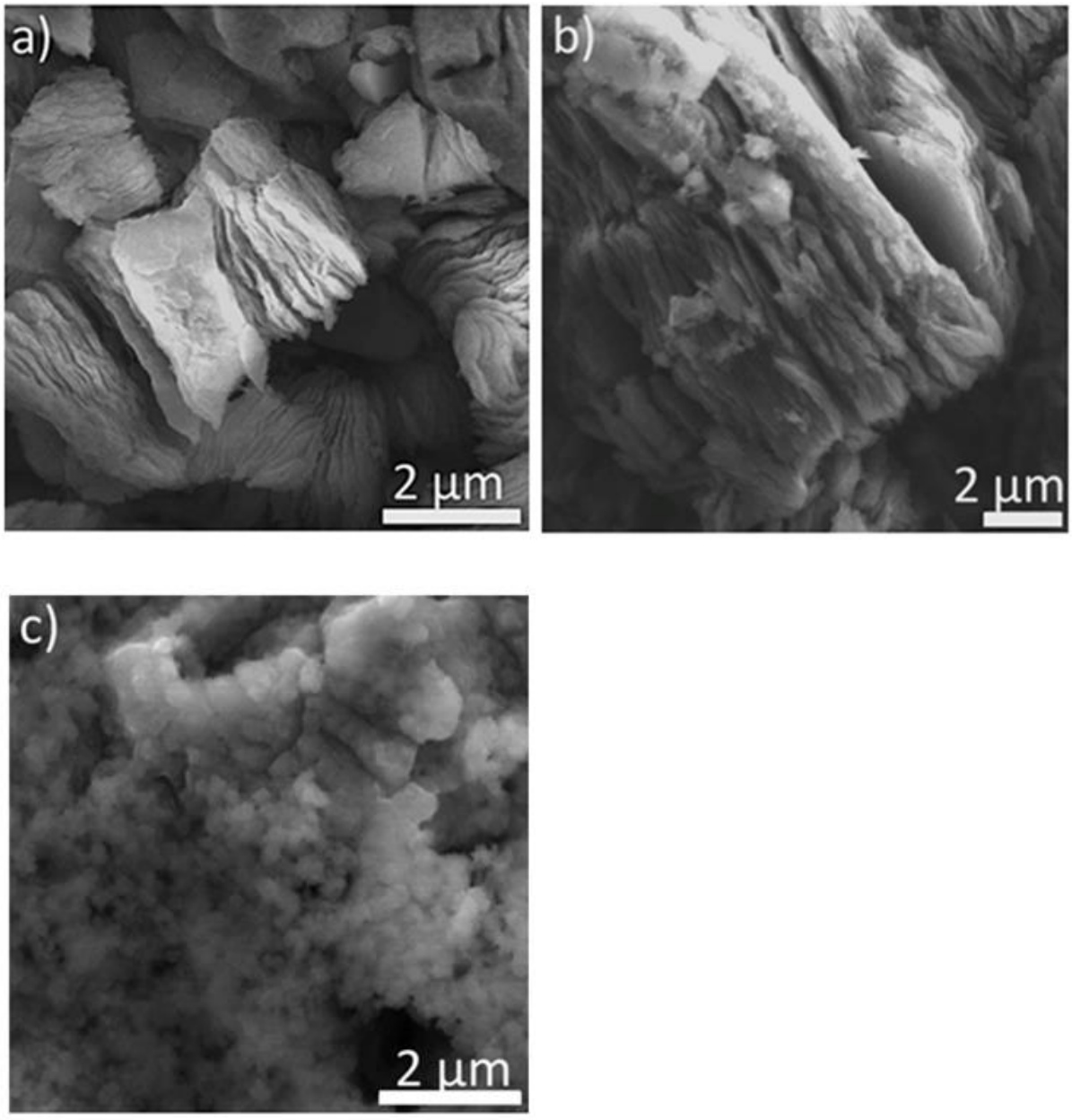

Fig. 4.2.4 SEM images of Ti_3SiC_2 anodized at applied potentials of (a) 10 V, (b) 30 V, and (c) 60 V for 3 h in aqueous solution containing 0.1 % vol. HF.

4.2.3.1.2 Effect of Fluoride Content

Part a and b of Fig. 4.2.5 shows the SEM images of Ti_3SiC_2 samples anodized at 60 V for 3 h in aqueous electrolyte containing 0.1 and 2 % vol. HF, respectively. There are two well defined conditions depending on the content of fluoride ions: (i) for a high

concentration, no oxide layer is obtained because Ti^{4+} will directly react with abundant fluoride ions to form water soluble TiF_6^{2-} and (ii) a compact oxide layer was obtained in the absence of fluoride ions . For intermediate concentration of HF, an oxide layer with different morphologies has been obtained. Nanolayered structure was obtained for low fluoride ion concentration (Fig. 4.2.5a), while a perforated oxide structure has been formed when the fluoride ion concentration is higher (Fig. 4.2.5b).

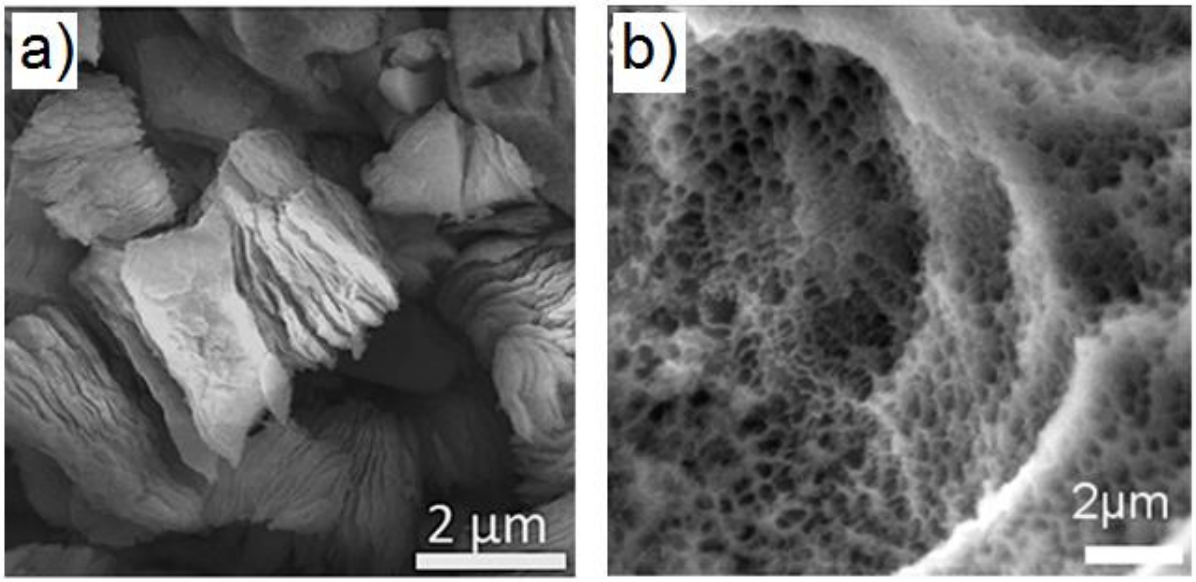

Fig. 4.2.5 SEM images of Ti_3SiC_2 anodized at applied potential of 60 V for 3 h in aqueous electrolyte containing 0.1 % vol. (a) and 2 % vol. (b) HF.

4.2.3.1.3 Effect of Anodization Time

Low-magnification SEM images of Ti_3SiC_2 anodized at 60 V in aqueous electrolyte containing 0.1 % vol. HF for 1, 2, and 3 h are shown in parts a, b, and c of Fig. 4.2.6, respectively. They show that porous morphologies are promoted when the anodization time was extended. One hour was insufficient to create pores, leading to a dense oxide layer (Fig. 4.2.6a). After 3 h anodization, however, a highly porous structure has grown (Fig. 4.2.6c).

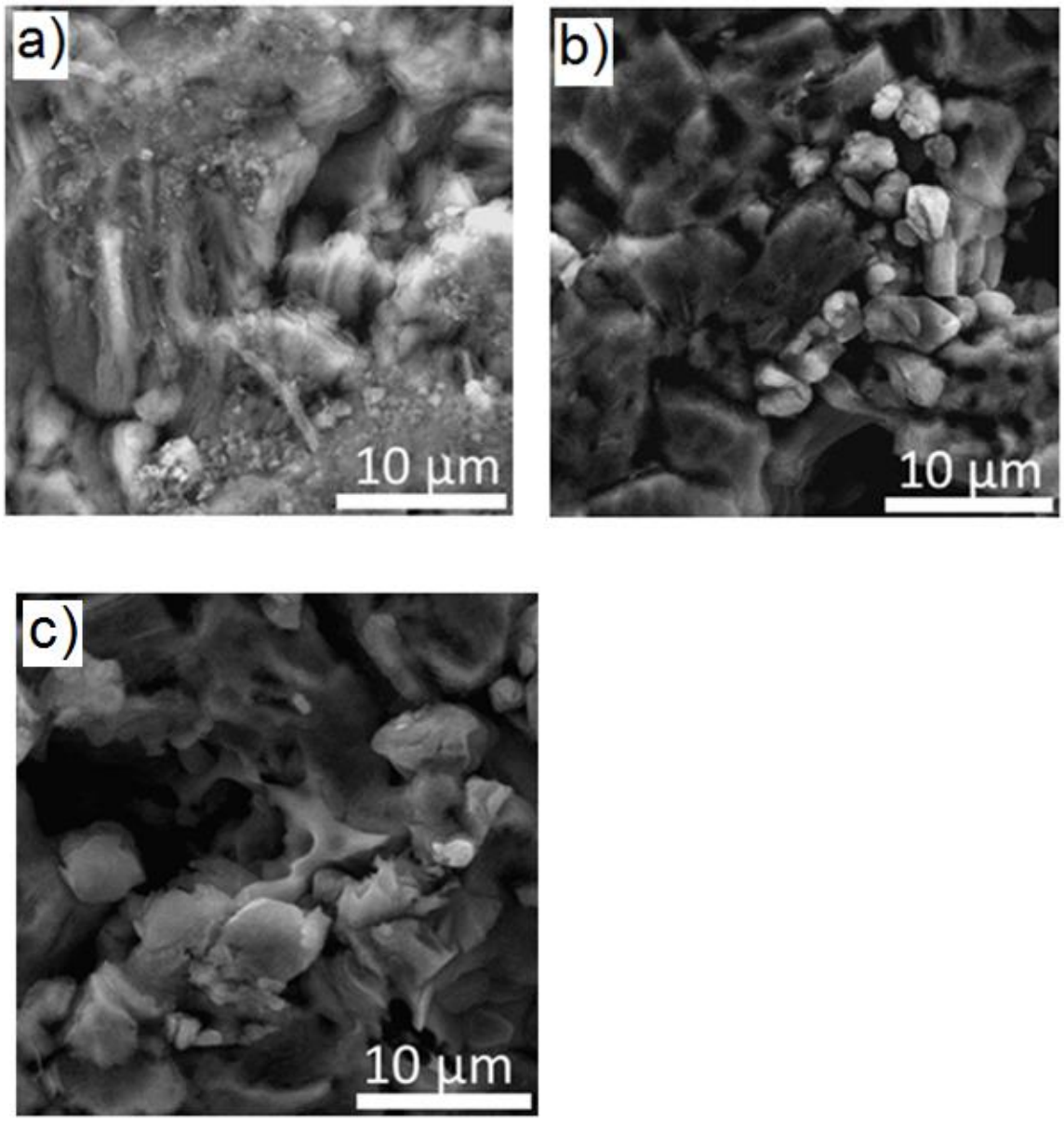

Fig. 4.2.6 Low-magnification SEM image of Ti_3SiC_2 anodized at applied potential of 60 V in aqueous electrolyte containing 0.1 % vol. HF for (a) 1 h, (b) 2 h, and (c) 3 h.

For further studies on the electrochemical performances of A- Ti_3SiC_2 an anodization time of 3 h (extended porous structure) and hydrofluoric acid concentration of 0.1 % vol. (various oxide morphologies were obtained by varying applied potential) was selected.

4.2.3.2 Characterization of A-Ti_3SiC_2

EDS analysis of the atomic and mass percentage of Ti, Si, C, and O in pristine and Ti_3SiC_2 anodized at 60 V, Ti_3SiC_2 (60 V) is provided in Table 4.2.1. The oxide formation is

evidenced by a significant increase in oxygen content. Moreover, the reduction of the Ti/Si atomic ratio from 3:1 to 3:0.7 upon anodization reveals that Si is preferentially dissolved. Under oxidizing conditions, HF is capable of selectively etch Si from SiC [32]. This can be attributed to the presence of HF, which is a well-known SiO_2 etchant [33]. Additionally, metallic Si−Ti bonds can be broken upon HF treatment, resulting in the selective etching of Si out of the MAX phase structure [34].

Table 4.2.1 Composition of Pristine and A-Ti_3SiC_2 Based on EDS Analysis

element	pristine Ti_3SiC_2		A-Ti_3SiC_2	
	mass %	atomic %	mass %	atomic %
C	12.04	32.6	12.94	29.46
O	0.78	1.59	15.95	27.25
Si	13.78	15.96	8.31	7.80
Ti	73.40	49.85	62.80	35.49
Total	100	100	100	100

The XRD patterns for pristine and A-Ti_3SiC_2, annealed at 450 ^{0}C for 3 h in air, is shown in Fig. 4.2.7a. The presence of new peaks at 25.19° and 48.01° correspond to the (101) and (200) reflections of anatase (Fig. 4.2.7 iii and iv), respectively. The anatase phase has a structure of tetragonal with the space group of $I4_1/amd$ and crystal size of 17 nm (JCPD file no. 21-1272). No peak could be assigned to SiO_2, suggesting that the SiO_2 formed was amorphous. As noted above, some silica could also have been dissolved by HF, leading to additional porosity after etching. It is worth noting that annealing of pristine (non-anodized) Ti_3SiC_2 using the same conditions (450 °C for 3 h in air) did not result in the formation of any crystalline phase (Fig. 4.2.7ii).

The predominance of anatase is confirmed by the Raman spectrum obtained from Ti_3SiC_2 (60 V) after annealing in air (Fig. 4.2.7b). Furthermore, the broad peaks

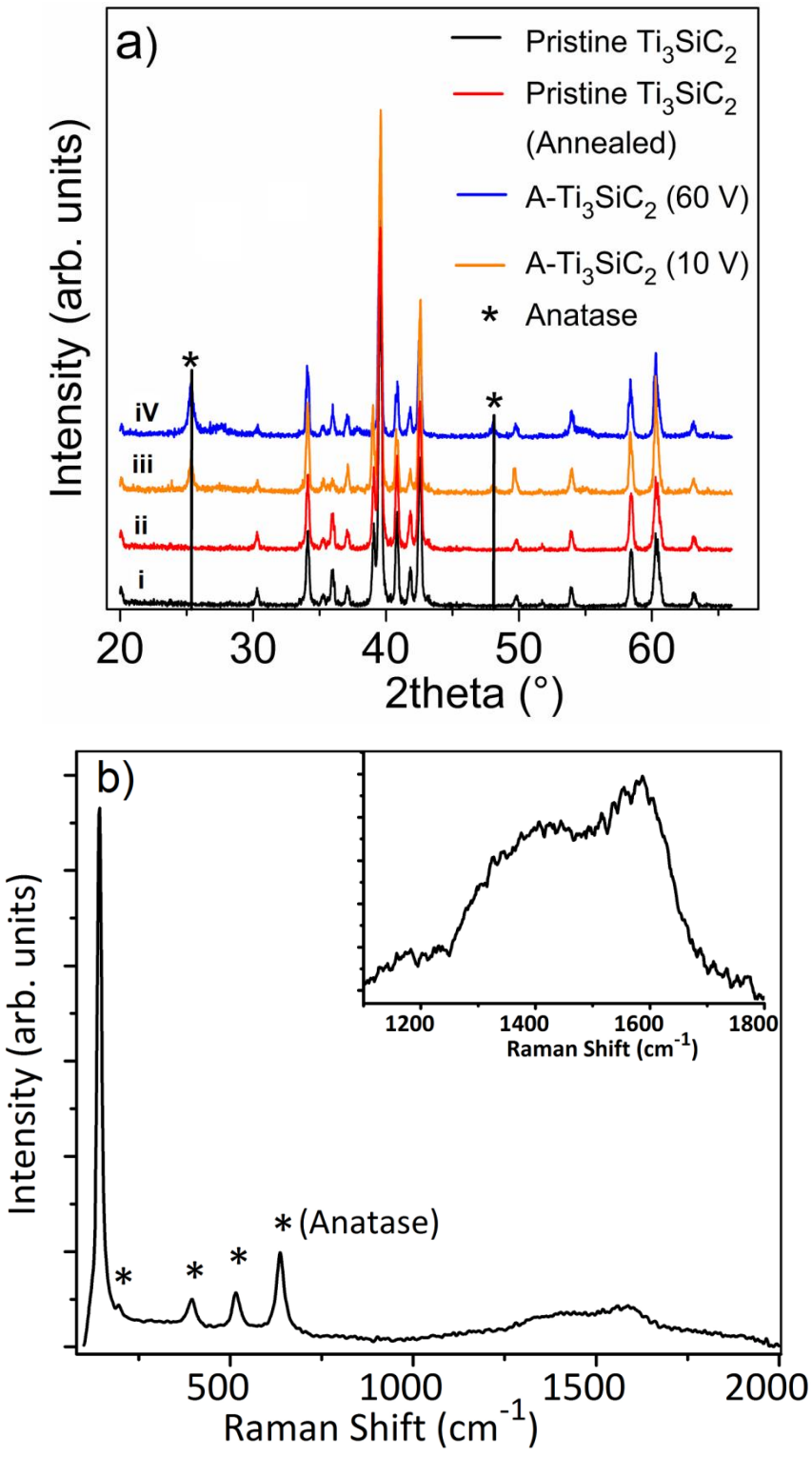

Fig. 4.2.7 (a) XRD patterns for the pristine material and Ti_3SiC_2 anodized at an applied potential of 10 and 60 V, then annealed in air at 450 °C for 3 h. (b) Raman spectrum of the A-Ti_3SiC_2 (60 V) showing anatase peaks. Inset shows the spectrum in the 1100 − 1800 cm^{-1} wavenumber range, D-band (1419 cm^{-1}), and G-band (1593 cm^{-1}).

corresponding to the D-band (1419 cm^{-1}) and G-band (1593 cm^{-1}) suggested that strongly disordered (amorphous) carbon carrying sp2 bonds with layered morphology was obtained after anodization (inset in Fig. 4.2.7b).

To gain more information on the chemical composition of the films formed, we carried out XPS analysis on a Ti_3SiC_2 surface anodized at 60 V for 3 h. Parts a, b, and c of Fig. 4.2.8 show high-resolution XPS spectra recorded in the Ti 2p, Si 2p, and C 1s regions, respectively. The high-resolution spectrum in the Ti 2p region (Fig. 4.2.8a) revealed a pronounced Ti(IV) oxide signal observed at ~ 459.1 eV, together with Ti−Si and Ti−C signals at 454.5 and 455.1 eV, respectively, arising from Ti atoms in the inner part of the Ti_3SiC_2 layers [35]. The presence of Ti−Si bonds was also confirmed by an asymmetric peak at ~ 99 eV, which can be deconvoluted into two symmetric peaks at 98.8 and 99.4 eV (ΔE = 0.63 eV) assigned to the Si 2p3/2 and Si 2p1/2 components of the signal, in the Si 2p region (Fig. 4.2.8b). More importantly, the peak at 102.6 eV evidenced the presence of SiO_2. Finally, deconvolution of the spectrum in the C 1s region (Fig. 4.2.8c) reveals peaks at 282.0 and 284.8 eV, which could be attributed to Ti−C and C−C bonds, respectively, together with C bonded to O showing up at higher binding energies. On the basis of XRD and XPS analysis, it can thus be concluded that the surface layer of A-Ti_3SiC_2 consists of anatase, amorphous SiO_2, and carbon.

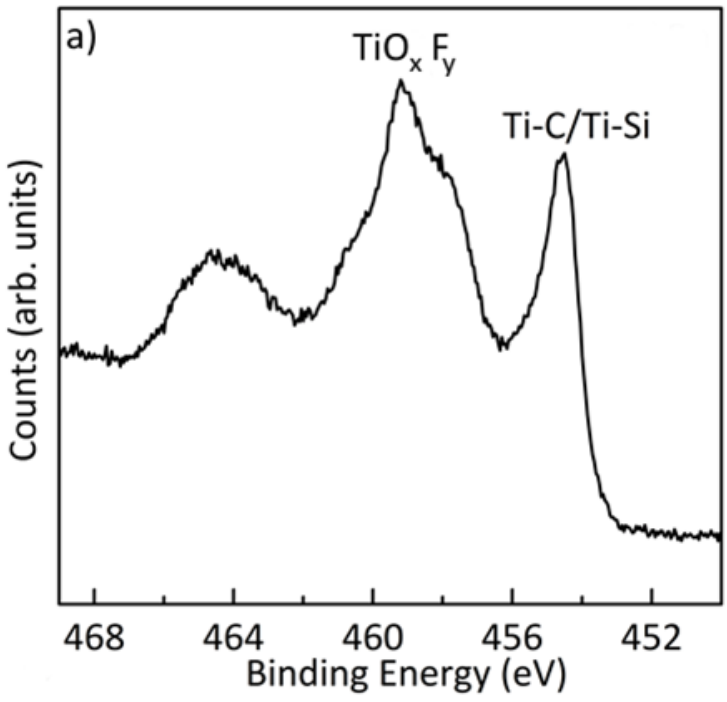

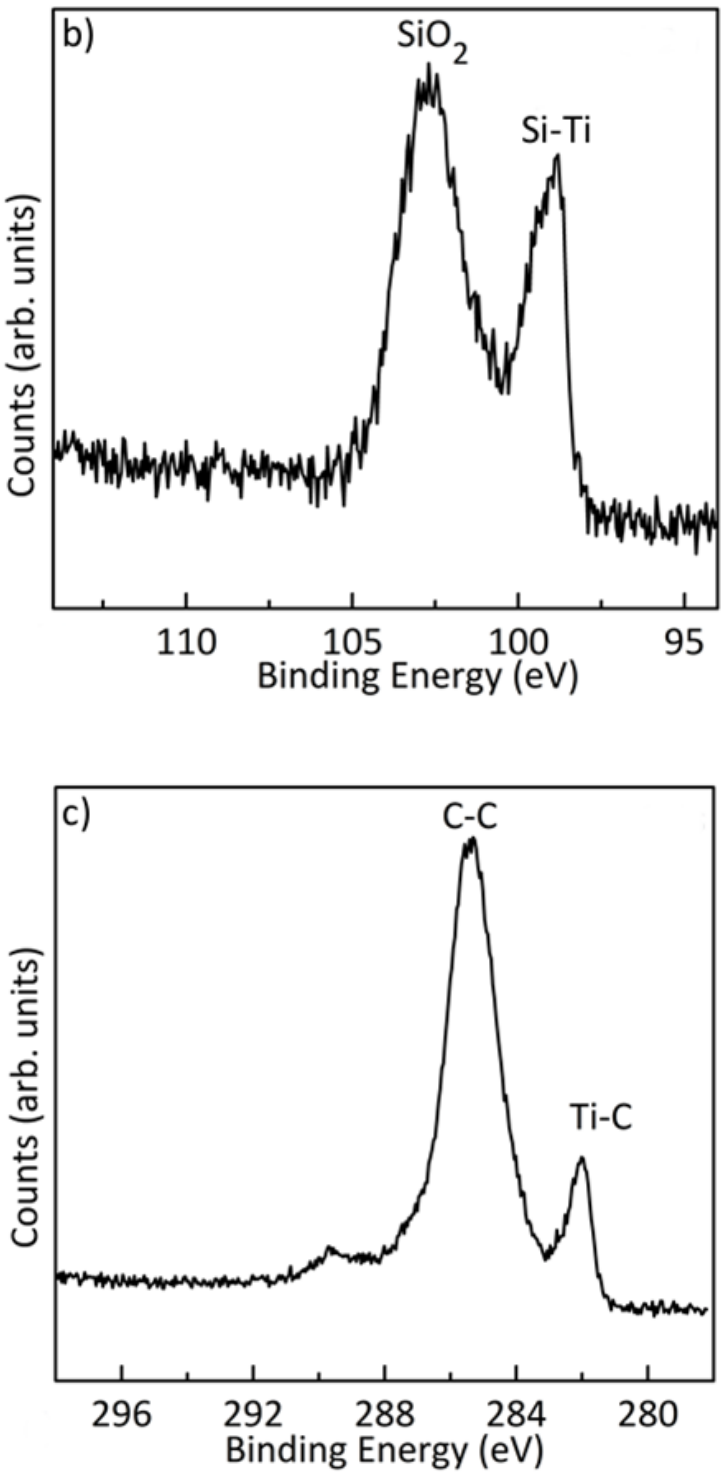

Fig. 4.2.8 High-resolution XPS spectra in the Ti 2p (a), Si 2p (b), and C 1s (c) regions for A-Ti_3SiC_2 (60 V).

The log differential intrusion volume of A-Ti_3SiC_2 as a function of pore diameter is given in Fig. 4.2.9. A-Ti_3SiC_2 (60 V) has an average pore size of 5 nm with a porosity of ~ 20 %. A-Ti_3SiC_2 (10 V) reveals 11 nm and 4 nm pores and an average porosity of 35 %.

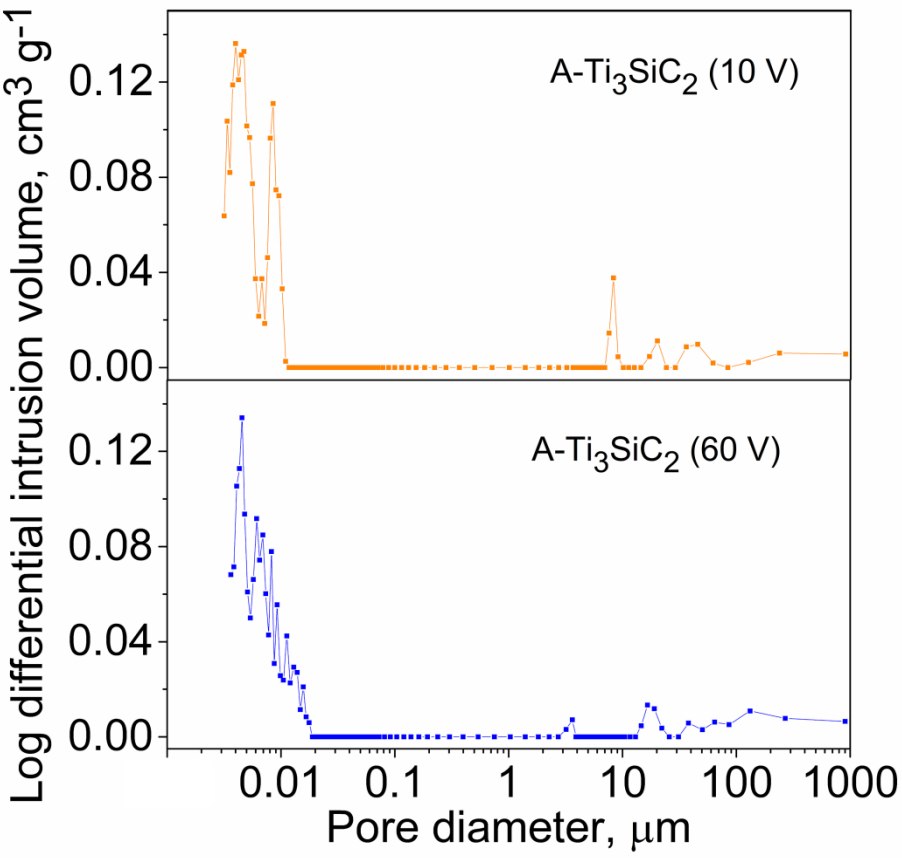

Fig. 4.2.9 The log differential intrusion volume as a function of pore diameter.

4.2.3.3 Electrochemical Characterization of A-Ti_3SiC_2

Fig. 4.2.10 compares the CVs obtained on pristine and anodized Ti_3SiC_2 at 10, 30, and 60 V, recorded at a scan rate of 1 mV s^{-1} between 1 and 3 V vs Li/Li^+. For the pristine sample, the enclosed area is small, and no peaks exist over the entire potential window, which implies that neither intercalation nor conversion reactions with Li^+ occurred. This result also shows that bulk Ti_3SiC_2 cannot accommodate Li ions and thus cannot be used as an active electrode material. In contrast, all CVs obtained from anodized A-Ti_3SiC_2 exhibit the cathodic and anodic peaks at 1.67 and 2.17 V vs Li/Li^+, respectively. These peaks are most probably associated with the reversible insertion and extraction of Li^+ in/from anatase according to Eq. (4.2.5) [36-40].

$$TiO_2 + xLi^+ + xe^- \leftrightarrows Li_xTiO_2 \qquad (4.2.5)$$

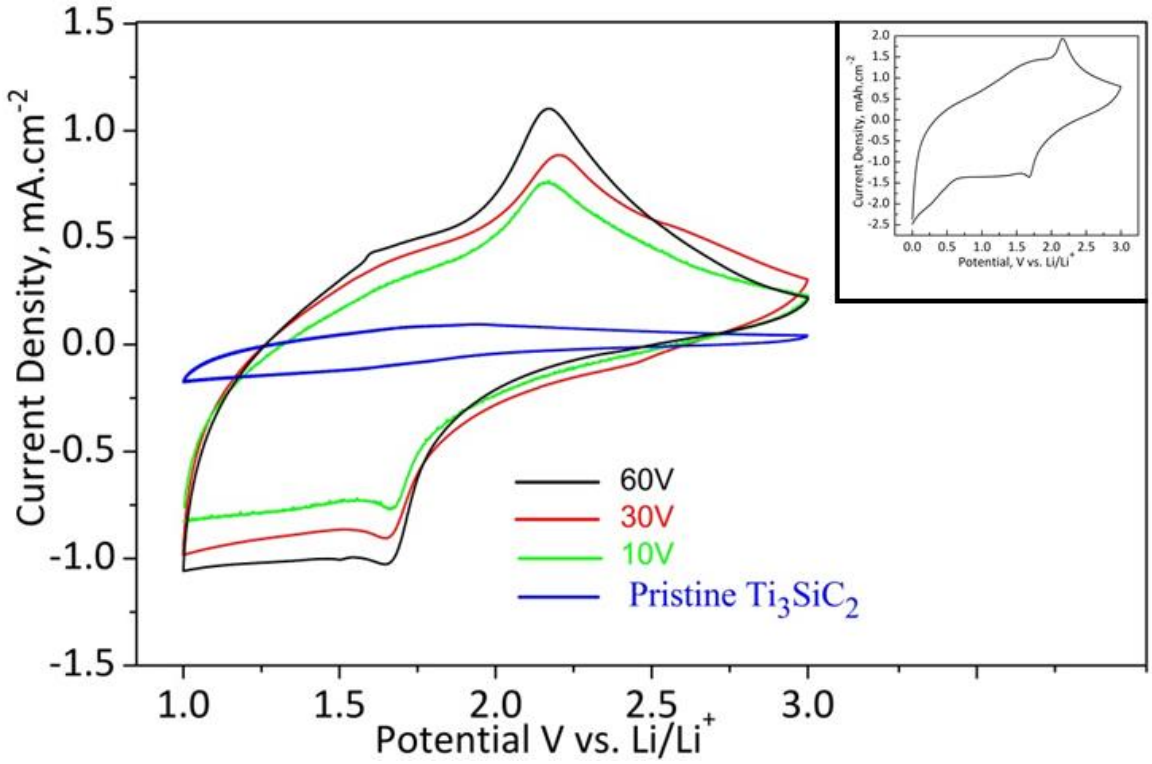

Fig. 4.2.10 Cyclic voltammograms (5th cycle) of pristine material and Ti_3SiC_2 anodized at 10, 30, and 60 V obtained at a sweep rate of 1 mV s^{-1} between 1 and 3 V vs Li/Li^+. Inset shows the CV curve for Ti_3SiC_2 anodized at 60 V recorded in potential window of 0.01 – 1.75 V vs Li/Li^+.

When the potential window was extended to 0.01 V vs Li/Li^+ (inset in Fig. 4.2.10), no other peaks were observed, suggesting that SiO_2 present is a minor component. The mole fraction of inserted lithium (x) into anatase is close to 0.5 and corresponds to a theoretical specific capacity of 168 mAh g^{-1}, which is in agreement with the capacity of TiO_2 anatase. As expected, the highest current density is reached for Ti_3SiC_2 anodized at 60 V for 3 h owing to its thicker oxide structure. In addition, all peaks are quite broad with the presence of a small peak below 1.6 V, suggesting that some of the Li^+ storage occurs at the surface. This capacitive effect, which is presumably responsible for peak broadening, increases with increasing porosity.

Fig. 4.2.11a shows the galvanostatic charge/discharge voltage profiles performed at 200 µA cm^{-2} for A-Ti_3SiC_2 (60 V). This profile can be divided into three regions ascribed to (i) the initial Li^+ insertion into anatase, characterized by a rapid drop in potential (from 3 to 1.75 V vs Li/Li^+) and the formation of Li_xTiO_2, with x up to 0.15, [41] (ii) a plateau at 1.75

V vs Li/Li^+ due to the presence of two phases,TiO_2 and Li_xTiO_2, [36] and last, (iii) a linear drop in potential from 1.75 to 1 V vs Li/Li^+, characteristics of pseudocapacitive behaviour [42]. The same potential regimes are seen in the charging curves. Note that the short presence of plateaus implies that the pseudocapacitive effect is significant, which is in agreement with the CV curves.

The cycle life performance was studied at applied current densities of 200, 300, and 500 µA cm^{-2}, respectively. The areal capacity (Ah cm^{-2}) vs cycle number is shown in Fig. 4.2.11b. The values of the discharge capacities were found to be 460, 350, and 380 µAh cm^{-2} for the 1^{st}, 2^{nd}, and 140^{th} cycles, respectively. These values are significantly higher than that reported for amorphous titania nanotubes [7] and very close to that for self-supported titania nanotubes fabricated by Wei and co-workers [11]. This can be attributed to the porosity combined with the presence of small amounts of free graphitic carbon improving the electronic conductivity [43]. The non-oxidized Ti_3SiC_2 probably also promotes faster kinetics due to its excellent electrical conductivity [17]. These results demonstrate that A-Ti_3SiC_2 is a potentially good negative electrode for microbattery applications. The irreversible capacity observed after the first cycle can

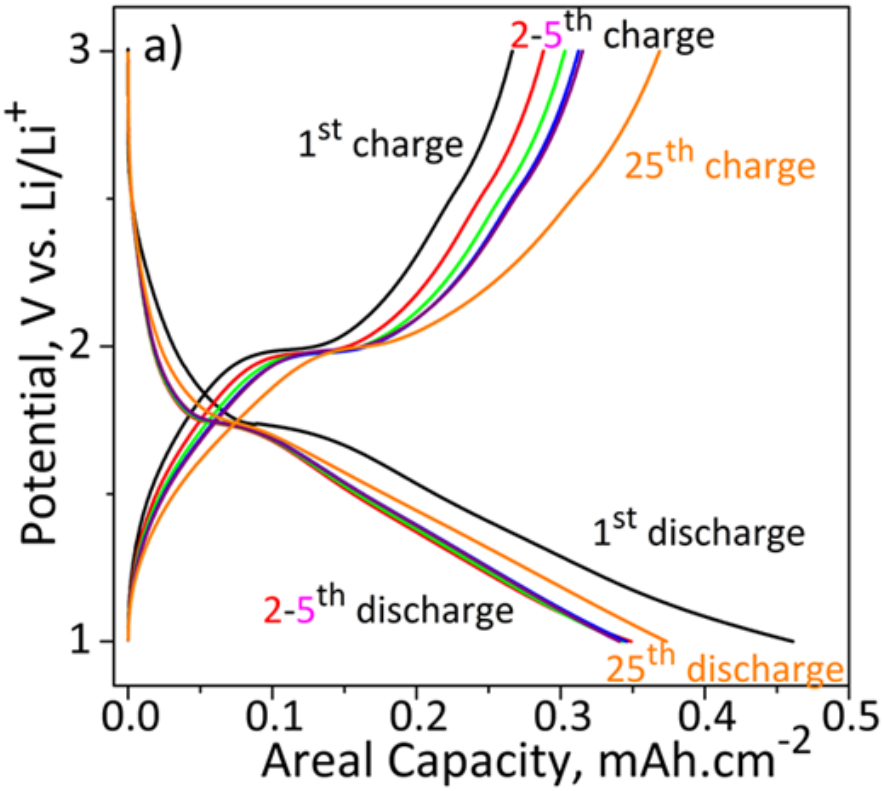

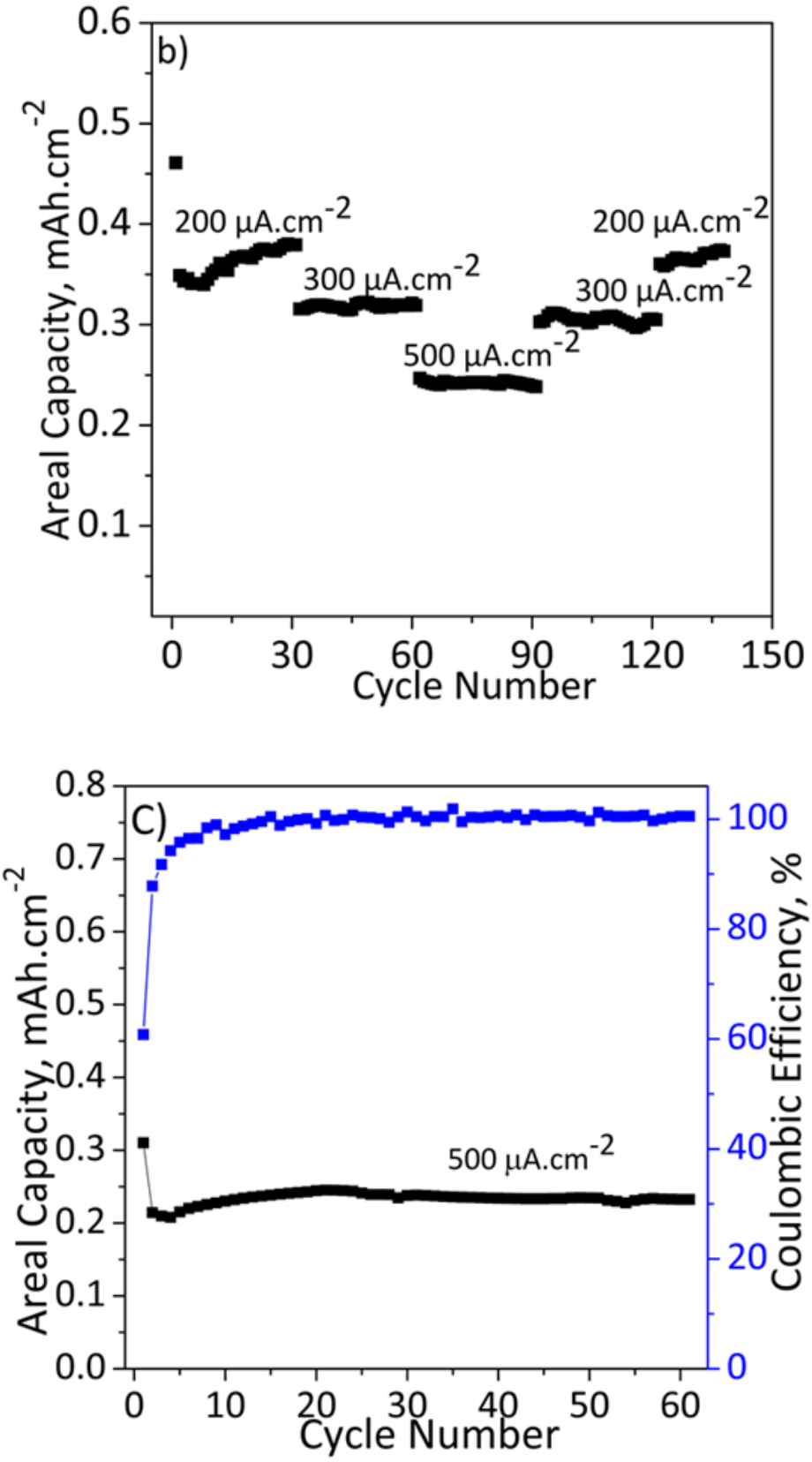

Fig. 4.2.11 (a) Typical galvanostatic charge–discharge curves at 200 µA cm^{-2}, (b) cycling performance, and (c) cycle stability for A-Ti_3SiC_2 (60 V).

be attributed to the reaction of Li^+ with traces of water molecules and Li^+ trapping in structural defects, as it has been observed for vertical arrays of titania nanotubes prepared by anodization [8] and the formation of SEI layer [44, 45].

It is remarkable that the discharge capacities increase with the number of cycles (Fig. 4.2.11 b and c). This effect can be ascribed to the formation of microcracks, which expose additional pore channels. The microcracks are probably a result of the phase changes during cycling. Interestingly, these microcracks do not seem to affect the integrity of the electrodes, at least up to 140 cycles. Except for the first two cycles, the capacity values are relatively stable up to 60 cycles for applied current density of 500 µAh cm^{-2} and a coulombic efficiency of > 95 % is obtained (Fig. 4.2.11c).

To verify the structural stability, and the morphological evolution, of A-Ti_3SiC_2, SEM and XRD analyses were carried out after 140 cycles (Fig. 4.2.12b) and compared to those before cycling (Fig. 4.2.12a). The presence of cracks is visible by comparing parts a and b of Fig. 4.2.12. However, according to the XRD pattern, no new peak appears after cycling, suggesting that the oxide structure is preserved (Fig. 4.2.12c). This approach is particularly promising for microbatteries, as a high areal capacity can be reached and the underlying MAX phase can act as the anode current collector, similar to the recently demonstrated carbide-derived carbon on TiC microsupercapacitors [46].

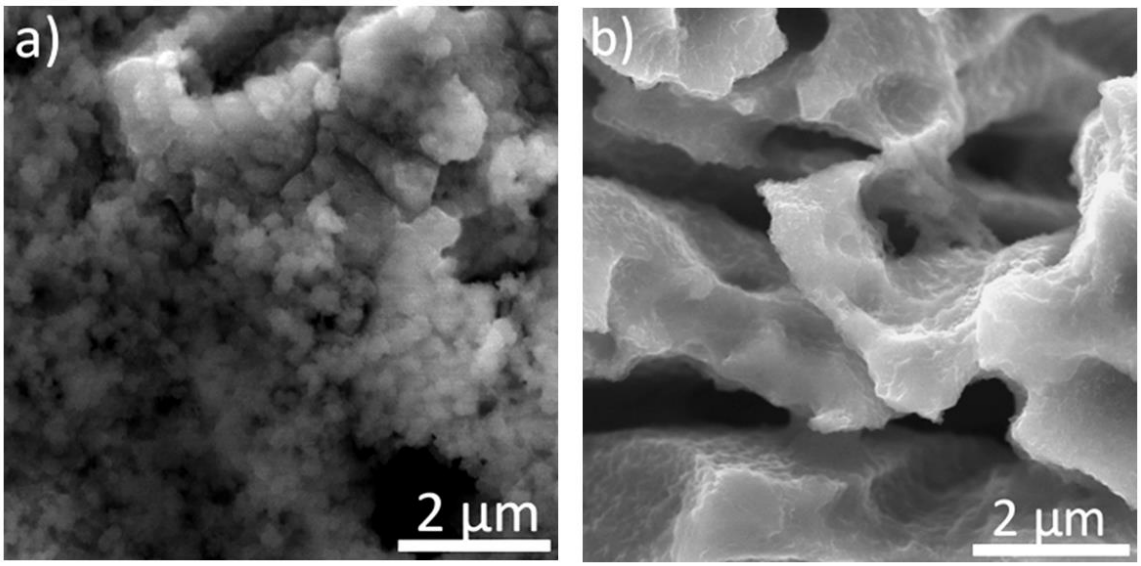

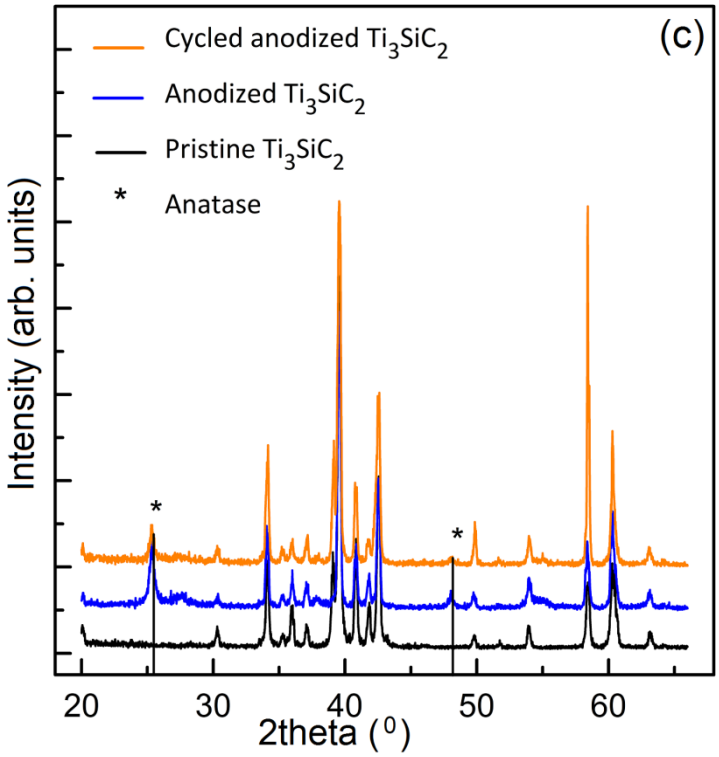

Fig. 4.2.12 SEM images of A-Ti_3SiC_2 (60 V) (a) before and (b) after 140 galvanostatic cycles in LIB. (c) XRD patterns for pristine and A-Ti_3SiC_2 (60 V) before and after galvanostatic cycling.

4.2.3.4 Tailoring the Morphological Properties of A-Ti_3SiC_2 for Better Power Density of Li-ion Microbatteries

The morphology of anodized Ti_3SiC_2 has a strong influence on the electrochemical performance of LIBs. Fig. 4.2.13a shows the first galvanostatic charge-discharge profiles. The first discharge areal capacity values (µAh cm^{-2} $µm^{-1}$) are very close, i.e. 24 µAh cm^{-2} $µm^{-1}$ and 22 µAh cm^{-2} $µm^{-1}$ for A-Ti_3SiC_2 (10 V) and A-Ti_3SiC_2 (60 V), respectively. Fig. 4.2.13b shows the electrochemical performance of A-Ti_3SiC_2 electrodes performed at the same kinetic for 30 cycles. The capacity loss after the first cycle can be induced by the irreversible reaction of Li^+ with trace water molecules, Li^+ trapping within the structural defects of titania, and the formation of SEI layer [44, 45]. The last discharge capacity values are 29 µAh cm^{-2} $µm^{-1}$ and 18 µAh cm^{-2} $µm^{-1}$ for A-Ti_3SiC_2 (10 V) and A-Ti_3SiC_2 (60 V), respectively. To compare the electrochemical performance of the two samples at a current density of 200 µA cm^{-2} after 30th cycle, a Ragone plot (Fig. 4.2.13c) has been

established using data given in Table 4.2.2. Compared to the mesoporous structure, the porous nanolayered morphology delivers a higher power density that can be attributed to the higher surface area enhancing the storage of charge through a pseudocapacitive mechanism.

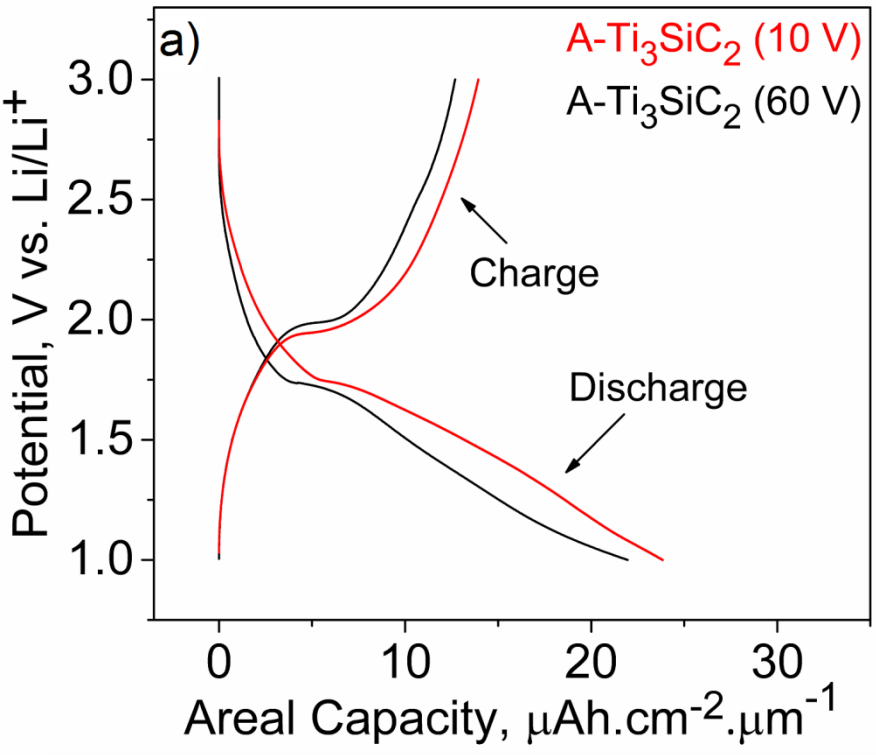

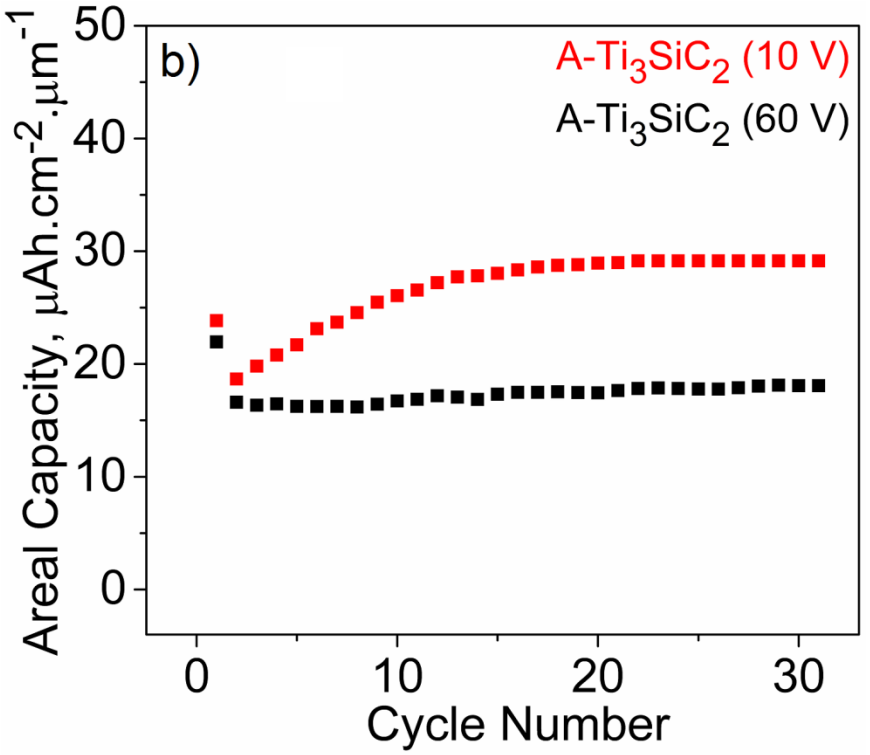

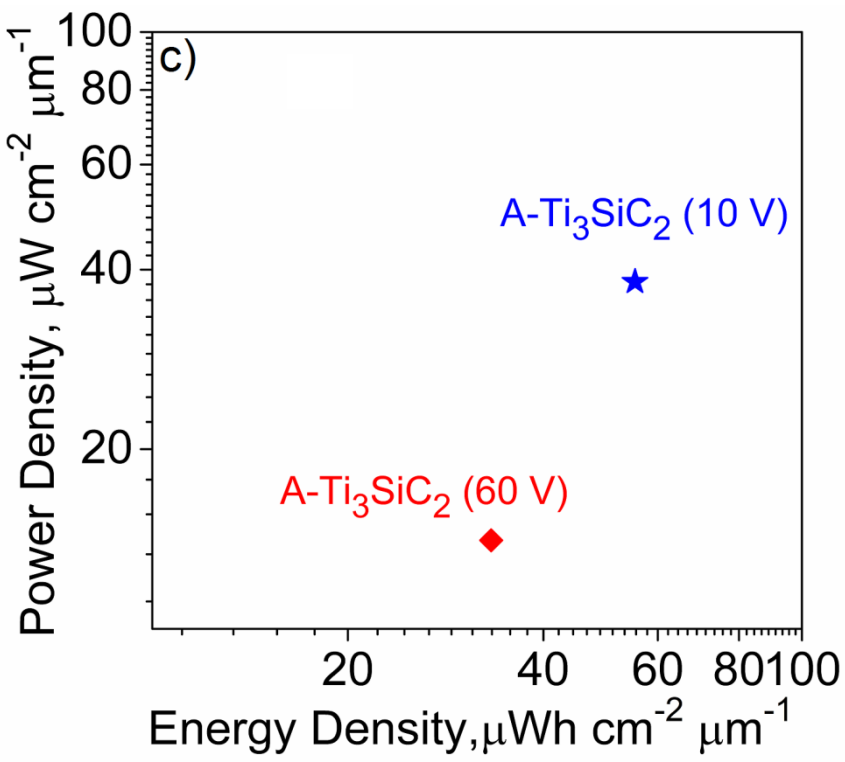

Fig. 4.2.13 (a) The first galvanostatic charge-discharge profiles, (b) cycling performance and (c) Ragone plot for Ti_3SiC_2 anodized at 10 V and 60 V at a current density of 200 μA cm^{-2} after 30 cycles. All the tests were carried out in the potential window of 1 – 3 V vs Li/Li^+.

Table 4.2.2 Data to Establish the Ragone Plot.

	A-Ti_3SiC_2 (10V)	A-Ti_3SiC_2 (60V)
30^{th} discharge capacity (μAh cm^{-2} $μm^{-1}$)	29	18
Operating voltage (V)	1.9	1.84
Discharge time (h)	1.45	2.36
Energy density = discharge capacity ∗ operating voltage (μWh cm^{-2} $μm^{-1}$)	55	33
Power density = energy density/discharge time (μW cm^{-2} $μm^{-1}$)	38	14

CV is a powerful technique for identifying the respective contributions of the surface (pseudocapacitive effect) and the bulk (diffusion of Li^+ into the TiO_2 lattice) [24, 47].

Generally, for mixed Li^+ storage processes the peak current (I_p) is given by Eq. (4.2.6) [47-49].

$$I_p = C_1 v + C_2 v^{1/2} \quad (4.2.6)$$

The first term ($C_1 v$) corresponds to the pseudocapacitive current I_c, which has a linear dependence on the scan rate *v*; the parameter C_1 is the product of the electrode surface area A and the capacitance per electrode surface area. The second term ($C_2 v^{1/2}$) corresponds to the diffusion current I_d, which has a square root dependence on the scan rate; the parameter C_2 is given by the product of $0.4958\,\mathrm{nFAc(D\alpha nF/RT)^{1/2}}$; where n is the number of electrons, F is the Faraday constant, c is the concentration of Li^+, D is the diffusion coefficient of Li^+, α is the transfer coefficient, R is the ideal gas constant, and T is the temperature [50]. Thus, the relative contribution of pseudocapacitive and bulk diffusion currents to the total storage current can be established by determining C_1 and C_2 at a specific scan rate.

Part a and b of Fig. 4.2.14 shows the CV curves for A-Ti_3SiC_2 (10 V) and A-Ti_3SiC_2 (60 V), respectively, recorded at various scan rates (0.05 – 1.3 mV s^{-1}). The total charge stored is strongly dependent on the scan rate. As shown in the CV curves, increasing the scan

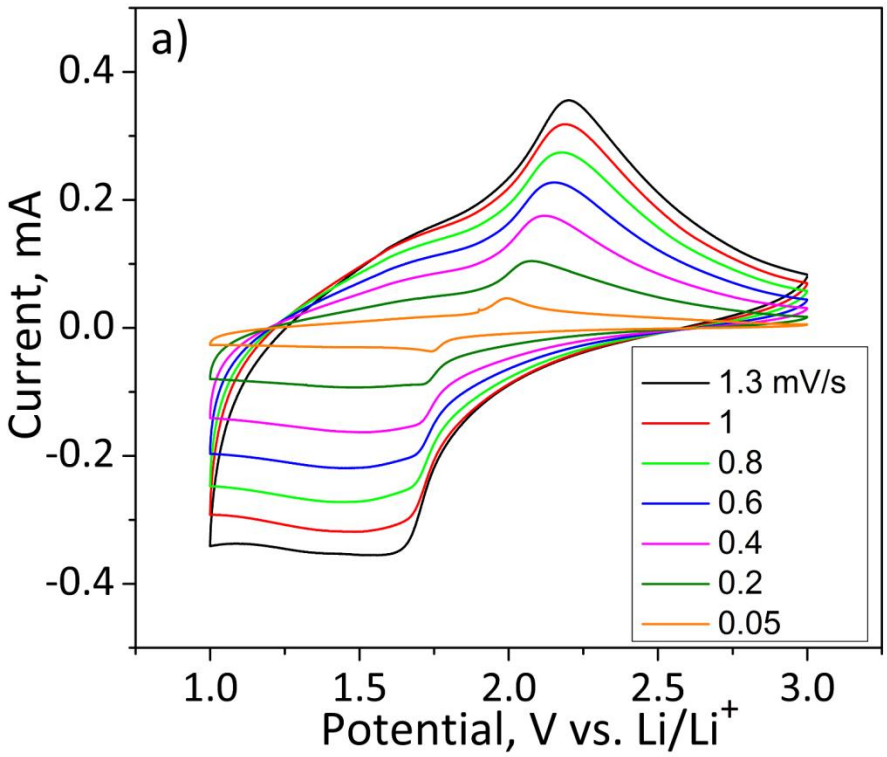

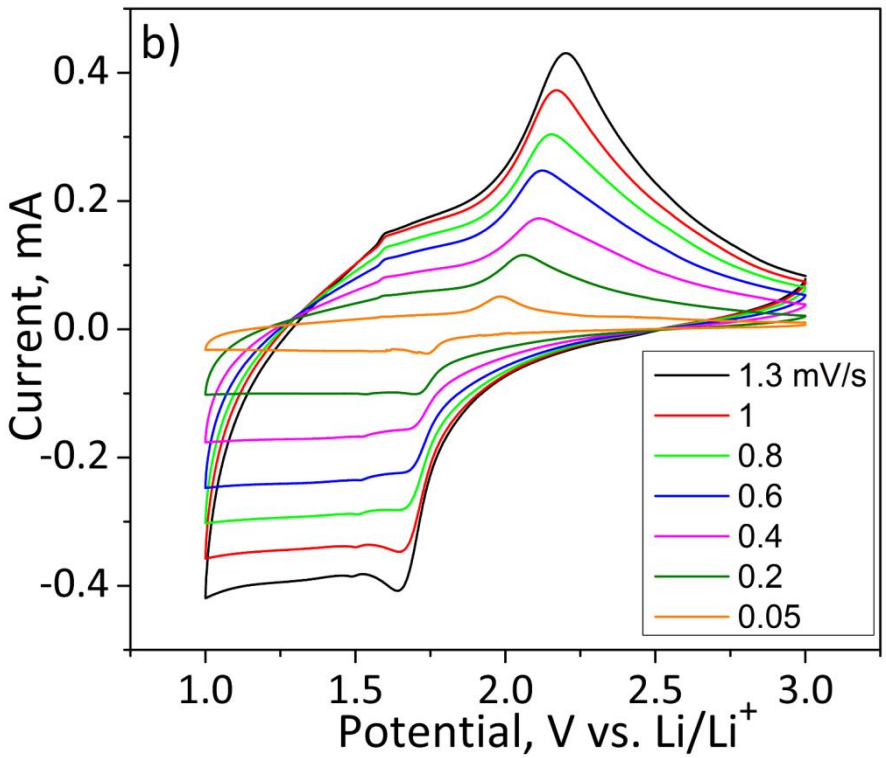

Fig. 4.2.14 (a) Cyclic voltammograms of Ti_3SiC_2 anodized at (a) 10 V and (b) 60 V recorded at various scan rates (0.05 – 1.3 mV s^{-1}).

rate results in the increase of peak current values as well as broadening and shifting of peak positions to lower and higher potentials. These electrochemical behaviour results from kinetic limitations to the diffusion of Li^+ within titania and the ohmic drop effects [11, 47,51].

Fig. 4.2.15a shows the peak discharge current as a function of scan rate for A-Ti_3SiC_2 (10 V). The best fit of the experimental data to an apparent power law ($I_p = a * v^b$) gives a dependence of $I_p \propto v^{0.845}$. There are two well-defined conditions: b = 0.5 and b = 1 corresponding to pure pseudocapacitive current (dashed black line) and pure diffusion current (dashed red line), respectively. An exponent value b = 0.845 is attributed to the contribution of both storage mechanisms. The best fit of the experimental data to Eq. (4.2.6) is represented by the red solid line giving the values for C_1= 0.159 ± 0.03 and C_2 = 0.00356 ± 0.00127.

Fig. 4.2.15b shows the calculated values of I_c and I_d as a function of scan rate for A-Ti_3SiC_2 (10 V). At low scan rates (< 0.4 mV s^{-1}), bulk diffusion of Li^+ into anatase is the

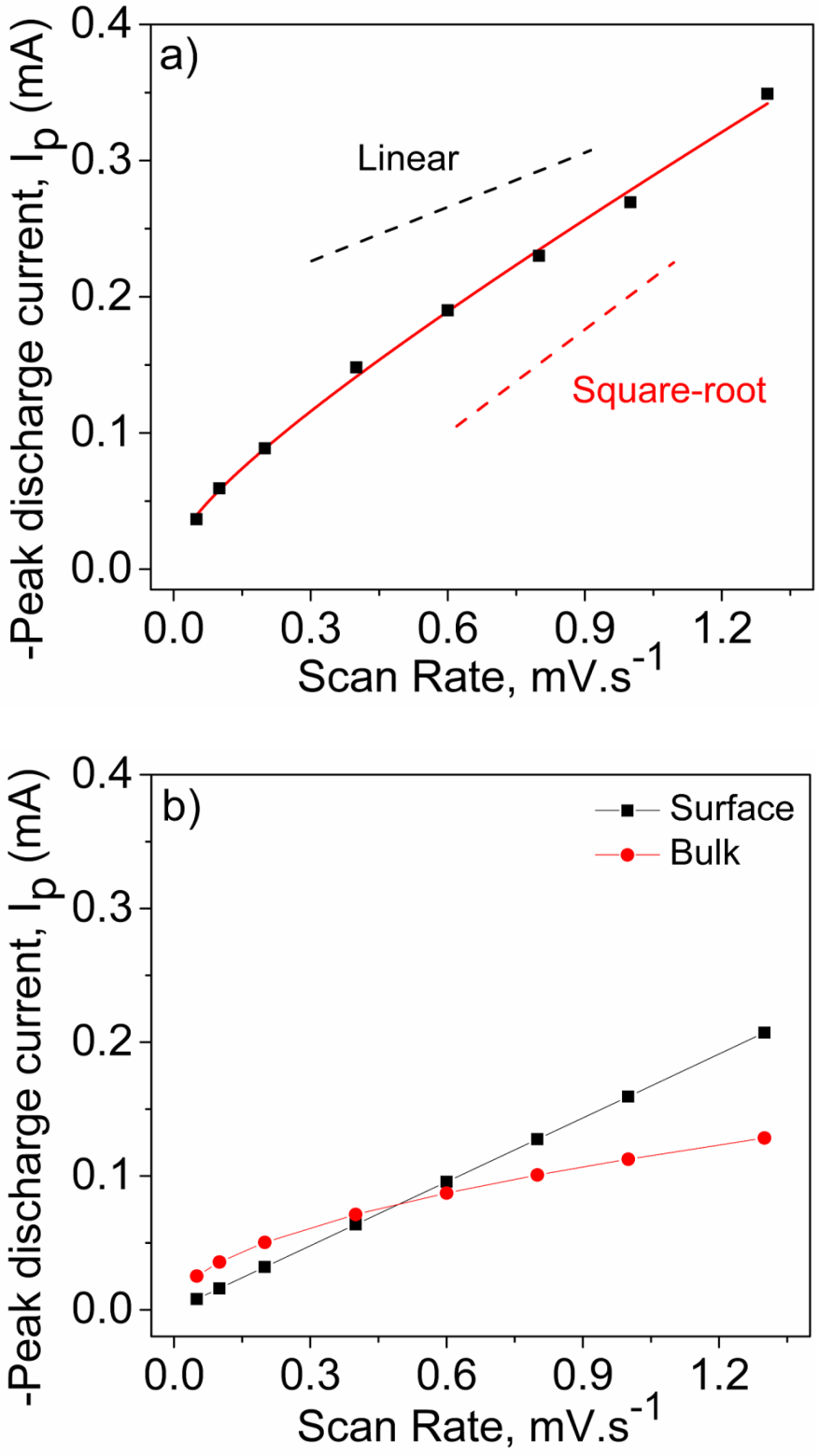

Fig. 4.2.15 (a) Peak discharge current vs scan rate: (■) experimental data and (—) fitting. (b) Calculated surface pseudocapacitive and bulk diffusion discharge currents for A-Ti_3SiC_2 (10 V).

predominant storage mechanism, e.g. the ratio I_d: I_c is 3:1 at 0.05 mV s^{-1}. However, the contribution of the pseudocapacitive current increases with increasing scan rate suggesting that storage of charges occurs predominately at the surface for faster kinetics. This might be the result of the extended layered morphology of A-Ti_3SiC_2 (10 V) as the contribution of pseudocapacitive storage increases with the surface area. The difference in charge storage mechanisms becomes more prominent at higher scan rates because of the fast charge/discharge processes induced by capacitive reactions, e.g. the ratio of I_d: I_c is 1:1.6 at 1.3 mV s^{-1}.

Fig. 4.2.16a shows the peak discharge current as a function of scan rate for A-Ti_3SiC_2 (60 V). The best fit of the experimental data to an apparent power law gives the dependence of the peak current to the scan rate $I_p \propto v^{0.6}$. The exponential value of 0.6 shows intercalation of Li^+ in to the titania lattice is the dominant storage mechanism. The best fit of the data to Eq. (4.2.6) yields C_1 = 0.0552 ± 0.017 and C_2 = 0.0107 ± 0.0007.

Fig. 4.2.16b shows that for A-Ti_3SiC_2 (60 V) bulk diffusion is the principal storage mechanism for all scan rates. The reasons for the enhanced power density can be explained by these results confirming that the layered structure formed at 10 V is able to store more charge at the surface than the mesoporous morphology obtained at 60 V.

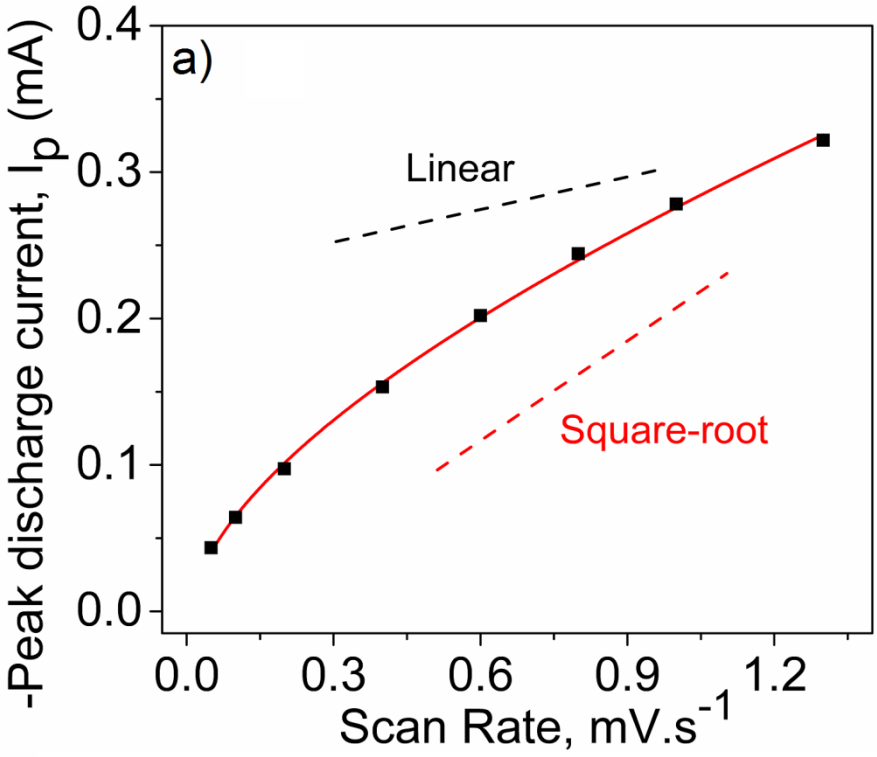

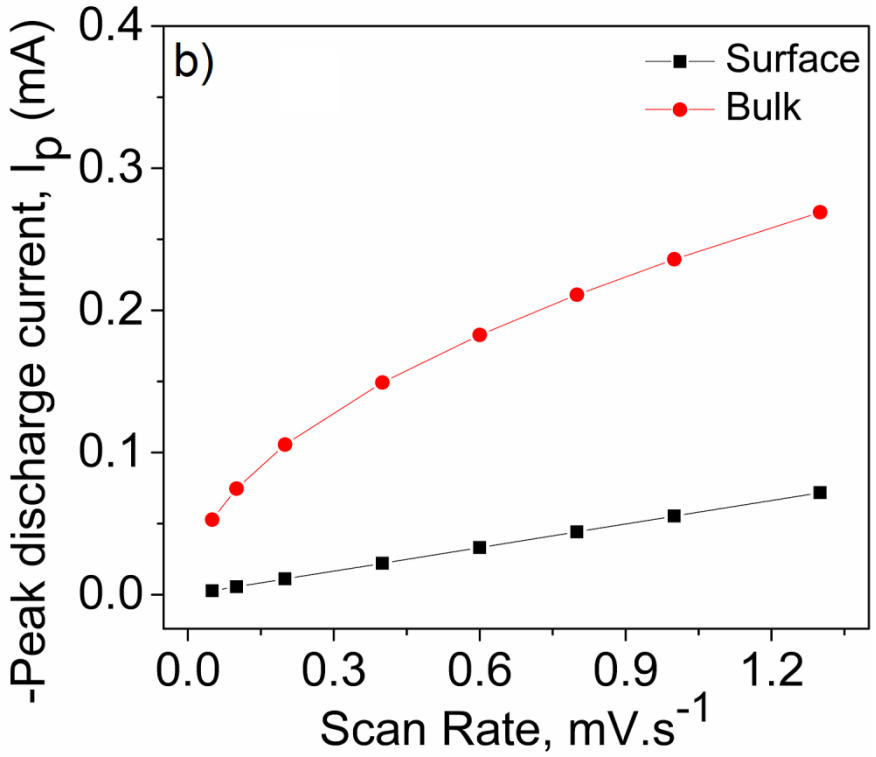

Fig. 4.2.16 (a) Peak discharge current vs scan rate: (■) experimental data and (—) fitting. (b) Calculated surface pseudocapacitive and bulk diffusion discharge currents for A-Ti_3SiC_2 (60 V).

4.2.4 Conclusion

In this work, we anodized the MAX phase, Ti_3SiC_2, in a HF containing electrolyte. After annealing the anodized Ti_3SiC_2 samples in air for 3 h, they were composed mostly of anatase, with small amounts of amorphous SiO_2 and carbon. The electrochemical tests demonstrated that anodized Ti_3SiC_2 can be used as a negative electrode material for Li-ion batteries. After 140 cycles performed at multiple applied current densities, an areal capacity of 380 µAh cm^{-2} (C-rate of 200 µA cm^{-2}) was achieved for A- Ti_3SiC_2 (60 V). This capacity is higher than that reported for amorphous titania. The high areal capacitance is attributed to the presence of disordered carbon carrying sp2-bonds and/or residual non anodized Ti_3SiC_2 regions that result in improved electrochemical reaction kinetics. The capacity loss after the first cycle is attributed to the irreversible reaction of Li^+ with trace water molecules, Li^+ trapping within the structural defects of titania, and the formation of SEI layer.

The electrochemical performance was enhanced by tailoring the morphological properties of A-Ti_3SiC_2. Compared to the mesoporous morphology obtained at 60 V, the power density delivered by the layered structure formed at 10 V is almost tripled. This effect can be explained by a higher porosity of the nanolayered structure promoting the charge storage at the surface. Cyclic voltammetry analyses have been performed to determine the relative contribution of pseudocapacitive and bulk diffusion storage. The anodized Ti_3SiC_2 electrode displayed both Li^+ storage mechanisms at the surface of the oxide film and within the bulk material. Clearly, the contribution of pseudocapacitive storage increases with scan rate and become the dominant mechanism at faster kinetics for nanolayered structure whereas for mesoporous morphology, bulk diffusion is the principal storage mechanism for the entire scan rates.

4.2.5 References

[1] D. Guyomard, J.-M. Tarascon, Rocking-chair or Lithium-ion Rechargeable Lithium Batteries, Adv. Mater., 6 (1994) 408-412.

[2] S. Megahed, B. Scrosati, Lithium-ion Rechargeable Batteries, J. Power Sources, 51 (1994) 79-104.

[3] M.V. Reddy, G.V. Subba Rao, B.V.R. Chowdari, Metal Oxides and Oxysalts as Anode Materials for Li Ion Batteries, Chem. Rev., 113 (2013) 5364-5457.

[4] B.L. Ellis, P. Knauth, T. Djenizian, Three-Dimensional Self-Supported Metal Oxides for Advanced Energy Storage, Adv. Mater., 26 (2014) 3368-3397.

[5] Q. Wang, Z. Wen, J. Li, Solvent-Controlled Synthesis and Electrochemical Lithium Storage of One-Dimensional TiO_2 Nanostructures, Inorg. Chem., 45 (2006) 6944-6949.

[6] Y. Gogotsi, What Nano Can Do for Energy Storage, ACS Nano, 8 (2014) 5369-5371.

[7] G.F. Ortiz, I. Hanzu, T. Djenizian, P. Lavela, J.L. Tirado, P. Knauth, Alternative Li-ion Battery Electrode based on Self-Organized Titania Nanotubes, Chem. Mater., 21 (2009) 63-67.

[8] T. Djenizian, I. Hanzu, P. Knauth, Nanostructured negative electrodes based on titania for Li-ion batteries microbatteries J. Mater. Chem., 21 (2011) 9925-9937.

[9] N.A. Kyeremetang, N. Plylahan, A.C.S.D. Santos, L.V. Traveira, L.F.P. Dick, T. Djenizian, Sulfidated TiO_2 nanotubes: A potential 3D cathode material for Li-ion microbatteries Chem. Commun. , 49 (2012) 4205-4207.

[10] N. Plylahan, S. Maria, T.N.T. Phan, M. Letiche, H. Martinez, C. Courrèges, P. Knauth, T. Djenizian, Enhanced Electrochemical Performance of Lithium-ion Batteries by Conformal Coating of Polymer Electrolyte, Nanoscale Res. Lett., 9 (2014) 1-8.

[11] W. Wei, G. Oltean, C.-W. Tai, K. Edstrom, F. Bjorefors, L. Nyholm, High Energy and Power Density TiO_2 Nanotube Electrodes for 3D Li-ion Microbatteries, J. Mater. Chem. A, 1 (2013) 8160-8169.

[12] N.A. Kyerematenq, Self-Organised TiO_2 Nanotubes for 2D or 3D Li-Ion Microbatteries, ChemElectroChem, 1 (2014) 1442-1466.

[13] A. Lamberti, N. Garino, A. Sacco, S. Bianco, A. Chiodoni, C. Gerbaldi, As-Grown Vertically Aligned Amorphous TiO_2 Nanotube Arrays as High-Rate Li-Based Micro-Battery Anodes with Improved Long-Term Performance, Electrochim. Acta, 151 (2015) 222-229.

[14] A. Lamberti, N. Garino, A. Sacco, S. Bianco, D. Manfredi, C. Gerbaldi, Vertically Aligned TiO_2 Nanotube Array for High Rate Li-Based Micro-Battery Anodes with Improved Durability, Electrochim. Acta, 102 (2013) 233-239.

[15] M.C. López, G.F. Ortiz, J.R. González, R. Alcántara, J.L. Tirado, Improving the Performance of Titania Nanotube Battery Materials by Surface Modification with Lithium Phosphate, ACS Appl. Mater. Interfaces, 6 (2014) 5669-5678.

[16] M.W. Barsoum, MAX Phases: Properties of Machinable Ternary Carbides and Nitrides, John Wiley & Sons2013.

[17] M.W. Barsoum, T. El-Raghy, Synthesis and Characterization of a Remarkable Ceramic: Ti3SiC2, J. Am. Ceram. Soc, 79 (1996) 1953-1956.

[18] M. Naguib, M. Kurtoglu, V. Presser, J. Lu, J. Niu, M. Heon, L. Hultman, Y. Gogotsi, M.W. Barsoum, Two-Dimensional Nanocrystals Produced by Exfoliation of Ti_3AlC_2, Adv. Mater., 23 (2011) 4248-4253.

[19] J. Come, M. Naguib, P. Rozier, M. Barsoum, Y. Gogotsi, P.-L. Taberna, M. Morcrette, P. Simon, A Non-Aqueous Asymmetric Cell with a Ti_2C-Based Two-Dimensional Negative Electrode, J. Electrochem. Soc., 159 (2012) A1368-A1373.

[20] M. Naguib, J. Come, B. Dyatkin, V. Presser, P.-L. Taberna, P. Simon, M.W. Barsoum, Y. Gogotsi, MXene: A Promising Transition Metal Carbide Anode for Lithium-ion Batteries, Electrochem. Commun., 16 (2012) 61-64.

[21] M. Naguib, J. Halim, J. Lu, K.M. Cook, L. Hultman, Y. Gogotsi, M.W. Barsoum, New Two-Dimensional Niobium and Vanadium Carbides as Promising Materials for Li-ion Batteries, J. Am. Chem. Soc., 135 (2013) 15966-15969.

[22] X. Liang, A. Garsuch, L.F. Nazar, Sulfur Cathodes Based on Conductive MXene Nanosheets for High-Performance Lithium–Sulfur Batteries, Angew. Chem. Int. Ed., 54 (2015) 3907-3911.

[23] M.R. Lukatskaya, O. Mashtalir, C.E. Ren, Y. Dall'Agnese, P. Rozier, P.L. Taberna, M. Naguib, P. Simon, M.W. Barsoum, Y. Gogotsi, Cation Intercalation and High Volumetric Capacitance of Two-Dimensional Titanium Carbide, Science, 341 (2013) 1502-1505.

[24] J. Wang, J. Polleux, J. Lim, B. Dunn, Pseudocapacitive contributions to electrochemical energy storage in TiO_2 (anatase) nanoparticles, J. Phys. Chem. C, 111 (2007) 14925-14931.

[25] X. Xie, S. Chen, W. Ding, Y. Nie, Z. Wei, An Extraordinarily Stable Catalyst: Pt NPs Supported on Two-Dimensional $Ti_3C_2X_2$ (X = OH, F) Nanosheets for Oxygen Reduction Reaction, Chem. Commun., 49 (2013) 10112-10114.

[26] M.R. Lukatskaya, J. Halim, B. Dyatkin, M. Naguib, Y.S. Buranova, M.W. Barsoum, Y. Gogotsi, Room-Temperature Carbide-Derived Carbon Synthesis by Electrochemical Etching of MAX Phases, Angew. Chem. Int. Ed., 53 (2014) 4877-4880.

[27] M.-Q. Zhao, M. Sedran, Z. Ling, M.R. Lukatskaya, O. Mashtalir, M. Ghidiu, B. Dyatkin, D.J. Tallman, T. Djenizian, M.W. Barsoum, Y. Gogotsi, Synthesis of Carbon/Sulfur Nanolaminates by Electrochemical Extraction of Titanium from Ti_2SC, Angew. Chem. Int. Ed., 54 (2015) 4892-4896.

[28] P. Roy, S. Berger, P. Schmuki, TiO_2 Nanotubes: Synthesis and Applications, Angew. Chem. Int. Ed., 50 (2011) 2904-2939.

[29] S. Berger, J. Kunze, P. Schmuki, D. LeClere, A.T. Valota, P. Skeldon, G.E. Thompson, A Lithographic Approach to Determine Volume Expansion Factors During Anodization: Using the Example of Initiation and Growth of TiO2-Nanotubes, Electrochim. Acta, 54 (2009) 5942-5948.

[30] L. Taveira, J. Macak, H. Tsuchiya, L. Dick, P. Schmuki, Initiation and Growth of Self-Organized TiO_2 Nanotubes Anodically Formed in NH4F⁄(NH4) 2SO4 Electrolytes, J. Electrochem. Soc., 152 (2005) B405-B410.

[31] M.W. Barsoum, T. El-Raghy, The MAX Phases: Unique New Carbide and Nitride Materials-Ternary Ceramics Turn out to Be Surprisingly Soft and Machinable, yet Also Heat-Tolerant, Strong and Lightweight, Am. Sci., 89 (2001) 334-343.

[32] G.Z. Cambaz, G.N. Yushin, Y. Gogotsi, V.G. Lutsenko, Anisotropic Etching of SiC Whiskers, Nano Lett., 6 (2006) 548-551.

[33] S. Verhaverbeke, I. Teerlinck, C. Vinckier, G. Stevens, R. Cartuyvels, M. Heyns, The Etching Mechanisms of SiO_2 in Hydrofluoric Acid, J. Electrochem. Soc., 141 (1994) 2852-2857.

[34] M. Naguib, Y. Gogotsi, Synthesis of Two-Dimensional Materials by Selective Extraction, Acc. Chem. Res., 48 (2014) 128-135.

[35] E. Kisi, J. Crossley, S. Myhra, M. Barsoum, Structure and Crystal Chemistry of Ti_3SiC_2, J. Phys. Chem. Solids, 59 (1998) 1437-1443.

[36] L. Kavan, M. Grätzel, J. Rathouský, A. Zukalb, Nanocrystalline TiO_2 (Anatase) Electrodes: Surface Morphology, Adsorption, and Electrochemical Properties, J. Electrochem. Soc., 143 (1996) 394-400.

[37] M.V. Koudriachova, N.M. Harrison, S.W. de Leeuw, Density-Functional Simulations of Lithium Intercalation in Rutile, Phys. Rev. B, 65 (2002) 235423-235435.

[38] J.S. Chen, X.W. Lou, SnO_2 and TiO_2 Nanosheets for Lithium-ion Batteries, Mater. Today, 15 (2012) 246-254.

[39] X.-Y. Yu, H.B. Wu, L. Yu, F.-X. Ma, X.W. Lou, Rutile TiO_2 Submicroboxes with Superior Lithium Storage Properties, Angew. Chem., Int. Ed., 54 (2015) 4001-4004.

[40] G. Zhang, H.B. Wu, T. Song, U. Paik, X.W. Lou, TiO_2 Hollow Spheres Composed of Highly Crystalline Nanocrystals Exhibit Superior Lithium Storage Properties, Angew. Chem., Int. Ed., 53 (2014) 12590-12593.

[41] G. Sudant, E. Baudrin, D. Larcher, J.-M. Tarascon, Electrochemical Lithium Reactivity with Nanotextured Anatase-Type TiO_2, J. Mater. Chem., 15 (2005) 1263-1269.

[42] M. Wagemaker, W.J.H. Borghols, F.M. Mulder, Large Impact of Particle Size on Insertion Reactions. A Case for Anatase Li_xTiO_2, J. Am. Chem. Soc., 129 (2007) 4323-4327.

[43] H. Ghassemi, W. Harlow, O. Mashtalir, M. Beidaghi, M.R. Lukatskaya, Y. Gogotsi, M.L. Taheri, In situ Environmental Transmission Electron Microscopy Study of Oxidation of Two-Dimensional Ti_3C_2 and Formation of Carbon-Supported TiO_2, J. Mater. Chem. A, 2 (2014) 14339-14343.

[44] E. Ventosa, E. Madej, G. Zampardi, B. Mei, P. Weide, H. Antoni, F. La Mantia, M. Muhler, W. Schuhmann, Solid Electrolyte Interphase (SEI) at TiO2 Electrodes in Li-Ion Batteries: Defining Apparent and Effective SEI Based on Evidence from X-ray Photoemission Spectroscopy and Scanning Electrochemical Microscopy, ACS Appl. Mater. Interfaces, 9 (2017) 3123-3130.

[45] S. Brutti, V. Gentili, H. Menard, B. Scrosati, P.G. Bruce, TiO2-(B) Nanotubes as Anodes for Lithium Batteries: Origin and Mitigation of Irreversible Capacity, Adv. Ener. Mater., 2 (2012) 322-327.

[46] P. Huang, C. Lethien, S. Pinaud, K. Brousse, R. Laloo, V. Turq, M. Respaud, A. Demortière, B. Daffos, P.L. Taberna, B. Chaudret, Y. Gogotsi, P. Simon, On-Chip and Freestanding Elastic Carbon Films for Micro-Supercapacitors, Science, 351 (2016) 691-695.

[47] N. Plylahan, A. Demoulin, L. Chrystelle, P. Knauth, T. Djenizian, Mechanism study of Li^+ insertion into titania nanotubes, RSC Adv., 5 (2015) 28474-28477.

[48] H. Lindström, S. Södergren, A. Solbrand, H. Rensmo, J. Hjelm, A. Hagfeldt, S.-E. Lindquist, Li^+ ion insertion in TiO_2 (anatase). 2. Voltammetry on nanoporous films, J. Phys. Chem. B, 101 (1997) 7717-7722.

[49] K. Zhu, Q. Wang, J.-H. Kim, A.A. Pesaran, A.J. Frank, Pseudocapacitive lithium-ion storage in oriented anatase TiO_2 nanotube arrays, J. Phys. Chem. C 116 (2012) 11895-11899.

[50] A.J. Bard, L.R. Faulkner, J. Leddy, C.G. Zoski, Electrochemical Methods: Fundamentals and Applications, Wiley New York1980.

[51] J. Ye, A.C. Baumgaertel, Y.M. Wang, J. Biener, M.M. Biener, Structural optimization of 3D porous electrodes for high-rate performance lithium ion batteries, ACS nano, 9 (2014) 2194-2202.

4.3 Porous Silicon Nanotube Arrays as Anode Material for Li-ion Batteries

The work presented in this section was done in collaboration between Aix-Marseille University and Texas Christian University (J. L. Coffer group). The work was published in ACS Applied Materials and Interfaces. DOI: 10.1021/acsami.5b05705.

4.3.1 Introduction

Because of a low operating potential (~ 0.25 V vs Li/Li^+) and the highest theoretical capacity reported so far (4200 mAh g^{-1}), Si is a promising negative electrode material for LIBs [1-5]. Si reacts reversibly with Li^+ by alloying/dealloying mechanisms according to Eq. (4.3.1) [6].

$$Si + xLi^+ + xe^- \leftrightarrows Li_xSi \qquad for\ 0 \leq x \leq 4.4 \tag{4.3.1}$$

Unfortunately, the reaction is accompanied by large volume expansion (~ 400 %), which results in pulverization and voltage cutoff in the first few cycles because of the loss of electrical contact [7, 8]. To address this concern, one-dimensional nanomaterials such as nanowires, nanotubes, and nanoporous instead of bulk materials have been investigated. For example, the use of nanostructured materials like graphite and transitional metal oxides [9-11] have shown an improved electrochemical performance compared to their bulk counterpart. For Si-based anode materials, it has been reported that voids between nano-objects are beneficial in bearing the volume expansion during cycling, [12-16] which is otherwise responsible for the strong capacity fading and the poor electrochemical cycling obtained in the case of bulk Si [7, 17-19]. The particular case of silicon nanotubes (SiNTs) offer well-defined uniform morphologies with a demonstrated impact on reversible capacity and long cycle life. Prior efforts have focused on sealed SiNTs (with or without carbon layers) [14, 15] or rather large SiNTs (> 400 nm diameter) containing porous silica shells [20]. In contrast, Coffer et al. has recently developed methods for the fabrication of ultrathin (~ 10 nm) crystalline SiNTs with clearly defined porous sidewalls [21]. The morphology associated with this type of nanotube platform is in stark difference to the other nanotube morphologies examined

previously, and warrants investigation in terms of capacity retention and cycling performance.

In this section, the synthesis and electrochemical behavior of self-supported vertical porous SiNTs fabricated by using sacrificial ZnO nanowire array templates on stainless steel substrate are discussed. We show that these self-supported SiNTs exhibit electrochemical properties to be of value as a negative electrode for LIBs.

4.3.2 Experimental Section

Zinc Oxide Nanowire Array (ZnO NWA) fabrication. ZnO NWA templates were prepared on stainless steel (1.5 cm x 1.5 cm) seeded primarily in a mixture solution (1:1 v:v) 0.03 M $Zn(NO_3)_2$ and 0.03 M hexamethylenetetramine at 92 ^{0}C for 10 – 40 h. Polyethylenimine (100 µl, branched, low molecular weight, Aldrich) was added into 100 ml of ZnO growth solution to adjust the ratio of L/D of ZnO NWA when desired . A ZnO seed layer was formed by spin - coating a mixture of 0.01 M zinc acetate (in methanol) and 0.03 M NaOH (also in methanol) (4:1 V:V) onto stainless steel substrates (without heating and stirring), followed by an oxidative treatment in air at 250 ^{0}C for 20 min.

SiNTs Fabrication. A ZnO NWA templates was inserted into a quartz tube reactor and Si deposition on the ZnO NWA was achieved through the use of silane, SiH_4, (15 sccm, 0.5% in He) mixed with He carrier gas (150 sccm) that was passed through a furnace operating at 500 ^{0}C for 8 min. These Si-coated ZnO NWA samples were then placed in another quartz reactor and heated to 450 ^{0}C; NH_4Cl was loaded in an alumina boat located upstream and heated to 350 ^{0}C. The gaseous etchant was transported via He gas downstream (100 sccm) to the furnace for 1 h for removal of the ZnO NWA substrate.

The half-cells consisted of as-formed self-standing SiNTs on stainless steel (0.55 cm^2) that were used as the working electrode and the current collector, respectively. A 9 mm diameter Li foil was used as the counter electrode and a Whatman glass microfiber separator soaked with lithium hexafluorophosphate in ethylene carbonate and diethylene carbonate (1 M $LiPF_6$ in (EC:DEC) 1:1 w/w) was used as separator. The mass of the active material was ~ 30 µg.

The cyclic voltammograms was performed in potential window of 0.01 − 1.75 V vs Li/Li^+ at a scan rate of 0.1 mV s^{-1}. The galvanostatic tests of the assembled cells were done at multiple C-rates (for this work 1 C = 4.2 A g^{-1}). The gravimetric capacity values were calculated on the basis of the weight of the active material. For all electrochemical tests, additives and binders were not used.

4.3.3 Results and Discussion

Fig. 4.3.1 shows the fabrication of SiNTs using three-step template-directed method [21]. First, the formation of a sacrificial ZnO NWA template was carried out on stainless steel substrates (Fig. 4.3.1a). This involves initial deposition of a ZnO nano-crystal seed layer on stainless steel, followed by annealing at 300 °C. ZnO nanowire arrays were grown from these seed layers by a hydrothermal process at 95 ^{0}C using 0.02 M $Zn(NO_3)_2$ and 0.02 M hexamethylenetetramine as precursors. Under these conditions, the length of the ZnO nanowires are 5 – 10 µm with length to diameter ratios (L/D) of ~ 10 – 25, depending on the reactant concentrations in the ZnO growth solution. Fig. 4.3.1b shows the deposition of Si onto the ZnO nanowires using chemical vapor deposition (CVD) technique. Specifically, the ZnO NWA exposure to silane, SiH_4, (150 sccm, 0.5% in He) at 530 ^{0}C in a dilute He atmosphere leads to coating of the template with Si. The thickness of the Si coating shell is dependent on silane exposure time (6 – 10 min).

Fig. 4.3.1c shows packed arrays of SiNTs which were obtained by removal of the ZnO NWA templates in NH_4Cl vapor at 450 ^{0}C [21]. At temperature higher than 420 ^{0}C the NH_4Cl decompose to generate HCl and NH_3 gas phase which start attacking the ZnO NWA templates according to the following reactions [21, 22]:

$$ZnO + 2\,HCl \;\rightarrow\; ZnCl_2 + H_2O \qquad (4.3.2)$$

$$ZnCl_2 + NH_3 \;\rightarrow\; Zn(NH_2)Cl + HCl \qquad (4.3.4)$$

The obtained SiNTs has porous structure that range in size from 2 – 5 nm. The porous structure is caused by strain-influenced mechanism, whereby Ostwald type coalescence into islands of Si occurs, with concomitant formation of void spaces in the nanotube. To

form a crystalline phase, the amorphous SiNTs was further annealed at 600 ^{0}C under He atmosphere for 30 min (Fig. 4.3.1d).

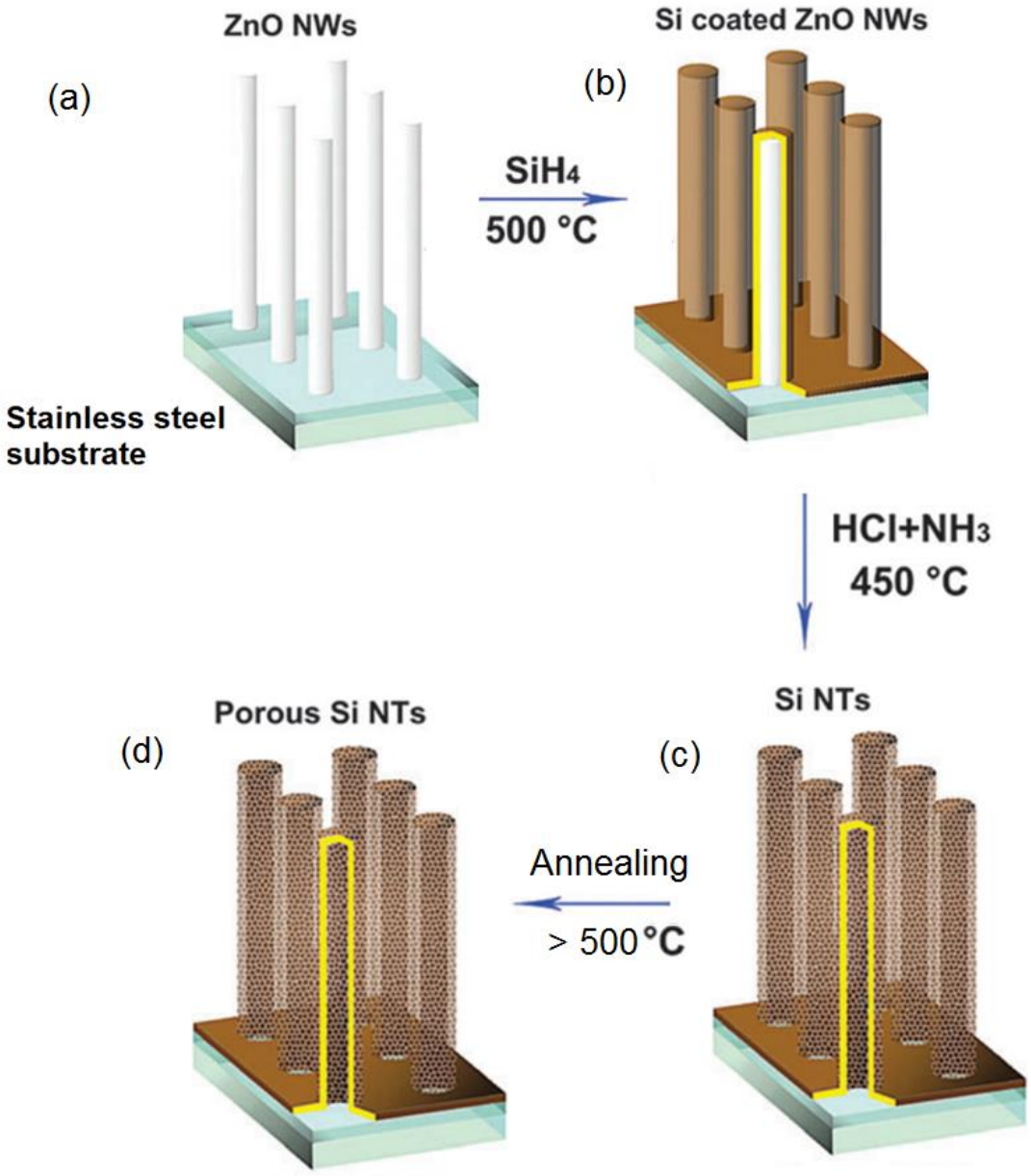

Fig. 4.3.1 A schematic representation of Si nanotube array (SiNTs) fabrication by three-step template directed method. (a) ZnO NWA templates on stainless steel substrate, (b) deposition of Si onto ZnO NWA by passing silane at 500 ^{0}C, (c) removal of the ZnO NWA templates by etching with HCl and NH_3 and (d) crystalline porous SiNTs were obtained by annealing at temperature of 600 ^{0}C.

The SiNTs were structurally characterized by a combination of field-emission SEM (Fig. 4.3.2) and TEM (Fig. 4.3.3); the latter technique included high-resolution imaging along with in situ elemental energy dispersive X-ray analysis (EDX). Fig. 4.3.2a and b shows low and high magnification SEM image of SiNTs, respectively, which reveals a dense packing of the nanotubes in a vertical fashion on the stainless steel substrate, as desired.

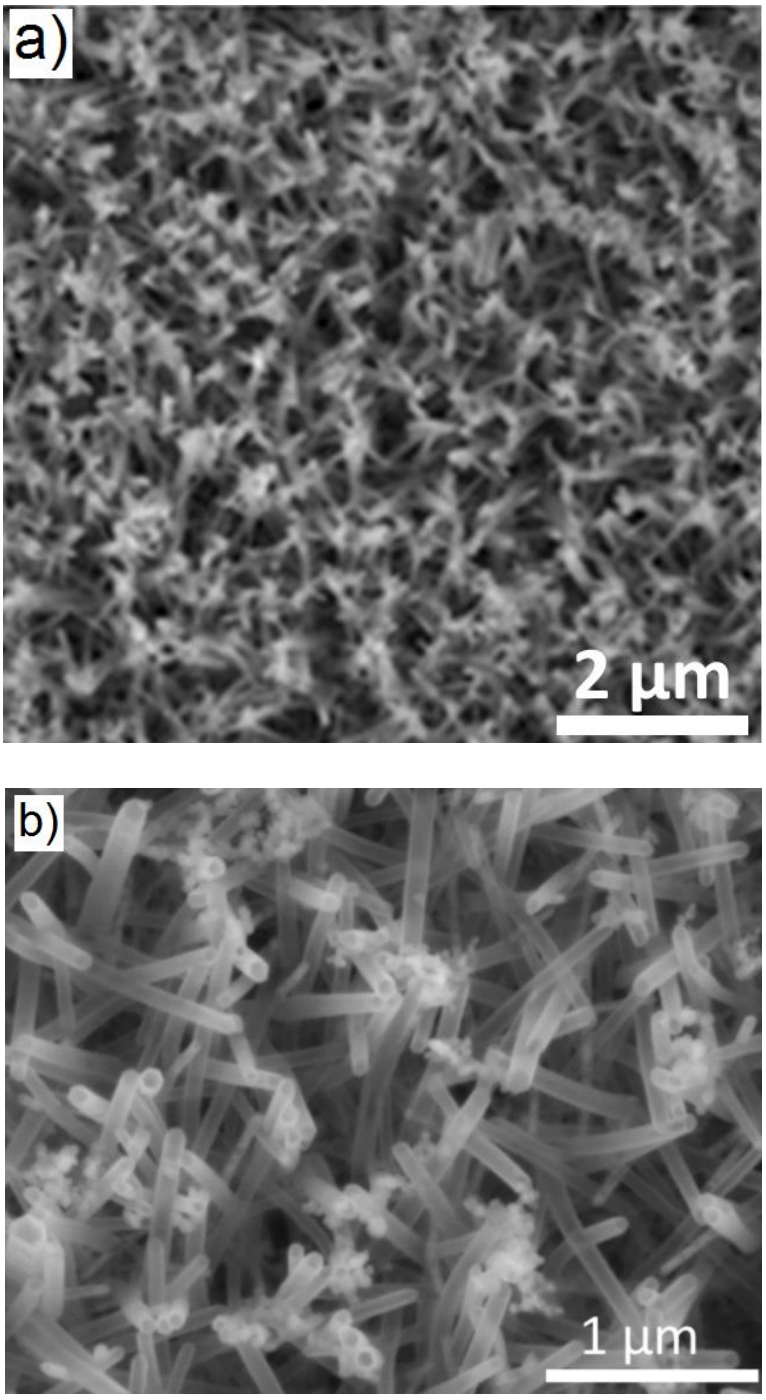

Fig. 4.3.2 (a) Low and (b) high magnification SEM images of SiNTs.

Complementary TEM analysis reveals a thin porous nature to the sidewalls of the nanotube, with a thickness on the order of 10 nm (Fig. 4.3.3a). Pores on the order of 2 – 5 nm can be observed along the length of a given tube. Statistical analysis of inner tube diameter shows a mean value of 57 nm (± 11 nm) with corresponding lengths up to 2 µm. The solid silicon regions of the nanotube are clearly crystalline in nature, as high-

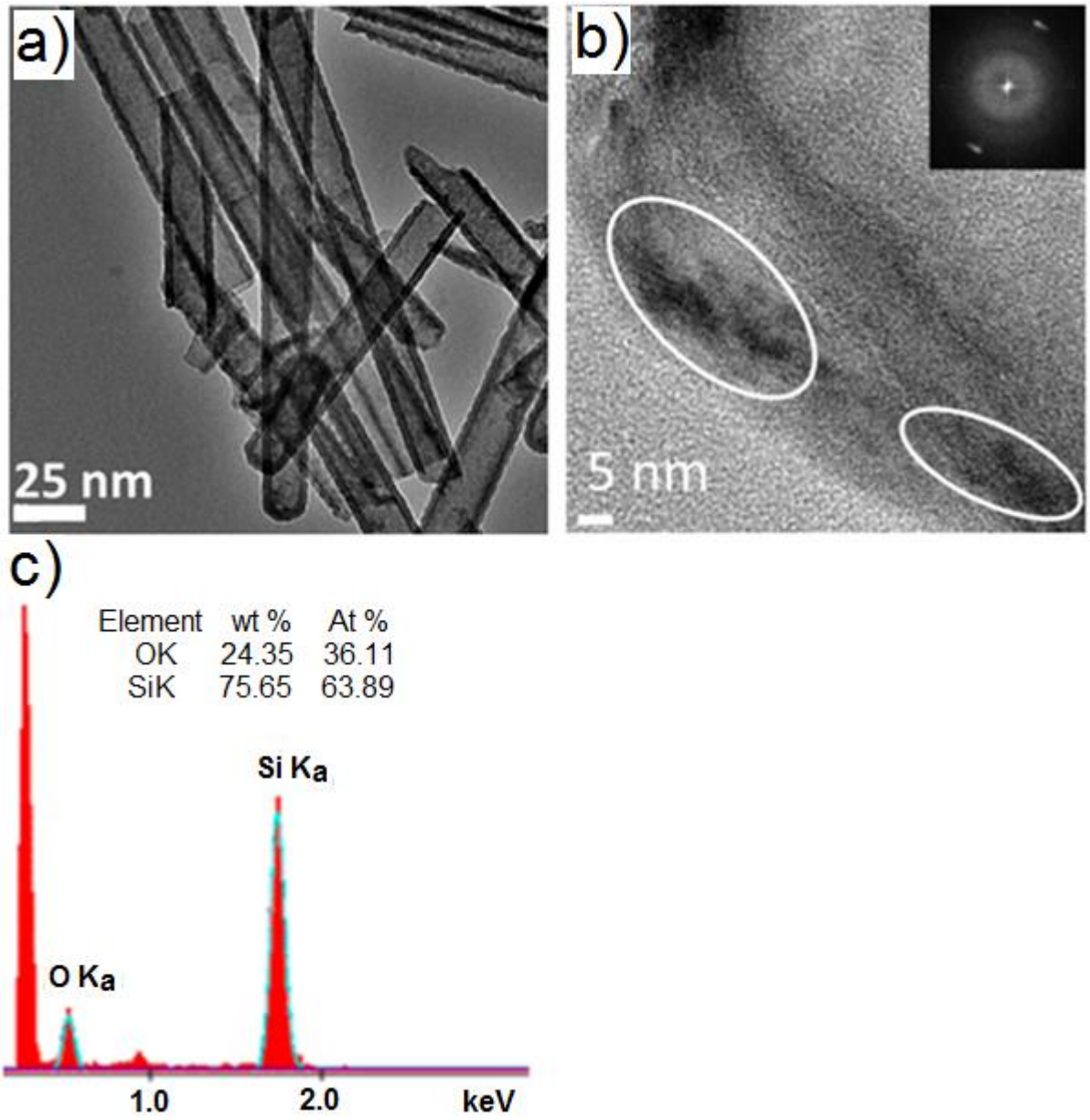

Fig. 4.3.3 (a) TEM and (b) HRTEM images of SiNTs. For the HRTEM the white circles represent crystalline domains of ⟨111⟩ orientation; inset: FFT indicating sample crystallinity. (c) EDX spectrum of SiNTs (from TEM analysis); small peak near 1.00 keV is associated with TEM sample grid.

resolution transmission electron microscope (HRTEM) imaging shows lattice spacing associated with the ⟨111⟩ index of cubic Si (Fig. 4.3.3b). In terms of composition, EDX analysis detects only the presence of Si and some oxygen from surface oxide species (Fig. 4.3.3c).

Fig. 4.3.4 shows the cyclic voltammogram (CV) recorded for first–fifth and 30th cycles. In agreement with previous studies, [4, 5] the electrochemical reactivity of the nanotubes are confirmed by the presence of four peaks during the first discharge. The irreversible peaks at 1.2 V vs Li/Li$^+$ are mainly due to the decomposition of the organic electrolyte leading to the formation of a solid electrolyte interface (SEI) at the surface of the electrode. The lithiation of the SiNTs begins around 0.4 V and further alloying is observed at 0.1 V vs Li/Li$^+$. The peaks at 0.38 and 0.5 V vs Li/Li$^+$ correspond to the dealloying of Si. The small broad peaks at potential of 0.7 and 1.0 V vs Li/Li$^+$ can be attributed to the reaction with iron oxide present in stainless steel substrate [23]. This material is known to demonstrate poor electrochemical behavior [24, 25].

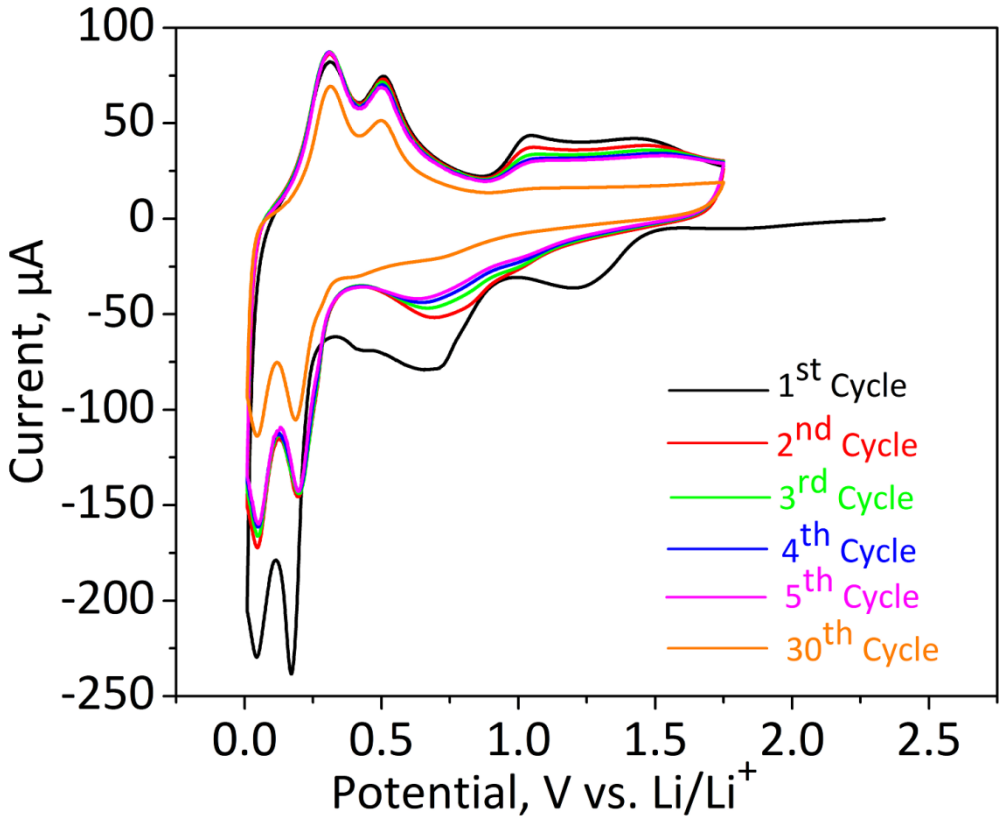

Fig. 4.3.4 Cyclic voltammogram recorded for the SiNTs in the potential window of 0.01 – 1.75 V vs Li/Li$^+$ at the scan rate of 0.1 mV s^{-1}.

Fig. 4.3.5a shows the galvanostatic charge–discharge curves performed at C/20 for the SiNTs. In agreement with the CV curves for the first discharge, there are four small plateaus at potential of 1.2 V, 0.7 V, 0.4 and 0.1 V vs Li/Li^+ corresponding to the organic electrolyte decomposition, the reduction of Fe^{3+} to Fe^0 and the formation of Li_xSi. The first discharge capacity of 4950 mAh g^{-1} is obtained for the SiNTs. The second discharge capacity of 3095 mAh g^{-1} with a coulombic efficiency of 63 % is attained. The capacity fading is attributed to the formation of the SEI layer and the irreversible reaction of Li^+ with iron oxide. Lithium ions react with iron oxide according to a conversion reaction mechanism to give metallic iron and Li_2O [24, 26]. The formation of Li_2O is irreversible and is also responsible for the large capacity loss during the first cycle. Although the capacity values decrease further, a stable value around 1670 mAh g^{-1} can be observed after 30 cycles with capacity retention of 54 %. These values are better than that reported for other selected Si nanostructured anodes, [27, 28] but not as high as large double walled SiNTs [20]. To place these results in the proper perspective, comparisons of the electrochemical performance of these SiNTs with previously reported literature results are shown in Table 4.3.1.

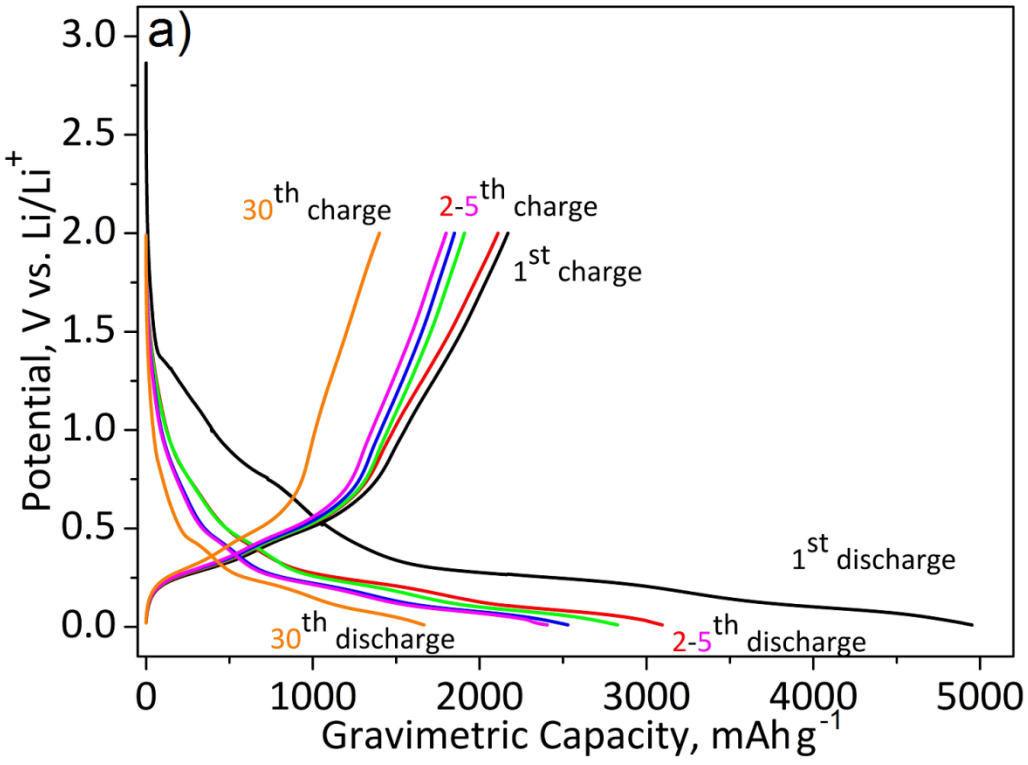

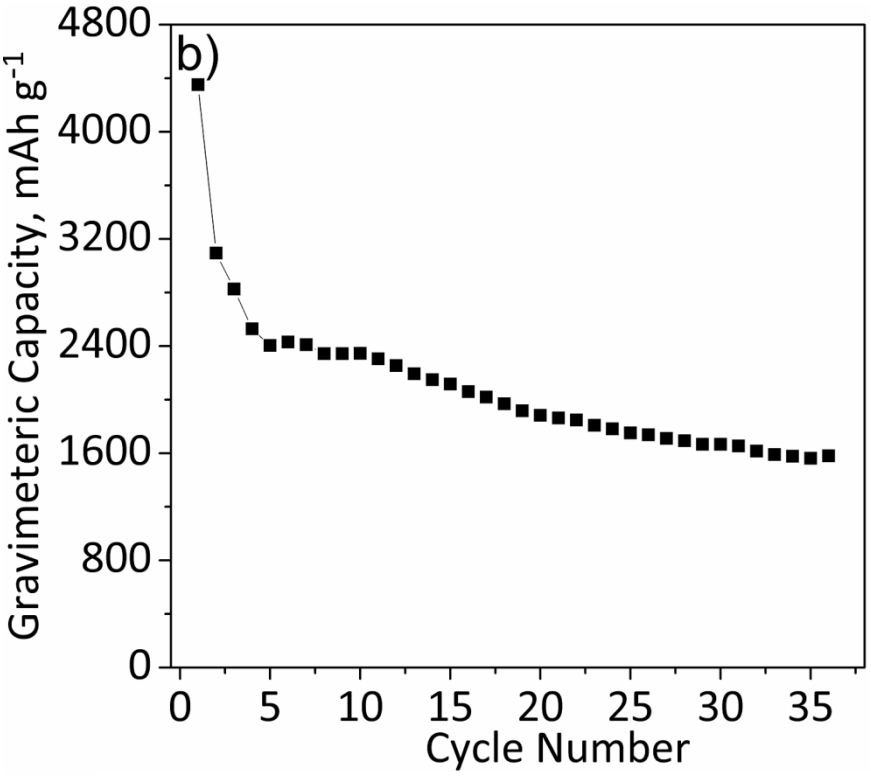

Fig. 4.3.5 (a) Galvanostatic discharge–charge profile and (b) capacity retention of SiNTs at C/20.

Table 4.3.1 Comparison of the Electrochemical Performance of Various SiNTs

working electrode	first discharge capacity (mAh g^{-1}) at C-rate	first irreversible capacity loss (%)	discharge capacity after (n) cycle (mAh g^{-1})	capacity retention (%) after (n) cycles	Coulombic efficiency (%) after (n) cycles
self-supporting SiNTs	4950 (0.05C)	63	1670 (30)	99.26 (30)	84.6 (30)
SiNTs [28]	1924 (0.5C)	80	1158 (10)	NA	60 (10)
SiNRs [27]	3285 (0.05C)	48.3	1398 (20)	NA	98.6 (20)
SiOC–CNT [29]	841.8 (0.1C)	67.1	686.3 (40)	81.5 (40)	99.6 (40)
carbon coated SiNWs [30]	3344 (0.15C)	86	1326 (40)	NA	95 (40)
DW SiNTs [20]	1780 (0.2C)	99.9	1566 (6000)	> 99.9 (6000)	> 99.9 (6000)

To study the operational stability of the SiNTs, the cycling life performance has been studied at multiple C-rates (Fig. 4.3.6). At high current density (1C), a gravimetric capacity of 450 mAh g^{-1} is observed; when the C-rate is subsequently restored to a

lower value (C/10), the capacity values reach 800 mAh g^{-1} suggesting that the microstructural features are partially preserved beyond 180 cycles (Fig. 4.3.6a). These results confirm that the porous three-dimensional geometry of the nanostructured Si electrode is beneficial to bear the large volume expansion during alloying/dealloying reactions.

Fig. 4.3.6b shows the capacity retention and the coulombic efficiency. Apart from the first three cycles, capacity retention of more than 97 % has been observed, whereas the coulombic efficiency of more than 75 % has been obtained for the first few cycles. It should be noted that during cycling, the coulombic efficiency increases slightly to reach 85 % at the 30th cycle, but still remains lower than those obtained for double-walled SiNTs [20], carbon-coated SiNTs [30], and pre-lithiated SiNWs [31].

The relatively high specific capacity value after 30 cycles and the excellent capacity retention of the SiNTs can be attributed to the high surface area of the porous nanotubular morphology. The high surface to volume ratio offers more active sites for lithium storage owing to the larger electrode/electrolyte interface and promote the

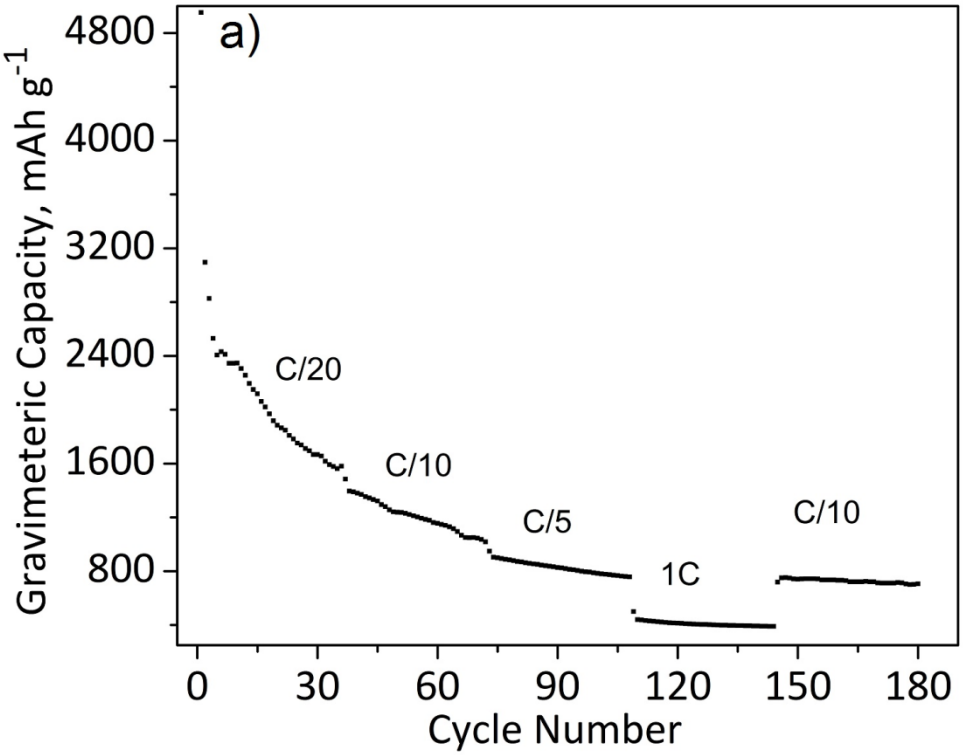

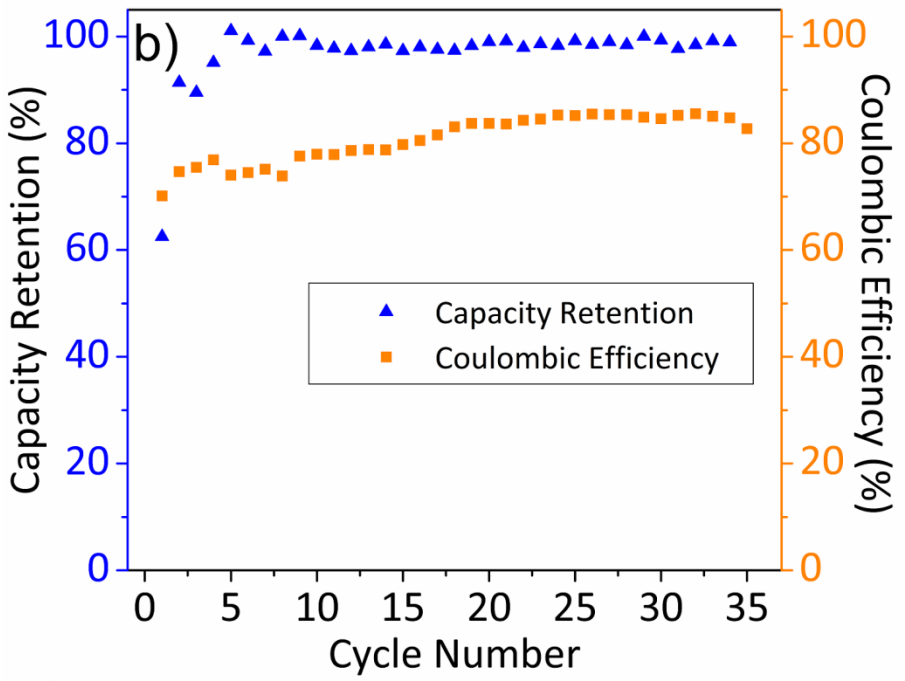

Fig. 4.3.6 (a) Cycling performance of SiNTs at multiple C-rates, and (b) coulombic efficiency and capacity retention vs cycle number of SiNTs at C/20.

storage of charges at the surface of the electrode according to a pseudocapacitive effect. This mechanism storage of charges can be verified by the presence of small plateaus and slopes in the charge/discharge profile.

To explain the origin of the capacity fading and the relatively low coulombic efficiency, post-mortem SEM (Fig. 4.3.6 a and b) and EDS analysis were carried out (Fig. 4.3.6c). EDS

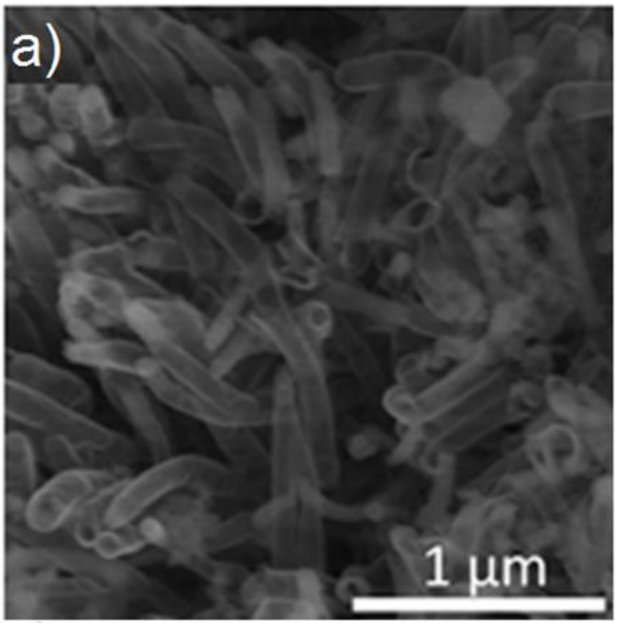

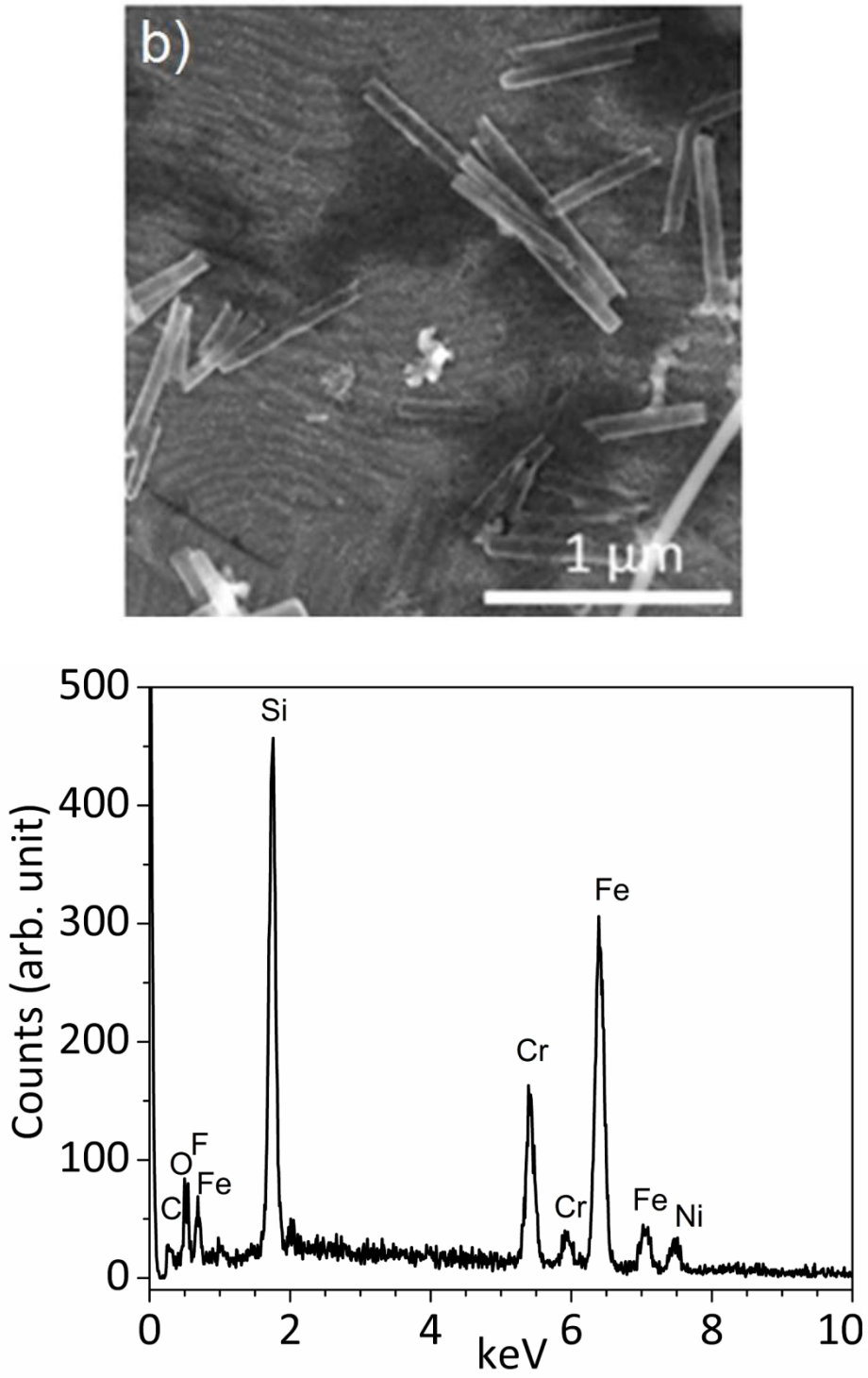

Fig. 4.3.7 (a, b) SEM images and (c) EDS spectra of SiNTs after 180 cycles.

analysis revealed the presence of F, C, and O confirming the formation of a SEI layer. This effect could be avoided in principle by using a solid electrolyte. In addition, it can be observed that SiNTs are partially broken and detached from the substrate after cycling. Hence, the relative poor adhesion of nanotubes to the substrate leads to the loss of the

electrical contact; in the future, this effect could be reduced by depositing a thin layer of Cr on stainless steel. Such a thin Cr layer could also be used to avoid the reaction of Li^+ with iron oxide and the subsequent formation of Li_2O that also hinders electron transfer.

4.2.4 Conclusion

A ZnO nanowire sacrificial template method, in conjunction with dilute Si reactant concentrations, was used to fabricate vertical arrays of Si nanotubes with thin porous sidewalls. The as-grown self-supported nanostructures have been used as a working electrode in LIB-half-cell tests. The electrochemical characterizations revealed good, stable electrochemical performance that can be attributed to the morphological properties of the material. In spite of the large volume expansion and the SEI formation associated with the use of Si, 54 % initial capacity is retained (1670 mAh g^{-1}) after 30 cycles and the capacity value of 800 mAh g^{-1} is attained after 180 cycles at C/10. The capacity fading and the low initial coulombic efficiency is attributed to the formation of SEI layer. In addition, the large volume change during alloying/dealloying result in the partial detachment of the nanotubes.

4.2.5 References

[1] M. Yoshio, T. Tsumura, N. Dimov, Electrochemical behaviors of silicon based anode material, J. Power Sources, 146 (2005) 10-14.

[2] X. Su, Q. Wu, J. Li, X. Xiao, A. Lott, W. Lu, B.W. Sheldon, J. Wu, Silicon-based nanomaterials for lithium-ion batteries: a review, Adv. Energy Mater., 4 (2014).

[3] B.A. Boukamp, G.C. Lesh, R.A. Huggins, All-Solid Lithium Electrodes with Mixed-Conductor Matrix, J. Electrochem. Soc, 128 (1981) 725-729.

[4] C.K. Chan, H. Peng, G. Liu, K. McIlwrath, X.F. Zhang, R.A. Huggins, Y. Cui, High-performance lithium battery anodes using silicon nanowires, Nat. Nanotechnol 3(2008) 31-35.

[5] B. Liang, Y. Liu, Y. Xu, Silicon-based materials as high capacity anodes for next generation lithium ion batteries, J. Power Sources, 267 (2014) 469-490.

[6] T.D. Bogart, A.M. Chockla, B.A. Korgel, High capacity lithium ion battery anodes of silicon and germanium, Curr Opin Chem Eng, 2 (2013) 286-293.

[7] U. Kasavajjula, C. Wang, A.J. Appleby, Nano-and bulk-silicon-based insertion anodes for lithium-ion secondary cells, Journal of Power Sources, 163 (2007) 1003-1039.

[8] L. Beaulieu, T. Hatchard, A. Bonakdarpour, M. Fleischauer, J. Dahn, Reaction of Li with alloy thin films studied by in situ AFM, Journal of The Electrochemical Society, 150 (2003) A1457-A1464.

[9] T. Djenizian, I. Hanzu, P. Knauth, Nanostructured negative electrodes based on titania for Li-ion batteries microbatteries J. Mater. Chem., 21 (2011) 9925-9937.

[10] B.L. Ellis, P. Knauth, T. Djenizian, Three-Dimensional Self-Supported Metal Oxides for Advanced Energy Storage, Adv. Mater., 26 (2014) 3368-3397.

[11] N.A. Kyeremetang, N. Plylahan, A.C.S.D. Santos, L.V. Traveira, L.F.P. Dick, T. Djenizian, Sulfidated TiO2 nanotubes: A potential 3D cathode material for Li-ion microbatteries Chem. Commun. , 49 (2012) 4205-4207.

[12] X.-y. Zhou, J.-j. Tang, J. Yang, J. Xie, L.-l. Ma, Silicon@carbon hollow core–shell heterostructures novel anode materials for lithium ion batteries, Electrochim. Acta, 87 (2013) 663-668.

[13] J. Jiang, Y. Li, J. Liu, X. Huang, Building one-dimensional oxide nanostructure arrays on conductive metal substrates for lithium-ion battery anodes, Nanoscale, 3 (2011) 45-58.

[14] M.-H. Park, M.G. Kim, J. Joo, K. Kim, J. Kim, S. Ahn, Y. Cui, J. Cho, Silicon Nanotube Battery Anodes, Nano Lett., 9 (2009) 3844-3847.

[15] T. Song, J. Xia, J.-H. Lee, D.H. Lee, M.-S. Kwon, J.-M. Choi, J. Wu, S.K. Doo, H. Chang, W.I. Park, Arrays of sealed silicon nanotubes as anodes for lithium ion batteries, Nano letters, 10 (2010) 1710-1716.

[16] D. Wang, Z. Yang, F. Li, X. Wang, D. Liu, P. Wang, D. He, Performance of Si–Ni nanorod as anode for Li-ion batteries, Mater. Lett., 65 (2011) 3227-3229.

[17] S.S. Zhang, A review on electrolyte additives for lithium-ion batteries, Journal of Power Sources, 162 (2006) 1379-1394.

[18] G. Simon, T. Goswami, Improving Anodes for Lithium Ion Batteries, Metall. Mater. Trans. A, 42 (2011) 231-238.

[19] D.M. Piper, T.A. Yersak, S.-H. Lee, Effect of compressive stress on electrochemical performance of silicon anodes, J. Electrochem. Soc., 160 (2013) A77-A81.

[20] H. Wu, G. Chan, J.W. Choi, I. Ryu, Y. Yao, M.T. McDowell, S.W. Lee, A. Jackson, Y. Yang, L. Hu, Y. Cui, Stable cycling of double-walled silicon nanotube battery anodes through solid-electrolyte interphase control, Nat Nano, 7 (2012) 310-315.

[21] X. Huang, R. Gonzalez-Rodriguez, R. Rich, Z. Gryczynski, J.L. Coffer, Fabrication and size dependent properties of porous silicon nanotube arrays, Chem. Commun., 49 (2013) 5760-5762.

[22] D. Cubicciotti, Effect of Carrier Gas on the Transpiration of Zinc Chloride, Inorganic Chemistry, 3 (1964) 1061-1062.

[23] P. Poizot, S. Laruelle, S. Grugeon, L. Dupont, J.M. Tarascon, Nano-sized transition-metal oxides as negative-electrode materials for lithium-ion batteries, Nature, 407 (2000) 496-499.

[24] D. Larcher, C. Masquelier, D. Bonnin, Y. Chabre, V. Masson, J.-B. Leriche, J.-M. Tarascon, Effect of Particle Size on Lithium Intercalation into α Fe_2O_3, J. Electrochem. Soc., 150 (2003) A133-A139.

[25] G.F. Ortiz, I. Hanzu, P. Lavela, J.L. Tirado, P. Knauth, T. Djenizian, A novel architectured negative electrode based on titania nanotube and iron oxide nanowire composites for Li-ion microbatteries, J. Mater.Chem., 20 (2010) 4041-4046.

[26] M.V. Reddy, G.V. Subba Rao, B.V.R. Chowdari, Metal Oxides and Oxysalts as Anode Materials for Li Ion Batteries, Chemical Reviews, 113 (2013) 5364-5457.

[27] Y. Zhou, X. Jiang, L. Chen, J. Yue, H. Xu, J. Yang, Y. Qian, Novel mesoporous silicon nanorod as an anode material for lithium ion batteries, Electrochim. Acta, 127 (2014) 252-258.

[28] Z. Wen, G. Lu, S. Mao, H. Kim, S. Cui, K. Yu, X. Huang, P.T. Hurley, O. Mao, J. Chen, Silicon nanotube anode for lithium-ion batteries, Electrochem. Commun., 29 (2013) 67-70.

[29] R. Bhandavat, G. Singh, Stable and Efficient Li-Ion Battery Anodes Prepared from Polymer-Derived Silicon Oxycarbide–Carbon Nanotube Shell/Core Composites, J. Phys. Chem. C, 117 (2013) 11899-11905.

[30] R. Huang, X. Fan, W. Shen, J. Zhu, Carbon-coated silicon nanowire array films for high-performance lithium-ion battery anodes, Appl. Phys. Lett., 95 (2009) 133119.

[31] N. Liu, L. Hu, M.T. McDowell, A. Jackson, Y. Cui, Prelithiated Silicon Nanowires as an Anode for Lithium Ion Batteries, ACS Nano, 5 (2011) 6487-6493.

4.4 Conclusion

The proposed electrode materials exhibit good electrochemical performance which makes them a promising candidates to replace carbon as a negative electrode for LIBs. However, their limitation due to capacity fading and the large irreversile capacity loss must be resolved before commercialization. The observed limitations are attributed to many factors, yet the formation and growth of SEI layer is the common factor for all the three proposed electrode materials. Because of the strong capacity fade and lack of many detailed studies on the Sn-based materials, specifically SnSb, we focus our study to investigate the formation and growth of SEI layer on SnSb electrode.

CHAPTER 5

STUDY OF THE SOLID ELECTROLYTE INTERPHASE (SEI) FORMATION ON SnSb ANODE

The objective of this chapter is to investigate the evolution of the electrical, compositional and morphological property of micron-sized SnSb electrode to understand the electrochemical behavior. Electron microscopy, chemical analysis techniques and electrochemical impedance spectroscopy have been combined to evidence the electrode modifications and particularly the formation of a SEI layer.

The work is accepted for publication on Electrochimica Acta.

5.1 Introduction

Chapter 4 (section 4.1) investigate micron-sized SnSb as a negative electrode for LIBs. The electrochemical characterization revealed high-specific capacity (ca. 833 mAh g^{-1}) and a good cycling stability up to 20 cycles. However, the capacity faded very quickly after the 25 cycles attributed to the disintegration of the electrode material due to the mechanical stress caused by the large volume change during lithium alloying and dealloying mechanism and the decomposition of the electrolyte that results in the formation of a SEI layer. Furthermore, the cracking of the electrode surface create new surfaces, which leads to the electrolyte decomposition promoting the SEI growth. The loss of electrical contact and active material combined with formation of passive layer is responsible for the overall poor electrochemical performance. Moreover, the formation of the SEI thin-film consumes irreversibly Li^+ and electrolyte leading to large irreversible capacity loss and low coulombic efficiency [1-4]. The SEI characteristics such as degradability, film thickness, and Li^+ conductivity dictate the kinetics of the electrochemical reactions and hence the batteries performance [5, 6]. Some of the strategies that have been proposed to solve this problem include the modification of the electrode by the use of composites, oxides, and alloys instead of pristine materials [7, 8]. The chemical modification of the electrolyte has been also proposed by adding additives like vinyl carbonate (VC) and fluroethylene carbonate (FEC) [9, 11].

Previous works have investigated the SEI formation on carbon-based anodes, while there are fewer studies on intermetallic compounds [6, 12-14]. In this chapter, evolution of the electrical and morphological properties of micron-sized SnSb has been investigated to understand the electrochemical behavior as an anode for LIBs. Particularly, electrode modifications such as the SEI formation are evidenced by electrochemical impedance spectroscopy (EIS), chemical analysis techniques (Fourier transform Infrared Spectroscopy (FTIR) and nuclear magnetic resonance spectroscopy (NMR)) and electron microscopy techniques including scanning electron microscopy (SEM) and transmission electron microscopy (TEM). Furthermore, the relation between the capacity fading and the electrode evolutions with the cell voltage is studied up to 50 cycles.

5.2 Experimental Section

SnSb anodes were prepared using slurry cast method by mixing a SnSb powder, binding agent polyvinylidene fluoride (PVDF), and conducting agent (Carbon black Sp) with mass ratio of 70:15:15 in vibrational ball milling for 25 min at 20 Hz. The slurry was tape casted on Cu current collector at room temperature for 24 h and then further dried at 110 ^{0}C for 12 h under vacuum.

Galvanostatic cycling with potential limitation (GCPL) and electrochemical impedance spectroscopy (EIS) were performed using standard three-electrode Swagelok cells assembled in a glove box filled with high purity argon. The half-cells were consisted of SnSb as the working electrode, Li foil served as the reference and the counter electrode. The two electrodes were separated by a Whatman glass microfiber soaked in the liquid organic electrolyte (1 M $LiPF_6$ in EC:PC:3DMC with 1% vol. VC and 5% vol. FEC). Prior to the impedance measurements, the cells were stored 24 h for stabilization. EIS measurements were performed at different potentials reached by galvanostatic experiments at C/20. The first discharge was performed from open circuit potential (OCP = 2.75 V) to 0.01 V vs. Li/Li^+ and the charge was carried out in the potential window 0.01 – 1.75 V vs. Li/Li^+. The EIS measurements performed during the discharge were recorded by applying an ac bias and amplitude of 7 mV over the frequency range of 200 KHz to 10 mHz at 2.75 V, 1 V, 0.78 V, 0.625 V, 0.5 V, 0.3 V, and 0.01 V vs. Li/Li^+ . The EIS measurements obtained during the charge were carried out under the same conditions at 0.01 V, 0.3 V, 0.5 V, 0.625 V, 0.78 V, 1 V, and 1.75 V vs. Li/Li^+.

Ex-situ SEM and TEM images of SnSb electrode were acquired during the first cycle at various potential stages: OCP; first discharge cutoff voltage of 0.68 V and 0.01 V; first charge cutoff voltage 0.75 V and 1.75 V vs. Li/Li^+. The morphological evolution of the SEI films with cycling was investigated using SEM and TEM images acquired after the 1st, 10th, 30th and 50th cycles.

5.3 Results and Discussion

5.3.1 Electrochemical Characterization

Fig. 5.1a shows the equivalent circuit used for analyzing the impedance spectra of SnSb/Li cell [15-18], where Re represents essentially the resistance of the electrolyte, Rsei and Csei are the resistance and capacitance of the SEI film, respectively. Rct and Cdl are the charge transfer resistance and double layer capacitance, respectively. Cint and W are the differential intercalation capacitance and the Warburg impedance describing the semi-infinite diffusion of Li^+ in the SnSb bulk electrode, respectively.

Fig. 5.1b shows the voltage variations of SnSb/Li cell vs. number of Li^+ (x) for the first cycle at C/20. The EIS spectra were obtained at different stages labeled D1 - D7 (discharge) and C1 – C6 (charge). As given in chapter, Li^+ reacts reversibly with SnSb by alloying/dealloying mechanism according to Eqs. (1 and 2) [19, 20].

$$3Li^+ + SnSb + 3e^- \rightleftharpoons Li_3Sb + Sn \quad (5.1)$$

$$xLi^+ + Sn + xe^- \rightleftharpoons Li_xSn \qquad (x \sim 4.4) \quad (5.2)$$

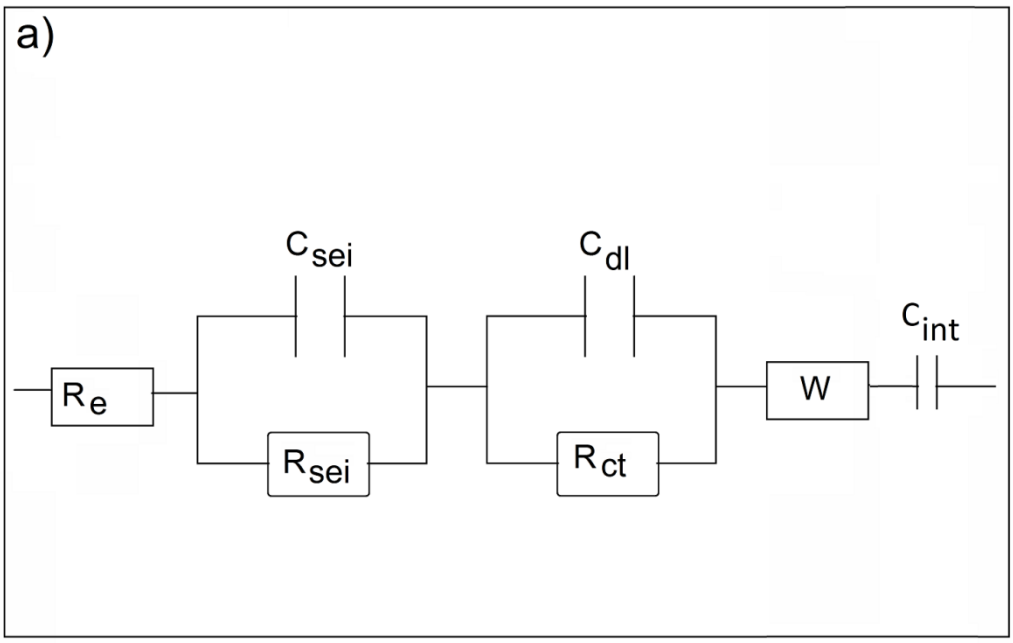

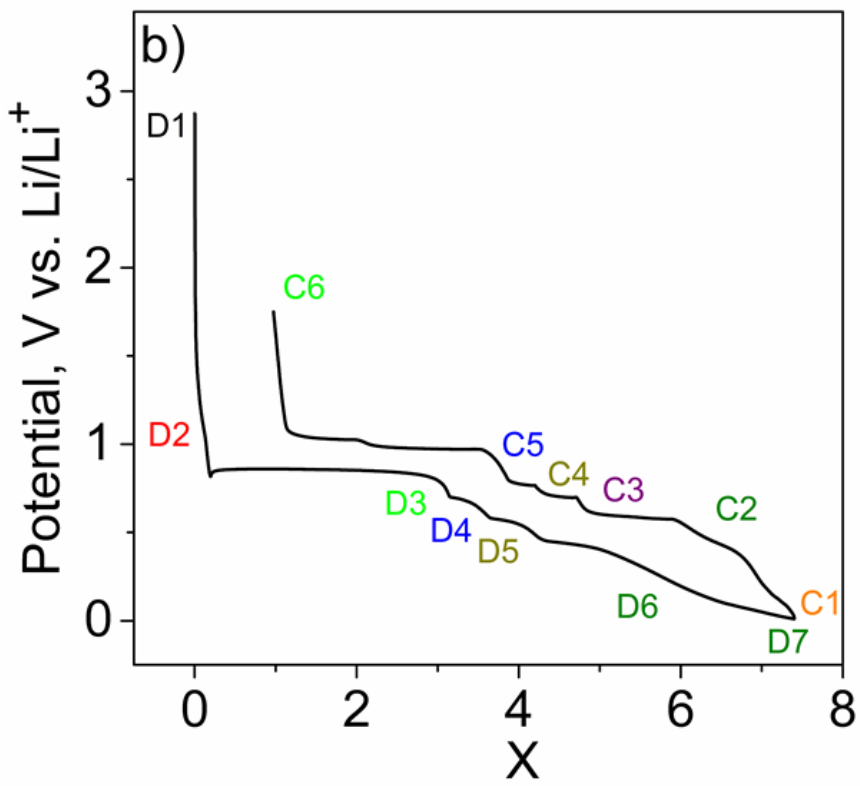

Fig. 5.1 (a) Equivalent circuit used for impedance analysis of SnSb/Li cell (b) galvanostatic profile of SnSb/Li cell vs. number of Li^+(x) at C/20 for the first cycle. The EIS spectra were measured at different stages labeled D1 - D7 (discharge) and C1 - C6 (charge).

In Fig. 5.2a, the impedance spectrum obtained at OCP = 2.75 V vs. Li/Li^+ shows a semi-circle at high frequency (HF) that can be attributed to the formation of the SEI layer as soon as SnSb is in contact with the organic liquid electrolyte [21]. At lower frequency (LF), the presence of a line at an angle close to 90^0 is typical of a capacitance behavior. The impedance spectra obtained for the first alloying/de-alloying reactions consist of two overlapped semi-circles at HF and medium frequency (MF) domain followed by a line at LF which is attributed to the diffusion of Li^+ in the bulk material. Finally, at very low frequencies, the -Zim vs. Zre plot becomes very steep, and in fact, reflects the intercalation capacitance ($C_{int} \approx -1/\omega Zim$, $\omega = 2\pi f \rightarrow 0$), Fig. 5.2 a and b.

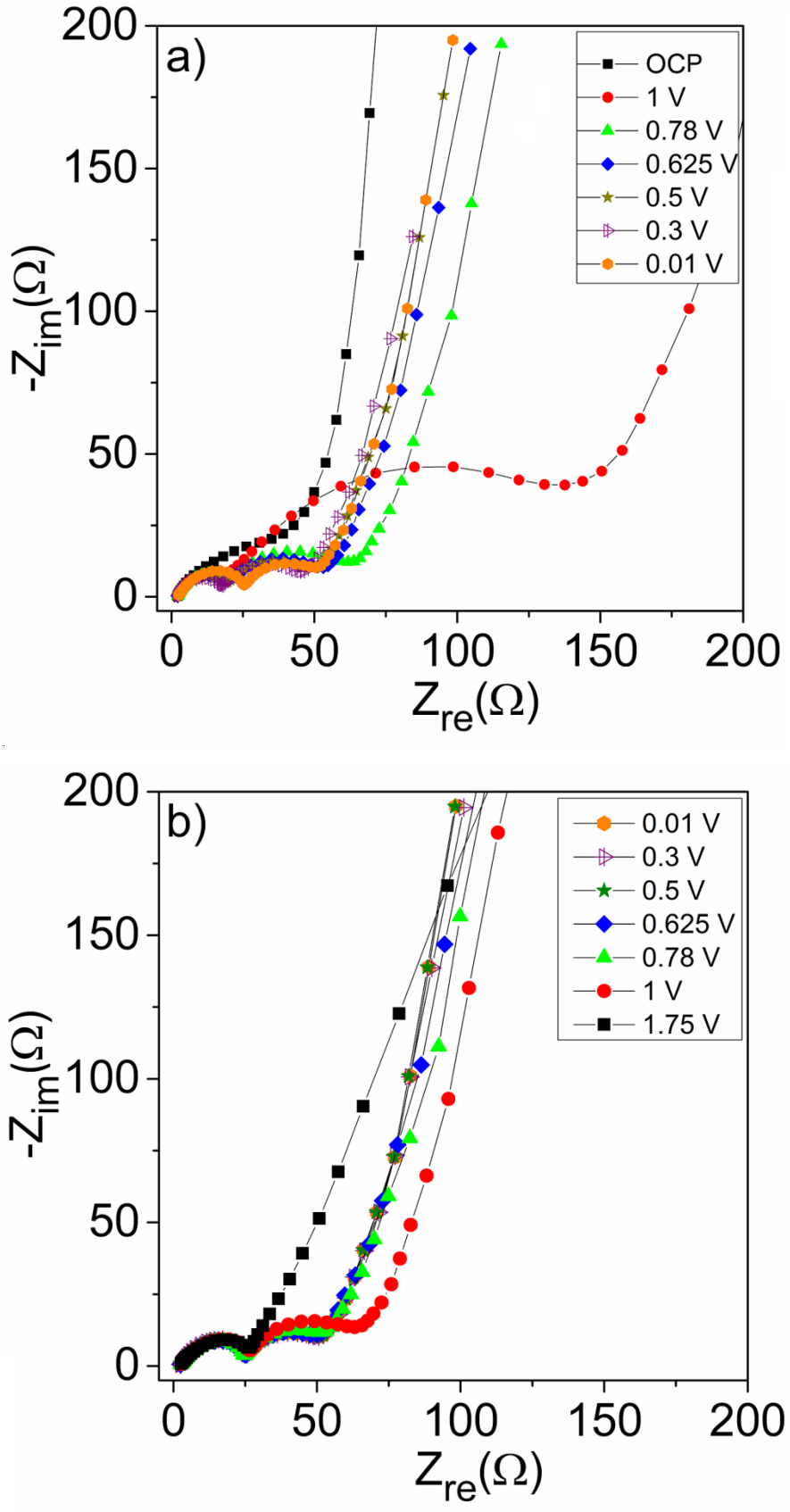

Fig. 5.2 Typical Nyquist plot of SnSb electrode at various potentials for the first (a) alloying and (b) de-alloying reactions.

Fig. 5.3 shows the dependence of the cell voltage on Re, Rsei, and Rct during the discharge/charge. The resistance of the electrolyte corresponding to the intercept of the x-axis at high frequency is not influenced by the potential variations as Re values are around 2 – 3 Ω during lithiation and 2.5 – 3.5 Ω during de-lithiation (Fig. 5.3a). This result shows that the conductivity of the electrolyte remains stable during the discharge/charge of the cell.

In agreement with previous studies, the resistance of the SEI layer increases from 8 Ω to 120 Ω with decreasing of the cell voltage from OCP to 1 V (Fig. 5.3b) suggesting that a thin passive film is formed at the SnSb surface as a result of the electrolyte degradation [15, 21-23]. Then, the Rsei drop at 0.75 V can be explained by the formation of Sn although the continuous decreasing of Rsei values at lower potentials reveals that the SEI layer has cracked due to the volume expansion of the electrode. During de-alloying reactions, Rsei slightly increases as the SEI layer is still forming at the surface. But the low value obtained at 0.75 V vs. Li/Li^+ shows that the structure of the SEI layer is again affected by the volume variations of the electrode. It can be pointed out that at the end of the discharge, the resistance of the SEI is around 13 Ω confirming the presence of the thin insulating layer.

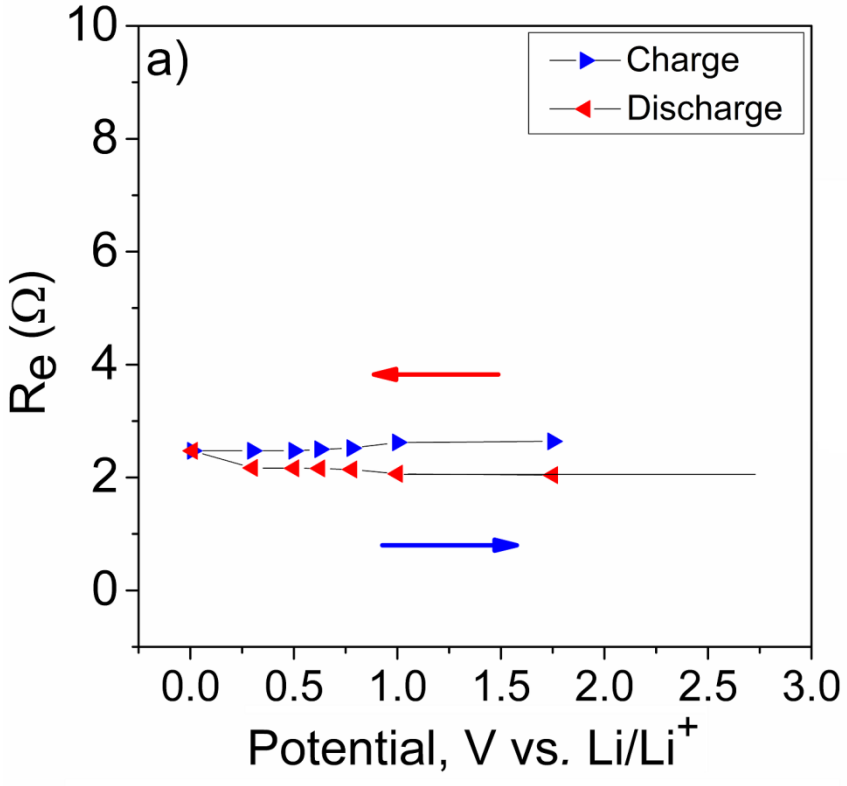

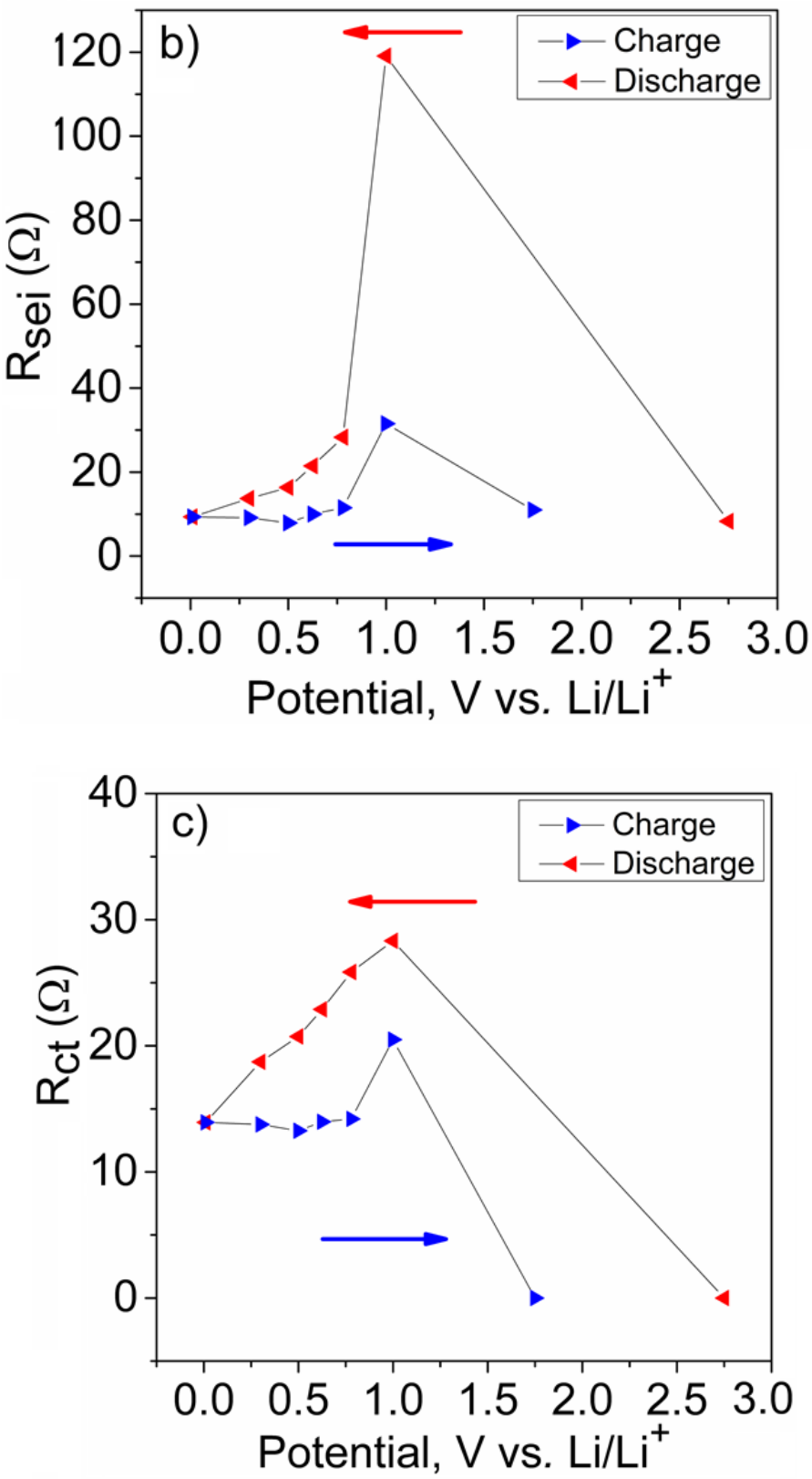

Fig. 5.3 Dependence of (a) R_e, (b) R_{sei}, and (c) R_{ct} on the cell voltage for the first cycle at C/20.

Examination of the charge-transfer resistance as a function of the cell voltage in Fig. 5.3c tends to confirm this assumption. During lithiation, Rct increases up to 28 Ω at 1 V vs. Li/Li^+ due to the formation of the SEI layer. The obvious decreases of Rct for potential lower than 1 V vs. Li/Li^+ can be ascribed to the formation of a porous SEI structure, which allows penetration of the electrolyte. This effect creates new contact between active material and electrolyte which results in the decrease of the charge transfer resistance [24]. During de-lithiation, Rct increases up to 20 Ω at 1 V vs. Li/Li^+, which might be attributed to the restructuring of the SEI layer. But for potential higher than 1 V, the mechanical strains induced by the volume changes of the electrode combined with the reformation of SnSb lead to a low charge-transfer resistance. It can be noticed that the charge transfer resistance at the end of the discharge is in the same order of magnitude than the resistance of the SEI.

The ageing phenomena of SnSb/Li cell were studied by investigating the impedance resistance spectra recorded at the end of discharges up to 50 cycles at C/20 (Fig. 5.4a). The impedance spectra clearly show the widening of the semi-circles corresponding to the continuous increase of the SEI resistance due to the gradually thickening of the layer. However, the SEI thickness tends to reach a constant value as the growth is self-limited owing to the insulating behavior of the layer. Moreover, the line angles decrease up to 45° with cycling suggesting that the electrochemical reactions are governed by the diffusion of Li^+ in the bulk electrode after the 20^{th} cycle. There is almost no change in Re after 50 cycles (Fig. 5.4b). This indicates that there is no modification of the electrolyte ionic conductivity during cycling experiments. Furthermore, the resistance of charge transfer has a low value (~ 4 Ω) and does not change during cycling (Fig. 5.4b) which suggests the SnSb reformation step at the end of charge improves the charge transfer between the anode and electrolyte. Moreover, the cracks induced by large volume change during cycling leads to increase in surface and porosity, thus low Rct. More remarkably, the SEI resistance increases from 13 Ω to 47 Ω between the 1^{st} and the 50^{th} cycle (Fig. 5.4b). This result confirms the continuous growth of a passive layer hindering gradually the electron transfer at the SEI/electrolyte interface with cycling.

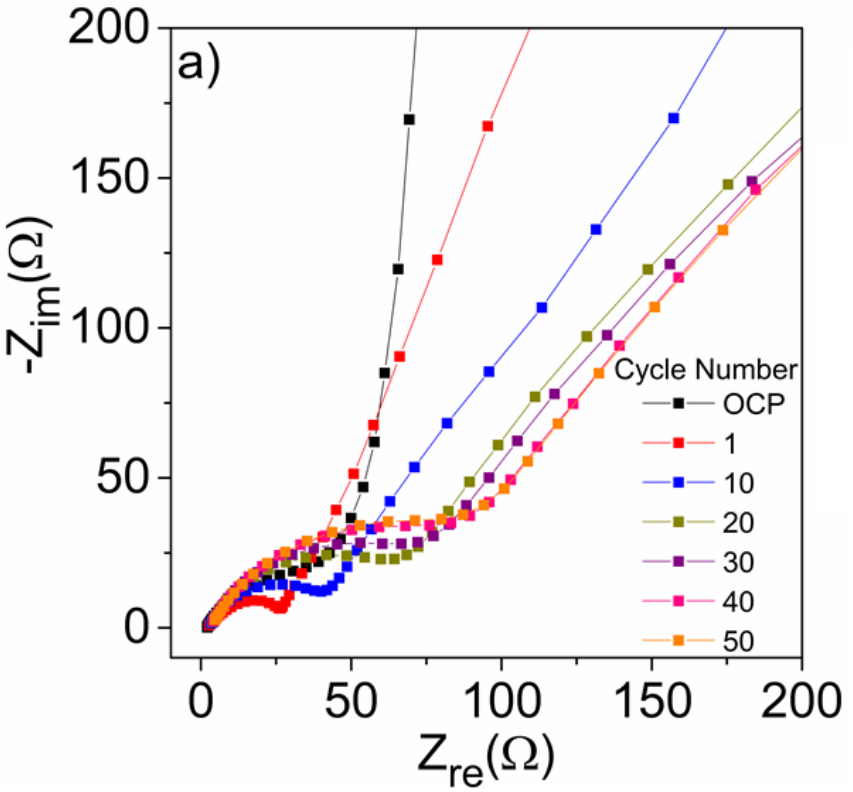
a)
200
150
100
50
0
-Z_im(Ω)
0
50
100
150
200
Z_re(Ω)
Cycle Number
OCP
1
10
20
30
40
50

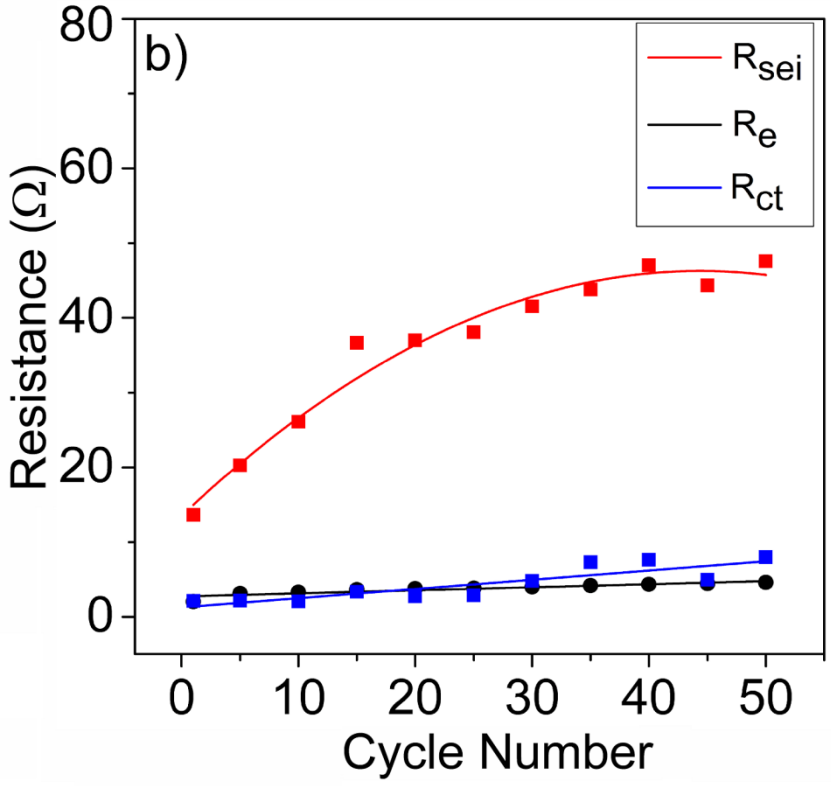
b)
80
60
40
20
0
Resistance (Ω)
0
10
20
30
40
50
Cycle Number
R_sei
R_e
R_ct

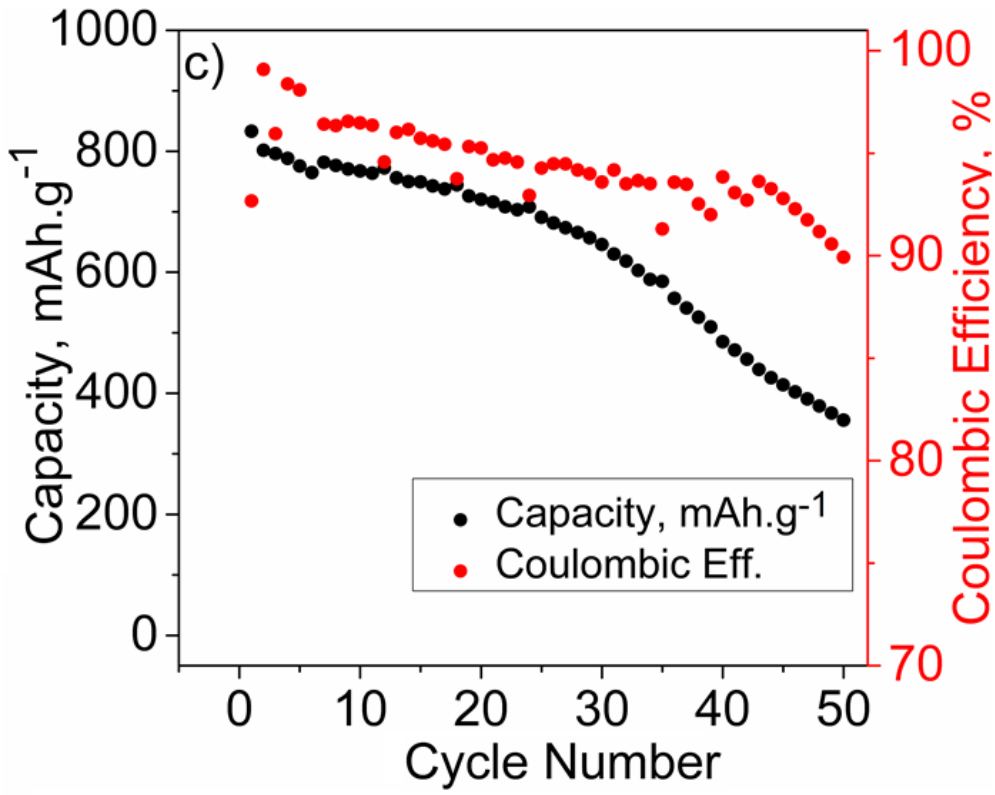

Fig. 5.4 Impedance spectra (a), resistance (b), and capacity and coulombic efficiency (c) of SnSb electrode recorded at the end of discharges at C/20.

As a consequence, the electrochemical performance of SnSb electrode is strongly affected by the formation of the SEI layer. The loss of electrical contact and active material combined with formation of passive layer is responsible for the overall poor electrochemical performance (Fig. 5.4c).

5.3.2 SEI Film Morphology on SnSb Electrode Characterized by Electron Microscopy

To confirm the results obtained by EIS, the morphology of SnSb electrodes have been examined by electron microscopy techniques. Electron microscopy has been widely used for probing the structural features of LIB electrodes [25, 26]. Clearly, the SEM images obtained at different states of discharge and charge reveals that the electrode surface changes as a function of the potential (Fig. 5.5). The as-formed SnSb electrode exhibits a crack-free and rough surface, which is not modified after the cell assembling at OCP (Fig. 5.5 a and b). After discharge at 0.68 V, the surface is covered by a mesoporous SEI layer

showing the presence of large cracks (Fig. 5.5c). This is attributed to the SnSb alloying and the electrolyte decomposition. Further discharging to 0.01 V (Fig. 5.5d) reveals that the SEI film is more porous, suggesting that partial dissolution of the SEI film still occurs.

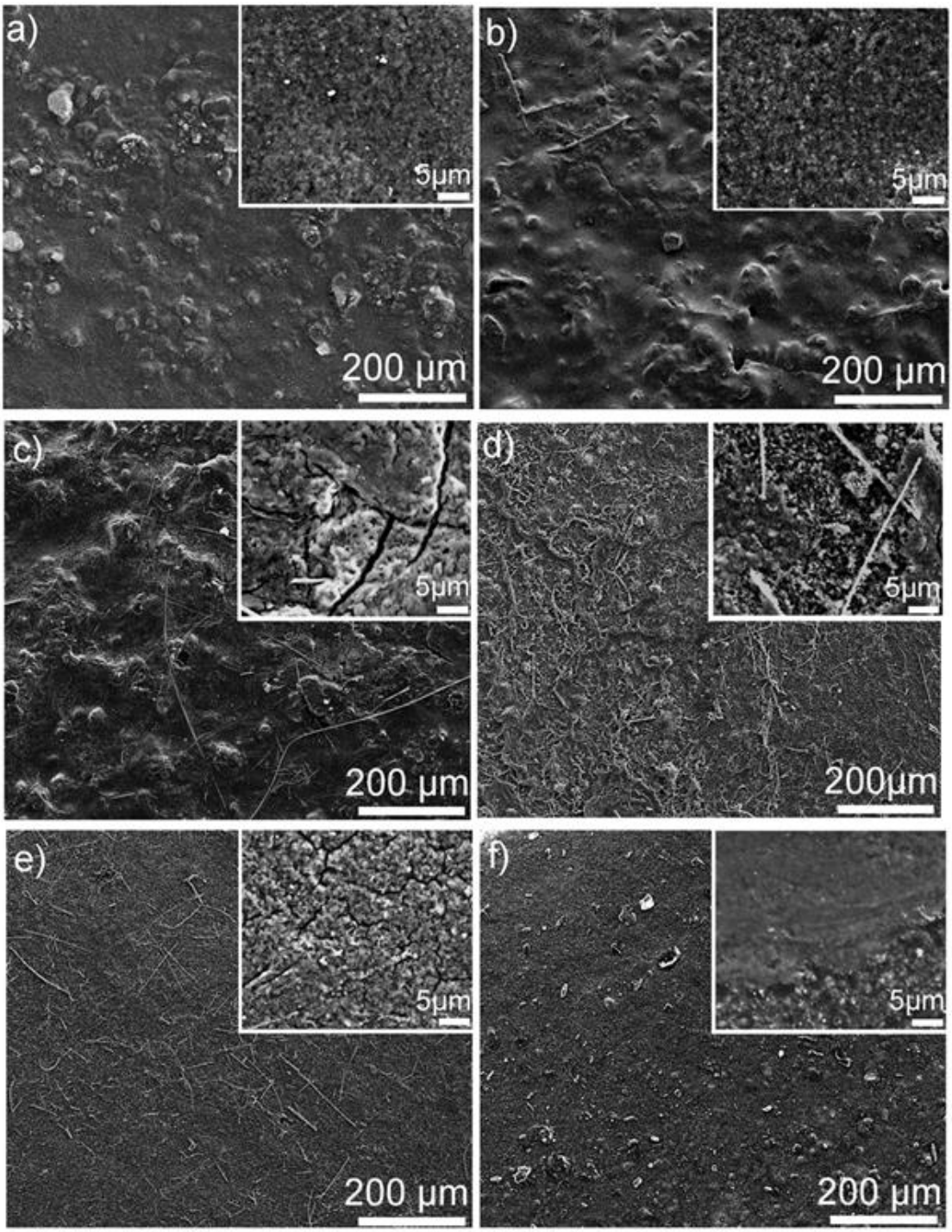

Fig. 5.5 SEM images of as-formed SnSb electrode (a) and SEI film formed at different potentials: OCP (b); first discharge cutoff voltage of 0.68 V (c) and 0.01 V (d); charge cutoff voltage of 0.75 V (e) and 1.75 V (f).

During the first charge to 0.75 V, a porous structure carrying few smaller cracks is again observed (Fig. 5.5e). When the cell charged further to 1.75 V (Fig. 5.5f), the electrode surface tends to adopt the same morphology than that examined before the discharge. This physical restructuring is attributed to the large volume change during the dealloying of SnSb and the electrolyte dissolution. These results in accordance with the EIS analysis confirm the reversible dependence of the SEI film formation on the electrode potential.

The morphological evolution of the SEI was examined by SEM at the end of discharges up to 50 cycles (Fig. 5.6 a – d). Compared to the as-formed SnSb anode, the surface morphology changes drastically after several cycles. After the 5th discharge, there are

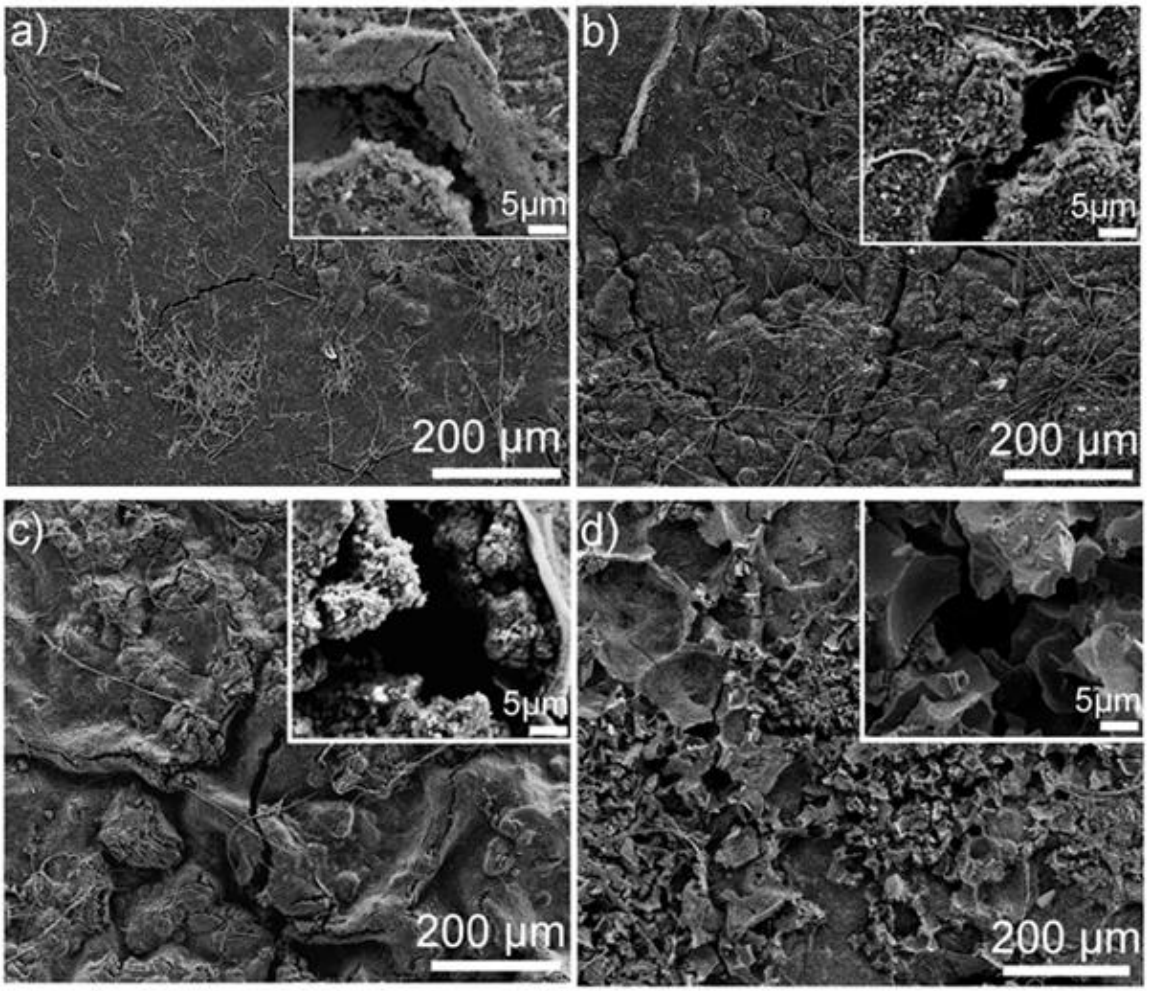

Fig. 5.6 SEM images of SnSb electrode before after the 5th (a), 10th (b), 30th (c), and 50th (d) cycles. The SnSb/Li cell cycled at C/20 in the potential window of 0.01 – 1.75 V vs. Li/Li^{+}.

still visible cracks on the surface of the electrode along with SEI film seems to be deposited mainly near the damaged regions (Fig. 5.6a). This is attributed to the large volume expansion/contraction during the alloying/de-alloying reaction of Li^+ with SnSb alloys [19]. More cracks as well as larger pits and pores can be observed after the 10^{th} cycle (Fig. 5.6b) and accordingly, the regions covered by the SEI film also increased. After the 30^{th} cycle, the electrode surface becomes highly rough with even larger cracks (Fig. 5.6c). Further cycling to 50 cycles (Fig. 5.6d) revealed a very different surface morphology that consisted of a composite material with different size of particles. This is due to the repeated volume change, which results in the pulverization of the SnSb particles. It can be noticed that there is almost no more evolution of the crack openings between the 30^{th} and the 50^{th} discharge.

Ex-situ TEM analysis has been used to investigate the early stages of SEI film formation on SnSb/Li cell. Fig. 5.7 a – e shows TEM images of SnSb electrodes at different states of discharge and charge during the first cycle. The selected area electron diffraction (SAED) pattern (Fig. 5.7a, inset) shows two rings: the inner ring corresponds to the (200) plane and the outer ring corresponds to the (220) plane of SnSb (JCPDS No. 33-0118).

At OCP (Fig. 5.7a), in agreement with impedance analysis, a very thin SEI film (1.4 nm) can be observed. This is attributed to the electrolyte degradation by a simple contact at the surface of SnSb anode. After the cell has been discharged to 0.68 V, the SEI film grows to 6.3 nm suggesting further electrolyte decomposition (Fig. 5.7b). When the cell discharged further to 0.01 V an SEI film thickness of 3.5 nm was obtained (Fig. 5.7c). In

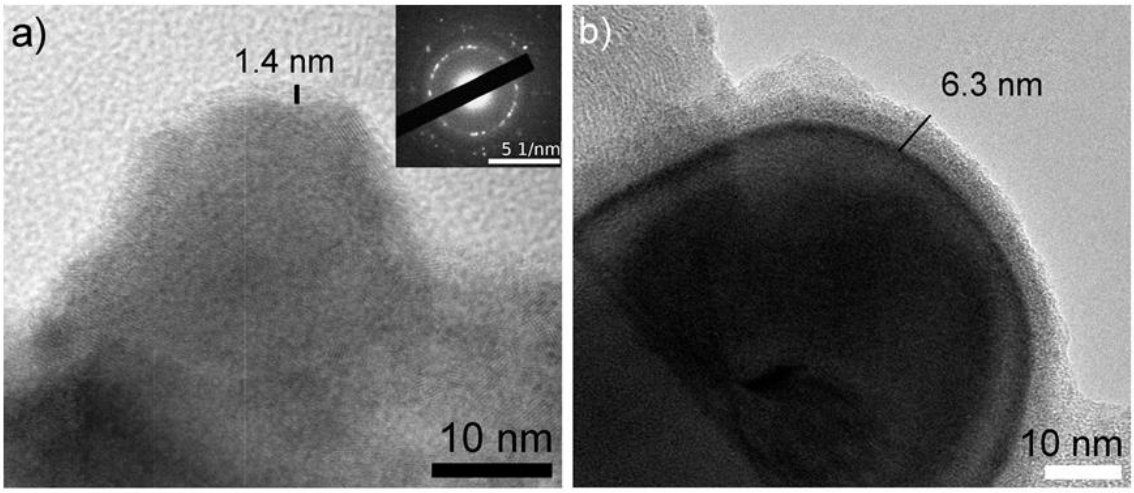

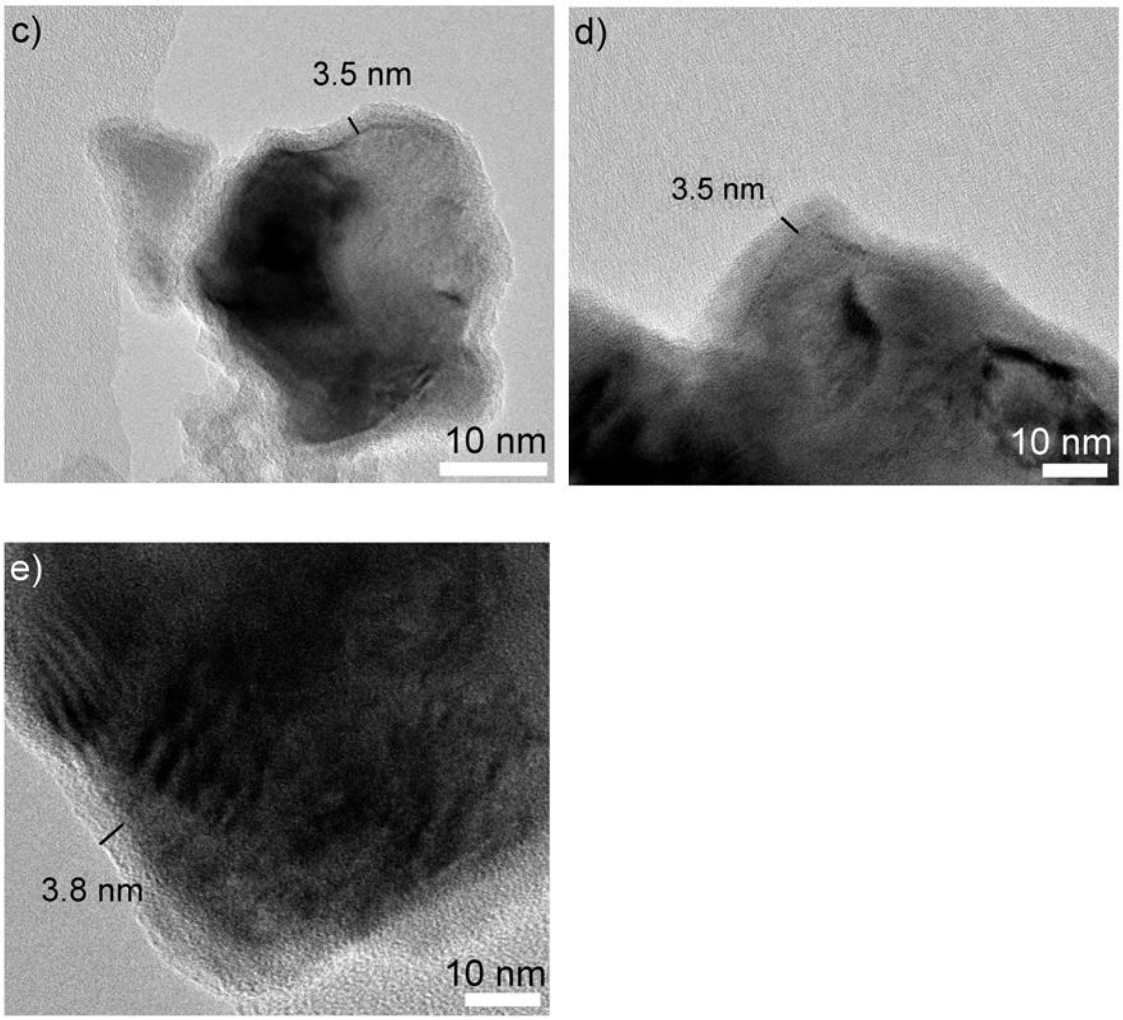

Fig. 5.7 TEM images of SnSb electrode and SEI film at different potentials: at OCP with SAED pattern as inset (a); first discharge cutoff voltage of 0.68 V (b) and 0.01 V (c); charge cutoff voltage of 0.75 V (d) and 1.75 V (e).

agreement with the EIS analyses, the thinning of the film is attributed to the dissolution of the SEI layer that has been formed at higher potential leaving more porous and thinner film. SEI film thickness of 3.5 nm and 3.8 nm were obtained when the cell charged to 0.75 V (Fig. 5.7d) and 1.75 V (Fig. 5.7e), respectively. It's interesting that unlike the discharge (Fig. 5.7 b – c) during charge the restructuring of the SEI film doesn't affect the film thickness.

The evolution of SEI film has been monitored by *ex-situ* TEM analysis at the end of discharges up to 50 cycles (Fig. 5.8). After the first discharge, a thickness of 3.8 nm was obtained (Fig. 5.7e). The surface of the SnSb electrode has clear edge suggesting less

severe morphological change after the first cycle. SEI film thickness of 4.7 nm (Fig. 5.8a) and 5.5 nm (Fig. 5.8b) were obtained after the 10th and 30th cycles, respectively. In agreement with EIS (Fig. 5.4a), the SEI film thickness slightly increased to 5.7 nm after the 50th cycle (Fig. 5.8c). In addition, there is no more clear distinction between the SEI film and the SnSb suggesting high concentration of electrolyte degradation products and the formation of SEI film which contains SnSb particles. This effect could be attributed to repeated volume change during the alloying/dealloying mechanism leading to cracks and pulverization, which creates new surface for further electrolyte decomposition. Similar behaviors have been observed for other alloying/de-alloying anode materials [25, 27].

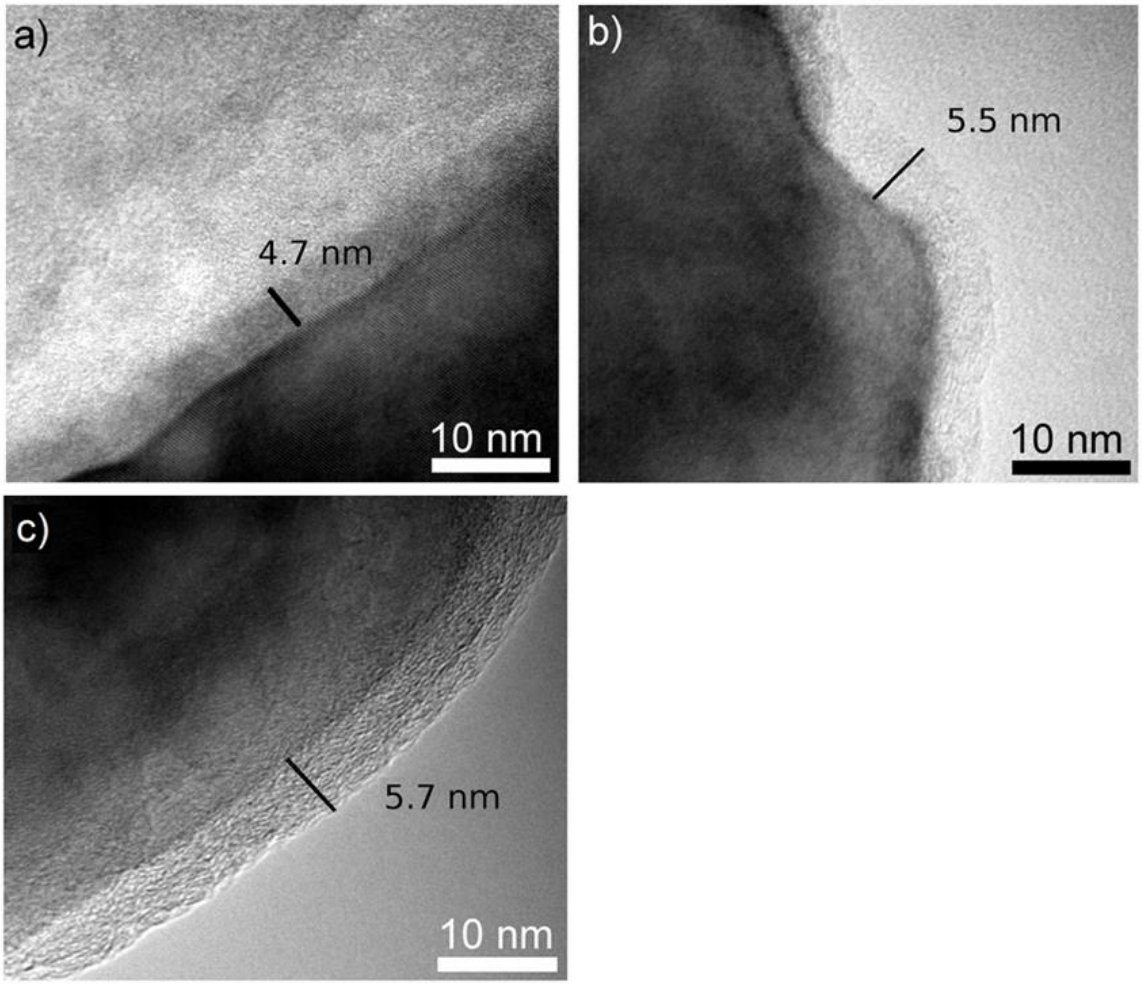

Fig. 5.8 TEM images of SnSb electrode after the 10th (a), 30th (b), and 50th (c) cycles. The SnSb/Li cell cycled at C/20 in the potential window of 0.01 – 1.75 V vs. Li/Li^{+}.

5.3.3 SEI Film Composition Characterized by FTIR and NMR

In order to develop a thorough understanding of the barrier for and mechanism of lithium ion transport through the SEI layer, the composition of the SEI must be better understood. Ex-situ NMR and FTIR has been used widely to characterize the SEI components [28-30]. Previous studies on various anode materials show that the SEI chemistry evolves with cycling experiments [27, 30].

FTIR Analysis on SnSb Electrodes

FTIR spectra were collected from SnSb electrodes extracted from cells cycled after the 1st, 5th, 10th, 30th and 50th cycle, respectively (Fig. 5.9). No peak has been observed for pristine SnSb electrodes (Fig. 9a), while all the cycled electrodes are rich in peaks (Fig. 5.9 b – f). Fig. 9b shows the IR peaks for SnSb electrode after the first cycle located at 3626 (υ_{O-H}), 1619 ($\upsilon_{C=O}$), 1515 ($\upsilon_{C-O\ st}$), 1415 ($\upsilon_{CH_2 bend}$), and 870 ($\upsilon_{C=O}$) cm^{-1}

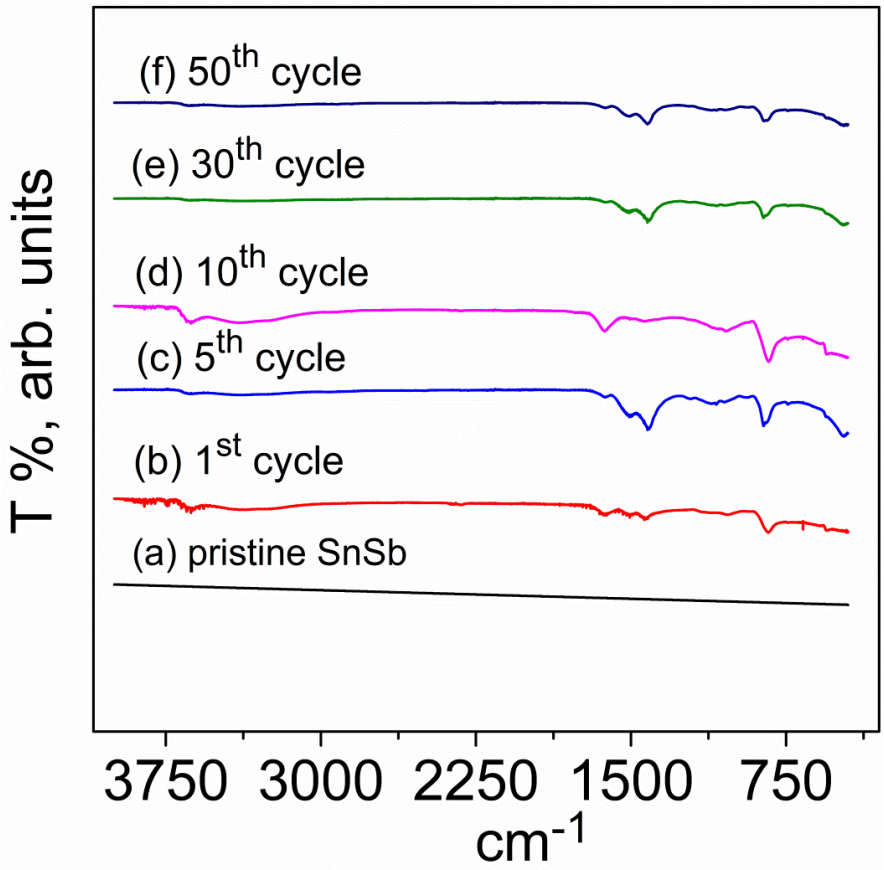

Fig. 5.9 FTIR spectra of pristine (a) and SnSb electrodes after: 1st (b), 5th (c), 10th (d), 30th (e), and 50th (f) cycle.

attributed to LiOH and lithium ethylene dicarbonate (LEDC), major component of EC reduction such as $ROCO_2Li$ and $(CH_2OCO_2Li)_2$, and polymeric decomposition of FEC products [5, 28, 29, 31-33]. Moreover, there are overlapping absorptions peaks associated with Li_2C0_3 at 1415 cm^{-1} and residual $LiPF_6$ at 870 cm^{-1} [32]. Similar trend were observed for SnSb electrodes cycled after 5 (Fig. 5.9c) and 10 (Fig. 5.9d) cycles. Compared to the SnSb electrode after the 5^{th} cycle, the intensity of IR peaks for LEDC and Li_2CO_3 reduced after the 10^{th} cycle while the LiOH peak intensity increased. Fig. 5.9 e and f shows the IR spectrum of SnSb electrodes after the 30^{th} and 50^{th} cycle, respectively. The disappearance of the peak for LiOH after the 30^{th} cycle suggests that the inorganic part of the SEI film decomposes while the organic component of the SEI film thickens.

NMR Analysis on SnSb Electrodes Extracted with D_2O

To further characterize the composition of the SEI film on SnSb anodes, ^{1}H, ^{13}C, and ^{19}F NMR spectroscopy of D_2O extracts of the SnSb electrodes has been conducted after the 1^{st}, 5^{th}, 10^{th}, 30^{th}, and 50^{th} cycle. The ^{1}H NMR spectra of extracts of SnSb electrodes after the first cycle contain no peak. After the fifth cycle IR peaks at 3.51, (3.6 and 1.86), 3.79, 3.68 ppm are consistent with lithium ethylene dicarbonate (LEDC, $(CH_2OC_2Li)_2$), lithium butylene dicarbonate (LBDC, $(CH_2CH_2OCO_2Li)_2$), lithium ethylene carbonate (LEC, $CH_3CH_2OCO_2Li$), and polyethyelene oxide (PEO, $-OCH_2CH_2O-$), respectively (Fig. 5.10b) [29, 31, 34]. These SEI products have been observed on graphite and silicon electrodes cycled in electrolyte containing EC, PC, FEC and VC, and thus the same reduction products are expected for SnSb electrodes [25, 31, 34]. Similar IR peaks have been observed in Fig. 5.10 c, d, and e for SnSb electrodes after the 10^{th}, 30^{th} and 50^{th} cycle, respectively. The continuous increasing intensity of the LEDC resonance suggests that the electrolyte reduction still pursues and that the SnSb anode is not totally passivated. This effect could be attributed to the large volume expansion during alloying leading to the formation of new surface sites for further electrolyte decomposition. The results are consistent with previous reports of continuous electrolyte reduction on alloy electrodes due to the large volume changes [25]. The lack of passivation is one of the most severe problems for SnSb electrodes and is the main contributor to poor cycling performance.

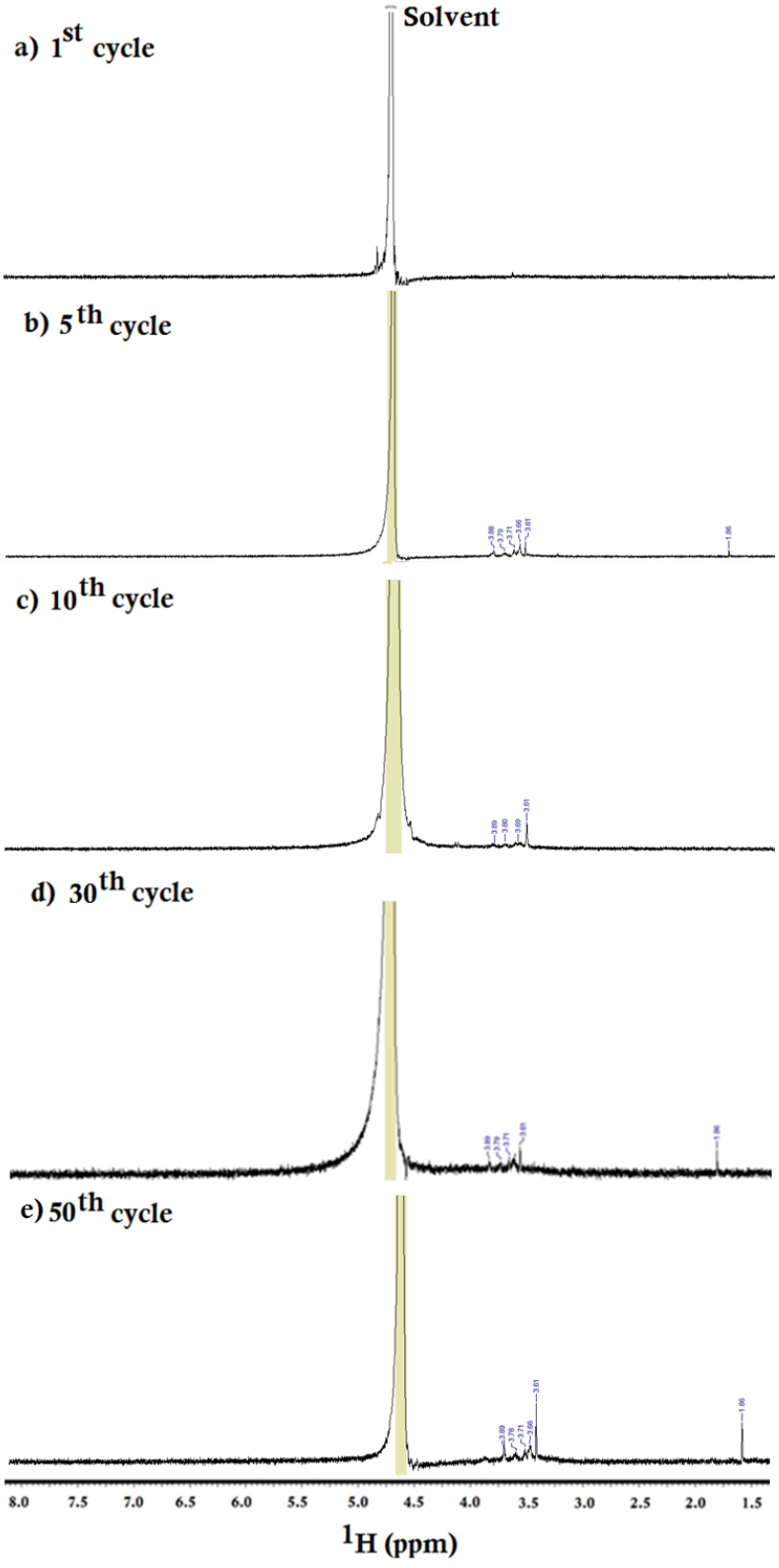

Fig. 5.10 (a) ^{1}H NMR spectra of SnSb electrode cycled after 1st (a), 5th (b), 10th (c), 30th (d), and 50th (e) cycle.

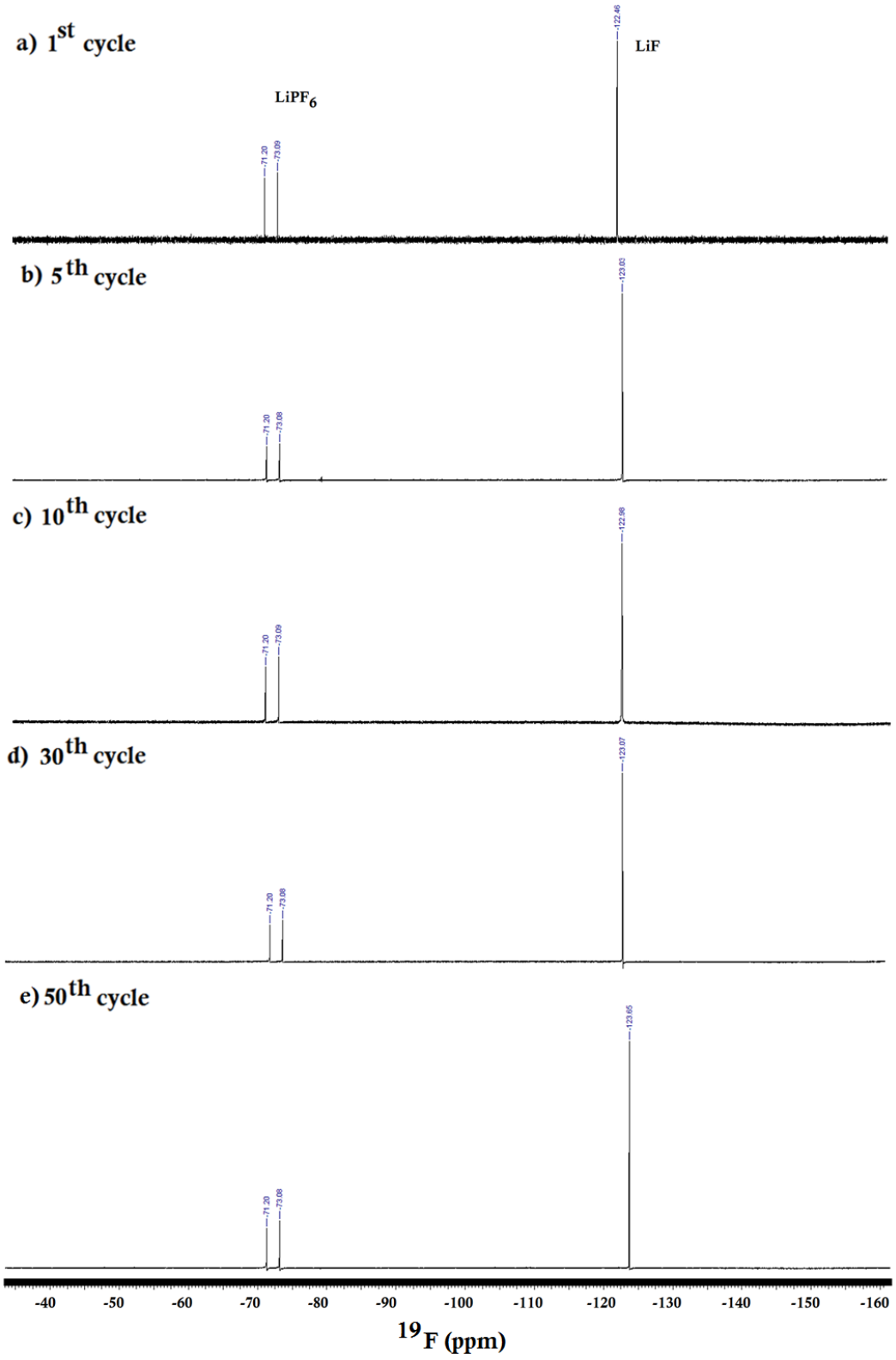

Fig. 5.11 (a) ^{19}F NMR spectra of SnSb electrode cycled after 1st (a), 5th (b), 10th (c), 30th (d), and 50th (e) cycle.

The ^{19}F NMR spectra of extracts from cycled SnSb electrodes contain peaks characteristic of residual $LiPF_6$ at −72.2 ppm (d) and a peak at −123 ppm (s), characteristic of LiF [25, 34, 35]. The concentration of LiF increases with increasing cycle number, suggesting that both the organic solvent and inorganic salt of the electrolyte continue to be reduced throughout the cycling process (Fig. 5.11 a – e). Moreover, previous reports have shown the presence of FEC in the electrolyte contributes to formation of LiF [25, 34]. It can be pointed out that only $LiPF_6$ and LiF were detected by ^{19}F NMR indicating that PFx or POFx, if present, are only there in low concentrations.

For ^{13}C NMR, unfortunately, because of the low concentration of the SEI products, such as LEDC, and the absence of hydrogen atoms directly attached to carbonyl carbon (lack of nuclear Overhauser effect) the resonance for the C=O is too weak to be observed.

To verify the structural stability of SnSb electrode, XRD analysis where carried out after 50 cycles (Fig. 5.12). The XRD patterns evidence that no new peaks appear after cycling, suggesting the SnSb structure is preserved.

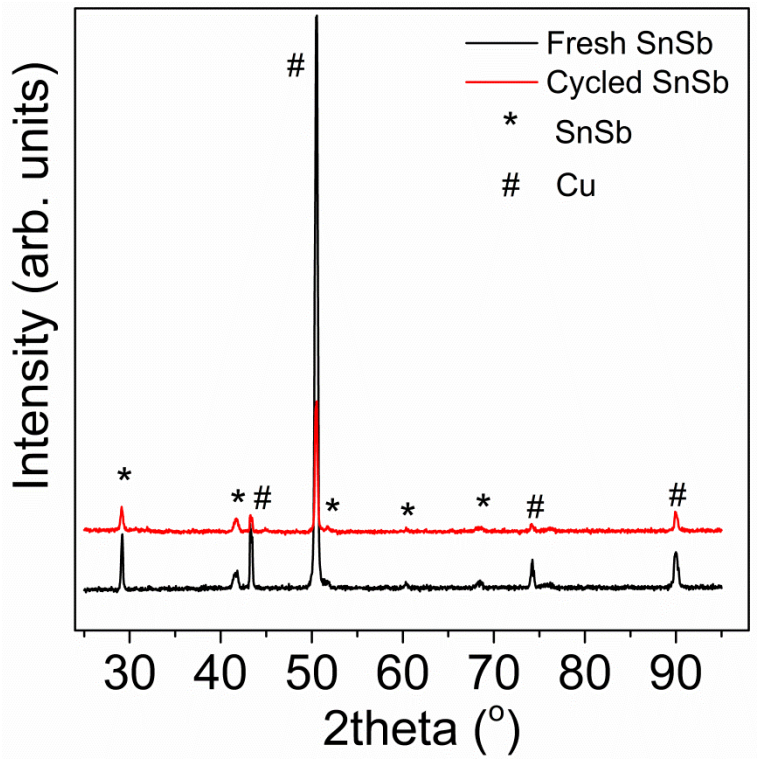

Fig. 5.12 XRD patterns of SnSb before and after galvanostatic cycling.

5.4 Conclusion

In this chapter, we have studied the electrochemical characteristics of SnSb electrode by EIS, electron microscopy, and chemical techniques. The results show that the formation of a SEI layer occurs as soon as the electrode is in contact with the electrolyte. The composition of the SEI film was characterized via FTIR and NMR spectroscopy of the D_2O extracts of the SnSb electrode. The primary components of the SEI formed are LEDC and LiF. The determination of the SEI resistance and the charge transfer resistance confirm that the electrode is the subject of large volume variations combined with the gradual growth of the SEI layer during discharge/charge up to the 50^{th} cycle. As a consequence, the loss of electrical contact combined with the formation of the passive layer hindering the electron transfer is responsible for the capacity fading during the first 50 cycles.

To limit the capacity fade we propose the use of protective layer on the electrode surface which will be discussed in detail the next chapter.

5.5 References

[1] S. Goriparti, E. Miele, F. De Angelis, E. Di Fabrizio, R. Proietti Zaccaria, C. Capiglia, Review on recent progress of nanostructured anode materials for Li-ion batteries, J. Power Sources, 257 (2014) 421-443.

[2] B. Scrosati, J. Garche, Lithium batteries: Status, prospects and future, J. Power Sources, 195 (2010) 2419-2430.

[3] A.T. Tesfaye, R. Gonzalez, J.L. Coffer, T. Djenizian, Porous silicon nanotube arrays as anode material for Li-ion batteries, ACS Appl. Mater. Interfaces, 7 (2015) 20495-20498.

[4] J. Chen, Recent progress in advanced materials for lithium ion batteries, Materials, 6 (2013) 156-183.

[5] P. Verma, P. Maire, P. Novák, A review of the features and analyses of the solid electrolyte interphase in Li-ion batteries, Electrochim. Acta, 55 (2010) 6332-6341.

[6] H. Bryngelsson, M. Stjerndahl, T. Gustafsson, K. Edström, How dynamic is the SEI?, J. Power Sources, 174 (2007) 970-975.

[7] H. Mukaibo, T. Osaka, P. Reale, S. Panero, B. Scrosati, M. Wachtler, Optimized Sn/SnSb lithium storage materials, J. Power Sources, 132 (2004) 225-228.

[8] M. Wachtler, J.O. Besenhard, M. Winter, Tin and tin-based intermetallics as new anode materials for lithium-ion cells, J. Power Sources, 94 (2001) 189-193.

[9] H.A. Wilhelm, C. Marino, A. Darwiche, L. Monconduit, B. Lestriez, Significant electrochemical performance improvement of TiSnSb as anode material for Li-ion batteries with composite electrode formulation and the use of VC and FEC electrolyte additives, Electrochem. Commun., 24 (2012) 89-92.

[10] S.S. Zhang, A review on electrolyte additives for lithium-ion batteries, J. Power Sources, 162 (2006) 1379-1394.

[11] P. Antitomaso, B. Fraisse, L. Stievano, S. Biscaglia, D. Aymé-Perrot, P. Girard, M.T. Sougrati, L. Monconduit, SnSb electrodes for Li-ion batteries: the electrochemical mechanism and capacity fading origins elucidated by using operando techniques, J. Mater. Chem. A, 5 (2017) 6546-6555.

[12] M. Wagner, P. Raimann, A. Trifonova, K.-C. Moeller, J. Besenhard, M. Winter, Electrolyte decomposition reactions on tin-and graphite-based anodes are different, Electrochem. Solid State Lett., 7 (2004) A201-A205.

[13] W. Zhang, F. Ghamouss, A. Darwiche, L. Monconduit, D. Lemordant, R. Dedryvère, H. Martinez, Surface film formation on TiSnSb electrodes: Impact of electrolyte additives, J. Power Sources, 268 (2014) 645-657.

[14] C. Marino, A. Darwiche, N. Dupré, H.A. Wilhelm, B. Lestriez, H. Martinez, R. Dedryvère, W. Zhang, F. Ghamouss, D. Lemordant, L. Monconduit, Study of the electrode/electrolyte interface on cycling of a conversion type electrode material in Li batteries, J. Phys. Chem. C, 117 (2013) 19302-19313.

[15] A. Mahmoud, M. Chamas, P.-E. Lippens, Electrochemical impedance study of the solid electrolyte interphase in MnSn2 based anode for Li-ion batteries, Electrochim. Acta, 184 (2015) 387-391.

[16] S.S. Zhang, K. Xu, T.R. Jow, EIS study on the formation of solid electrolyte interface in Li-ion battery, Electrochim. Acta, 51 (2006) 1636-1640.

[17] T. Ong, H. Yang, Symmetrical cell for electrochemical AC impedance studies of lithium intercalation into graphite, Electrochem. Solid State Lett., 4 (2001) A89-A92.

[18] N. Takami, A. Satoh, M. Hara, T. Ohsaki, Structural and kinetic characterization of lithium intercalation into carbon anodes for secondary lithium batteries, J. Electrochem. Soc., 142 (1995) 371-379.

[19] L. Simonin, U. Lafont, E. Kelder, SnSb micron-sized particles for Li-ion batteries, J. Power Sources, 180 (2008) 859-863.

[20] M. Winter, J.O. Besenhard, Electrochemical lithiation of tin and tin-based intermetallics and composites, Electrochim. Acta, 45 (1999) 31-50.

[21] X. Zhang, R. Kostecki, T.J. Richardson, J.K. Pugh, P.N. Ross, Electrochemical and infrared studies of the reduction of organic carbonates, J. Electrochem. Soc., 148 (2001) A1341-A1345.

[22] S. Naille, R. Dedryvère, H. Martinez, S. Leroy, P.E. Lippens, J.C. Jumas, D. Gonbeau, XPS study of electrode/electrolyte interfaces of η-Cu6Sn5 electrodes in Li-ion batteries, J. Power Sources, 174 (2007) 1086-1090.

[23] K.K.D. Ehinon, S. Naille, R. Dedryvère, P.E. Lippens, J.C. Jumas, D. Gonbeau, Ni3Sn4 electrodes for Li-ion batteries: Li–Sn alloying process and electrode/electrolyte interface phenomena, Chem. Mater., 20 (2008) 5388-5398.

[24] Y. Xia, Z. Xiao, X. Dou, H. Huang, X. Lu, R. Yan, Y. Gan, W. Zhu, J. Tu, W. Zhang, X. Tao, Green and facile fabrication of hollow porous MnO/C microspheres from microalgaes for lithium-ion batteries, ACS Nano, 7 (2013) 7083-7092.

[25] C.K. Chan, R. Ruffo, S.S. Hong, Y. Cui, Surface chemistry and morphology of the solid electrolyte interphase on silicon nanowire lithium-ion battery anodes, J. Power Sources, 189 (2009) 1132-1140.

[26] P. Lu, C. Li, E.W. Schneider, S.J. Harris, Chemistry, impedance, and morphology evolution in solid electrolyte interphase films during formation in lithium ion batteries, J. Phys. Chem. C, 118 (2014) 896-903.

[27] M. Nie, D.P. Abraham, Y. Chen, A. Bose, B.L. Lucht, Silicon solid electrolyte interphase (SEI) of lithium ion battery characterized by microscopy and spectroscopy, J. Phys. Chem. C, 117 (2013) 13403-13412.

[28] K. Xu, G.V. Zhuang, J.L. Allen, U. Lee, S.S. Zhang, P.N. Ross, T.R. Jow, Syntheses and characterization of lithium alkyl mono-and dicarbonates as components of surface films in Li-ion batteries, J. Phys. Chem. B, 110 (2006) 7708-7719.

[29] Y. Wang, S. Nakamura, M. Ue, P.B. Balbuena, Theoretical studies to understand surface chemistry on carbon anodes for lithium-ion batteries: reduction mechanisms of ethylene carbonate, J. Am. Chem. Soc., 123 (2001) 11708-11718.

[30] D. Aurbach, B. Markovsky, A. Rodkin, M. Cojocaru, E. Levi, H.-J. Kim, An analysis of rechargeable lithium-ion batteries after prolonged cycling, Electrochim. Acta, 47 (2002) 1899-1911.

[31] G.V. Zhuang, K. Xu, H. Yang, T.R. Jow, P.N. Ross, Lithium ethylene dicarbonate identified as the primary product of chemical and electrochemical reduction of EC in 1.2 M LiPF6/EC: EMC electrolyte, J. Phys. Chem. B, 109 (2005) 17567-17573.

[32] A.S. Cavanagh, Y. Lee, B. Yoon, S. George, Atomic layer deposition of LiOH and Li2CO3 using lithium t-butoxide as the lithium source, ECS transactions, 33 (2010) 223-229.

[33] V. Etacheri, O. Haik, Y. Goffer, G.A. Roberts, I.C. Stefan, R. Fasching, D. Aurbach, Effect of fluoroethylene carbonate (FEC) on the performance and surface chemistry of Si-nanowire Li-ion battery anodes, Langmuir, 28 (2011) 965-976.

[34] A.L. Michan, M. Leskes, C.P. Grey, Voltage dependent solid electrolyte interphase formation in silicon electrodes: monitoring the formation of organic decomposition products, Chem. Mater., 28 (2015) 385-398.

[35] D. Aurbach, Review of selected electrode–solution interactions which determine the performance of Li and Li ion batteries, J. Power Sources, 89 (2000) 206-218.

CHAPTER 6

COATING OF SnSb BY A THERMOPLASTIC ELASTOMER FOR THE SEI GROWTH CONTROL

The objective of this chapter is to investigate electrochemical performance of micron-sized SnSb electrode coated with thermoplastic elastomer protective film, namely poly(styrene-*b*-2-hydroxyethyl acrylate), as a negative electrode for LIBs. The high failure strain characteristics of elastomer is a very desirable features for rechargeable LIBs because a high specific capacity anode materials, such as SnSb, are susceptible to large volume change and continuous SEI growth during cycling lead to poor electrochemical performance.

6.1 Introduction

As discussed in detail in Chapter 5 during cycling the SnSb suffer from large volume change and the formation of unstable SEI film. As a consequence, the loss of electrical contact and active material (between SnSb particles and between SnSb and conductive additive particles) combined with the formation of the passive layer hindering the electron transfer is responsible for the poor electrochemical performances.

Many efforts have been devoted to improve the cycling stability, which include chemical modification of the electrolyte by adding various additives likes VC and FEC to create a thin stable protective layer [1-4]; and the modification of the electrode/electrolyte interface by coating the electrode surface with inorganic (such as Ni, Al_2O_3) and organic (such as self-healing polymer, polyaniline) layer [5-9]. In this chapter, the latter concept is developed by coating the micron-sized SnSb anode electrode with thin block copolymer film, namely, poly(styrene-*b*-2-hydroxyethyl acrylate) (PS-*b*-PHEA) to improve the electrochemical performance.

Thermoplastic elastomers (TPEs) based on block copolymers are advantageous compared to classical thermoset rubbers. Indeed, TPEs combine the elastic properties of vulcanized rubbers with the processing properties and the recyclability of thermoplastics. Typically, TPEs, such as Poly(styrene-butadiene-styrene) SBS, are based on block- or graft-copolymer, i.e. capable of self-assembling in nanostructures with hard spheres, which ensure physical crosslinking and stiffness, dispersed in a soft rubbery matrix.

PS-*b*-PHEA was designed to coat SnSb and ensure a good bonding of the active materials together and maintain a good adhesion. Indeed, PHEA, which is known for its biocompatibility and lack of toxicity, is rubbery at room temperature. Moreover, the block copolymer is expected to have a good affinity for SnSb thanks to hydrogen bonding between the hydroxyl groups, which are present as pendant functions on PHEA and on the surface of the inorganic particles [10]. In order to obtain a well-defined block copolymer, it was synthetized by controlled radical polymerization, i.e. by nitroxide

mediated polymerization (NMP). NMP allows for precise control of molecular parameters such as PS and PHEA length, molecular weight, dispersity to tune the mechanical properties of the copolymer. To the best of our knowledge, it is the first time that PS-*b*-PHEA obtained by NMP.

6.2 Experimental Section

6.2.1 Material and Instrumentation

Tetrahydrofurane (THF), N,N-Dimethylformamide (DMF), Methanol, 2-hydroxyethyl acrylate (HEA) and styrene (MEA) were purchased from Sigma-Aldrich and were used as received. (*N*-*tert*-butyl-*N*-(1'-diethylphosphono-2,2'-dimethylpropyl)-*O*-(2-carboxyl-prop-2-yl) (MAMA-SG1) alkoxyamine initiator (registered as trademark BlocBuilder by Arkema) and *N*-*tert*-butyl-*N*-(1'-diethylphosphono-2,2'-dimethylpropyl) (SG1, 85%) free nitroxide were provided by Arkema and were used as received.

The SEC experiments for PS-SG1 macroinitiator were performed on an EcoSEC apparatus from PSS, equipped with a dual flow cell refractive index detector. Eluent was THF at a flow rate of 0.3 mL min^{-1} for the sample pump and 0.15 mL min^{-1} for the reference pump. The stationary phase was a combination of one PL Resipore (50x4.6) mm guard column and two PL Resipore (250x4.6) mm columns thermostated at 40 °C. Samples were prepared at concentration of 0.25 wt. % in THF containing 0.25 vol. % of toluene, as a flowmarker. Injection volume was 20 µL. Polystyrene equivalent number-average molar masses (M_n) and dispersities $Đ$ were calculated by means of PS calibration curve using PS-M Easivial standards (Agilent, USA). SEC experiments for PS-b-PHEA were carried out on the following columns were used: one pre-column and two PL Resipore columns. The injection loop, the columns and the RI detector were in the same oven thermostated at 70 °C. The eluent was a solution of 0.1 M LiBr in dimethylformamide and the flow rate was fixed at 0.7 mL min^{-1}. The samples were prepared in a mixture of eluent and toluene (0.25 vol. %) as flowmarker, filtered through a 0.2 µm Nylon filter (Interchim) and placed in an auto-sampler preheated at 50°C. Samples concentration

was 0.25 wt. %. Calibration curves were established with poly(methyl methacrylate) (PMMA) standards purchased from PSS polymers.

6.2.2 Block-copolymer Synthesis

6.2.2.1 Synthesis of Macroinitiator, PS-SG1

Schematic 1a shows the initiation mechanism of alkoxyamine. 0.768 g of MAMA-SG1, (25.6 mmol) and 20 g of styrene (192 mmol, 95 eq.) were placed in a three-neck round-bottom flask equipped with a reflux condenser and a magnetic stir bar. The mixture was purged for 30 min with argon to remove oxygen. The mixture was immersed in an oil bath and heated to 120 °C (in the solution) with a 30 min ramp temperature. After 2h, cooling down the mixture in an ice bath stopped the polymerization. The crude product was diluted in 20 mL of THF and then poured into a large excess of cold ethanol. The solid was collected by filtration, re-dissolved in THF, and re-precipitated in cold methanol. The precipitate was filtered off, and then dried under vacuum (5×10^{-2} mbar). The M_n was 6496 g mol^{-1} with a $Đ$ of 1.13.

6.2.2.2 Synthesis of Poly(styrene-*b*-2-hydroxyethyl acrylate) Block Copolymer, PS-*b*-PHEA

The synthesis mechanism of PS-b-PHEA is shown in schematic 1c. 0.4418 g of PS-SG1 macroinitiator (0.068 mmol) and 1.98 mg of SG1 free nitroxide (0.00674 mmol, 0.1 eq.), dissolved in 4 g of DMF, were placed in a three-neck round-bottom flask equipped with a reflux condenser and a magnetic stir bar (schematic 1b). Then 4.002 g of HEA (34.5 mmol, 507 eq.) were added and the solution was purged for 30 min with argon to remove oxygen. The mixture was immersed in an oil bath and heated to 120°C (in the solution) with a 20 min ramp temperature. Aliquots were withdrawn periodically for monitoring conversions by ^{1}H NMR and molar masses by SEC. After 90 min, cooling down the mixture in an ice bath stopped the polymerization. The final conversion was 82 %. The crude product was diluted in 15 mL of THF and then poured into a large excess of cold diethyl ether. The precipitated viscous polymer stuck on the bottom of the beaker and was collected by decanting the solvent in the fridge, followed by washing

3 times with diethyl ether and drying under reduced pressure. The solid was re-dissolved in DMF and then re-precipitated in cold diethyl ether. Finally, the solvent was decanted in the fridge, followed by washing 3 times with diethyl ether, and drying under reduced pressure, yielding the desired copolymer with M_n = 65200 g mol^{-1} and $Đ$ = 1.91 (by SEC in DMF at 70°C relative to PMMA standards).

6.2.3 Electrode Fabrication

PS-*b*-PHEA was dissolved in DMF (1.5 ml) and then mixed with carbon black and Li-salt (Bis(trifluoromethane)sulfonimide, LiTFSi) with a mass ratio of 70:15:15 using magnetic stirrer to obtain a homogenous suspension. The suspension is then drop cast onto Teflon and dried overnight at 80 ^{o}C to form a conductive elastomer thin film. The SnSb electrode was fabricated using slurry cast method by mixing a SnSb powder, binding agent polyvinylidene fluoride (PVDF), and conducting agent (Carbon black Sp) with mass ratio of 70:15:15 in vibrational ball milling for 25 min at 20 Hz. The slurry was tape casted on Cu current collector at room temperature for 24 h and then further dried at 110 ^{0}C for 12 h under vacuum. Then the SnSb electrode was heated to 90 ^{0}C on a hot plate. The conductive polymer film was then melted at 100 ^{0}C and coated on the SnSb electrode with a sharp blade, henceforth SnSb (PS-*b*-PHEA). The electrodes were degassed in vacuum at room temperature overnight and transferred to an argon glove box for battery assembly.

Cyclic voltammetry (CV) and galvanostatic cycling with potential limitation (GCPL) were performed using standard two-electrode Swagelok cells assembled in a glove box with high purity argon. The half-cells were consisted of SnSb (PS-*b*-PHEA) as the working electrode and a battery grade lithium foil as the counter electrode. The two electrodes were separated by Whatman glass microfiber soaked in the liquid electrolyte (1 M $LiPF_6$ in EC:PC:3DMC with 1 vol. % VC and 5 vol. % FEC). The CV was performed in potential window of 0.01 − 1.75 V vs. Li/Li$^+$ at a scan rate of 0.1 mV s^{-1}. The galvanostatic tests of the assembled cells were done at multiple C-rates.

6.3 Results and Discussion

6.3.1 Material Synthesis

Scheme 6.1 describes the synthesis of PS-*b*-PHEA. In the first step (Scheme 6.1 a and b), polystyrene PS-SG1 with low molecular weight and dispersity (M_n = 6496 g mol^{-1} and $Đ$ = 1.13) was synthetized in bulk in the presence of MAMA-SG1 as initiator/controlling agent at 120°C. Schematic 1c shows, PS-SG1 was used as alkoxyamine macroinitiator to perform the controlled polymerization of HEA in DMF at 120°C. A small amount of free nitroxide SG1 was also added, since it is known to improve the control of acrylates

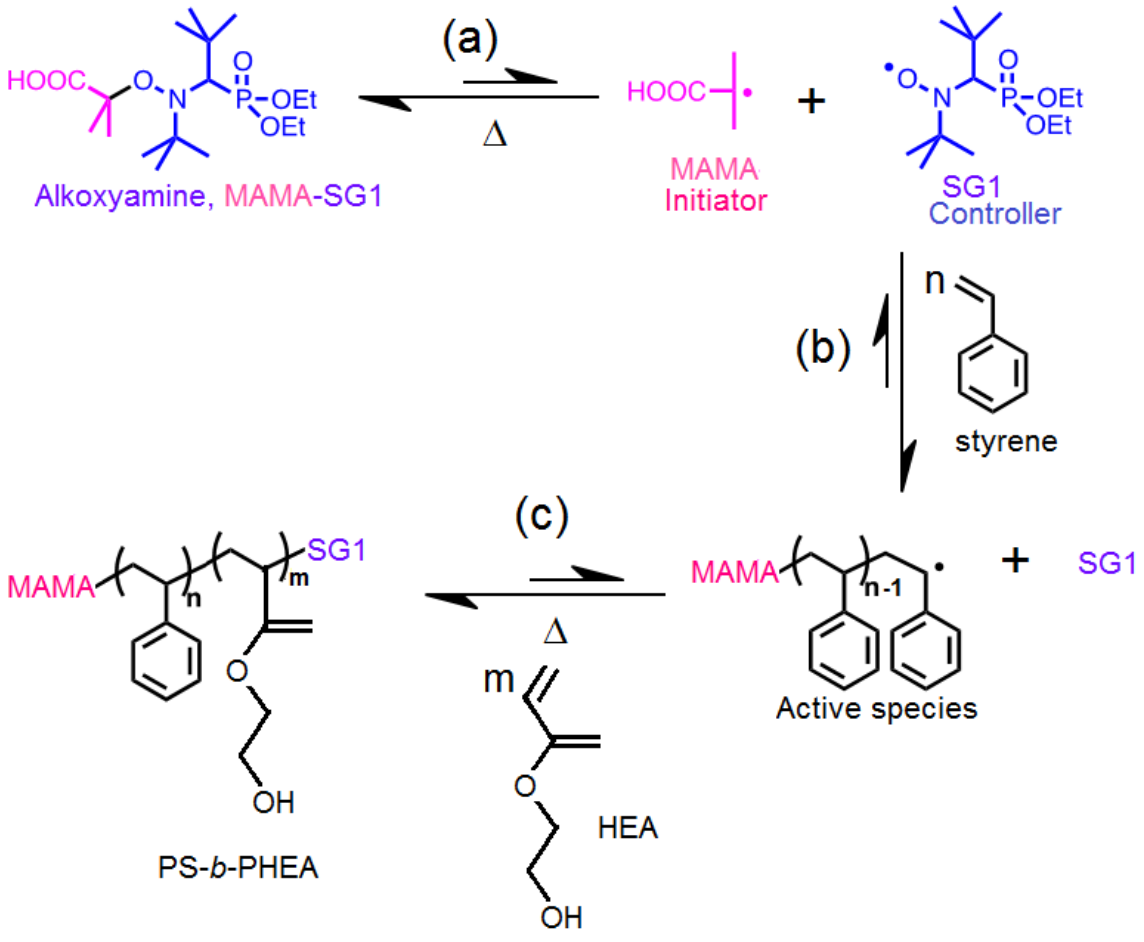

Scheme 6.1. The synthesis mechanism of PS-*b*-PHEA using NMP: (a) Initiation of radicals, (b) initiation of macroinitiator, reaction mechanism of NMP with styrene, and (c) synthesis of block copolymer PS-*b*-PHEA.

polymerization [11]. Moreover kinetics was carried out in order to show that the NMP polymerization of HEA from PS-SG1 occurred in a well-controlled manner. As shown in Fig. 6.1, $\ln([M]_o/[M])$ vs. time is linear indicating that the concentration of propagating radicals stay constant in the course of the polymerization and therefore the undesired bimolecular termination reactions should be negligible. Indeed, as shown in Fig. 6.1b, the average molar masses of the copolymer increased linearly with the conversion and

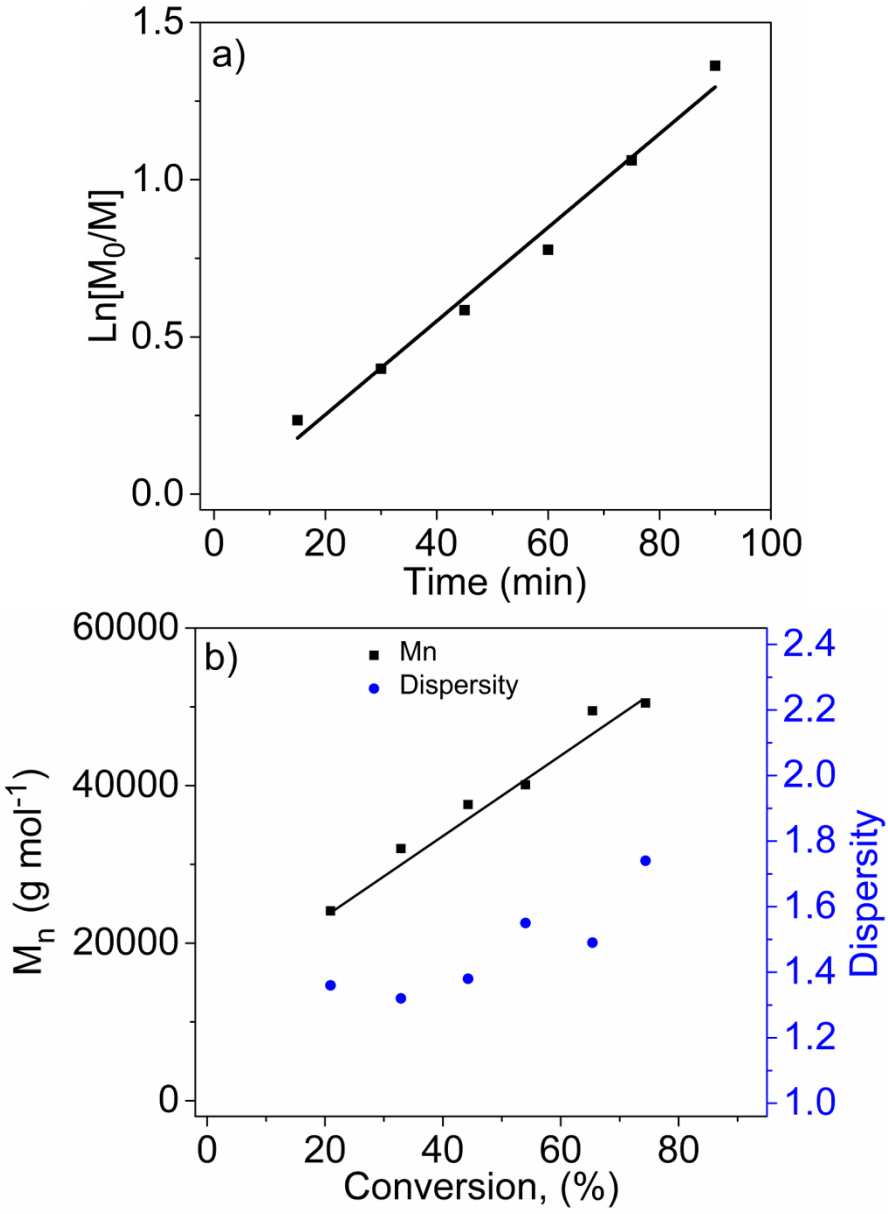

Fig. 6.1 (a) The plot of Ln[Mo/M] vs. time and Mn-and-dispersity vs. conversion for PS-*b*-PHEA synthesized by NMP.

the molar mass distributions stay relatively low with dispersity values below 1.5 until 65 % conversion.

The desired copolymer PS-*b*-PHEA was obtained with a weight fraction of PS within the block copolymer determined by ^{1}H NMR around 10 %, which is normally suitable for morphology of PS nanospheres organized in PHEA matrix. Thus, the average molecular weight M_n estimated by ^{1}H NMR was 62,000 g mol^{-1} and, by SEC, a M_n of 65,200 g mol^{-1} and a dispersity $Đ$ of 1.91 were measured relative to PMMA standards.

The chemical structure and composition of the block copolymer was investigated with ^{1}H NMR and FTIR spectroscopy. Fig. 6.2a shows the ^{1}H NMR spectrum of the PS-SG1

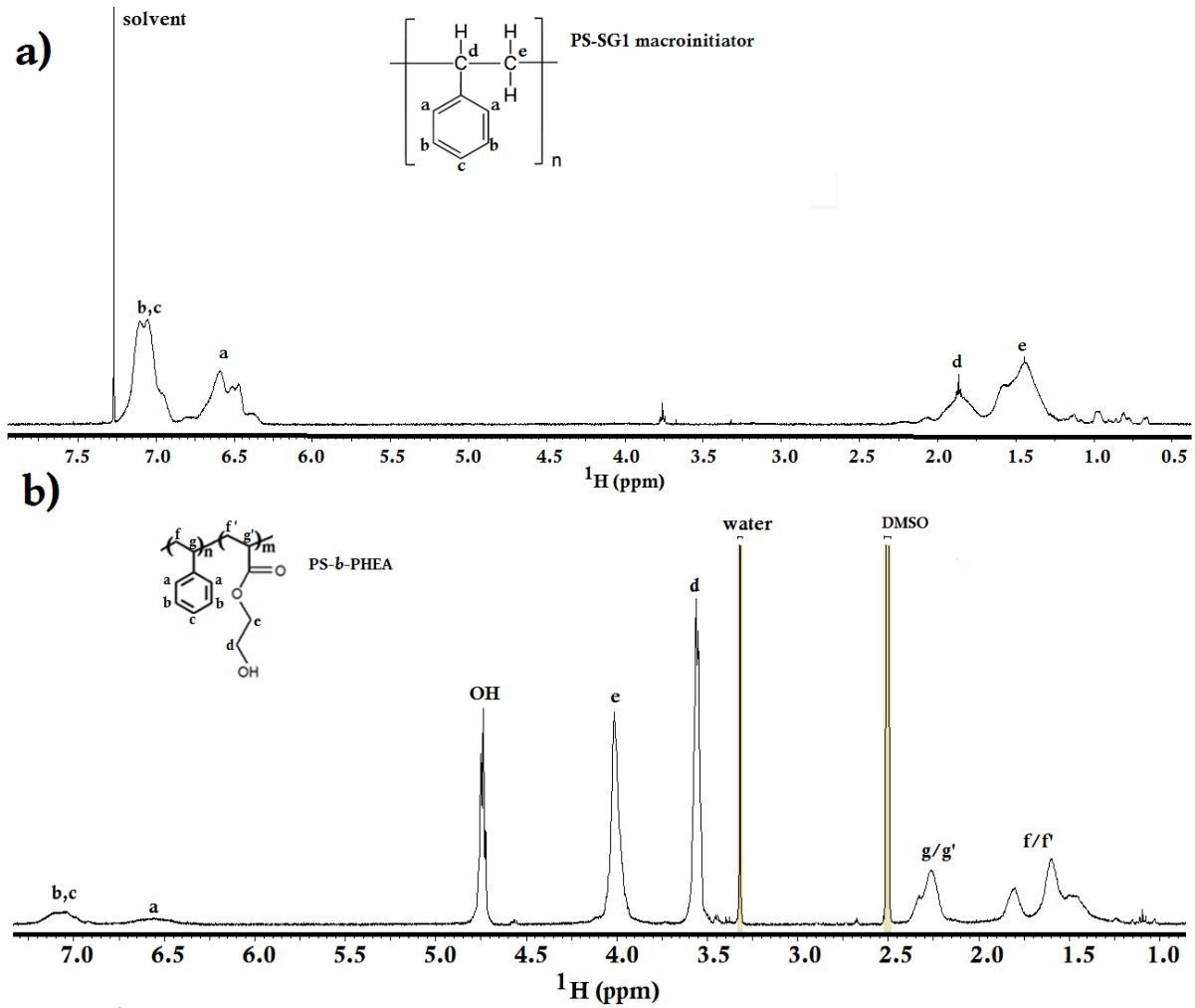

Fig. 6.2 ^{1}H NMR spectrum of (a) PS-SG1 macroinitiator in $CDCl_3$ and (b) PS-*b*-PHEA in DMSO-d_6.

macroinitiator. Signals a and (b, c) at 7.00 and 6.6 ppm, respectively, are attributed to benzene groups of PS. Signals d and e at 1.8 and 1.4 ppm are ascribed to the ethylene (–CH) and methylene ($–CH_2$) protons on the PS chain, respectively.

The ^{1}H NMR spectrum obtained for PS-*b*-PHEA is shown in Fig. 6.2b. The signals at 6.50–7.30 ppm are related to the protons of the aromatic styrene groups (a, b, c). The strong signals at 3.55 and 4.05 ppm are ascribed to the methylene ($–CH_2$) protons of the hydroxyethyl group (d and e) and the signal at 4.8 ppm corresponds to the –OH of hydroxyethyl group. The presence of peaks belonging to styrene and HEA in the ^{1}H NMR spectrum indicated that copolymerization took place [12, 13].

FTIR spectroscopy analysis of PS and PS-*b*-PHEA are shown in Fig. 6.3. In the FTIR spectrum of PS the aromatic (C=C stretching) band produced three peaks at 1602, 1492, and 1451 cm $^{-1}$, the aromatic (C–H) bands was observed at 740 cm $^{-1}$, and aliphatic band (C–H stretching) appeared at 3024 cm^{-1}. The FTIR spectrum of PS-*b*-PHEA exhibit new stretching bands appeared at 3432, 1714, and 1160 cm^{-1}, which were assigned to (–OH),

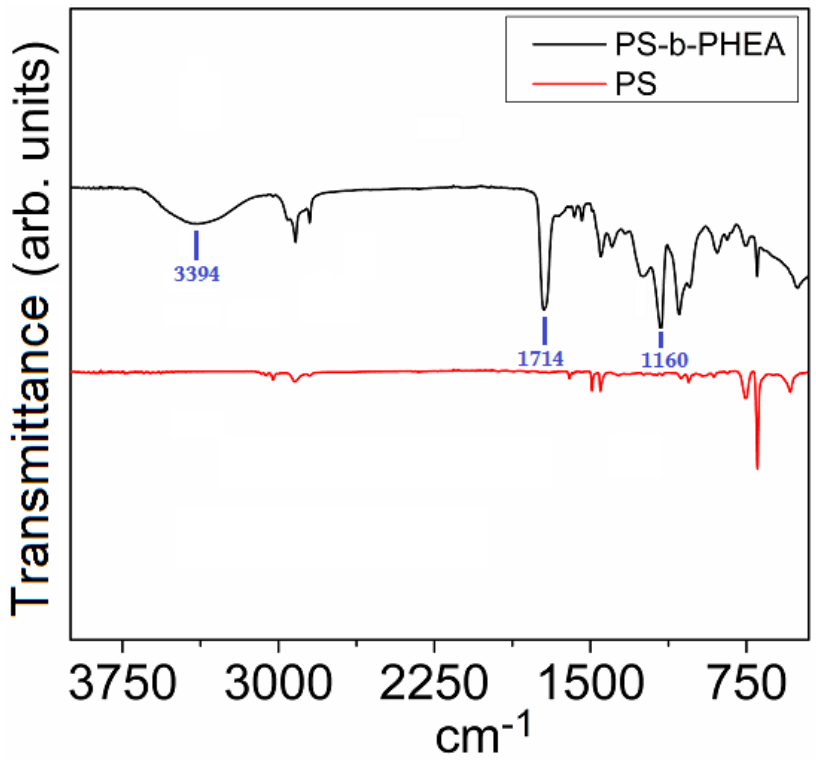

Fig. 6.3 FTIR spectra of PS and PS-*b*-PHEA.

–C=O, and C–O of PHEA, respectively [12, 14]. These FTIR spectroscopy results are clear evidence of the copolymerization of styrene and HEA using NMP.

6.3.2 Electrochemical Characterization

Fig. 6.4 a and b shows the cyclic voltammogram (CV) profile for SnSb without elastomer coating (as-formed SnSb) and SnSb coated with elastomer film (SnSb (PS-*b*-PHEA)) electrode, respectively. The CV curves were recorded at 0.1 mV s^{-1} in potential between 0.01 – 1.75 V vs. Li/Li^+ for the 1^{st}, 2^{nd}, 5^{th}, 10^{th}, 20^{th} and 40^{th} cycle. As described in Chapter 4 and 5, the electrochemical reactivity for both electrodes is confirmed by the presence of five peaks during the first cycle (Fig. 6.4). The broad peak around 0.8 V vs. Li/Li^+ correspond to the alloying of Li^+ with SnSb to form Li_3Sb and Sn and SEI film formation [15-17]. The peak at 0.5 V and 0.6 V vs. Li/Li^+ correspond to the lithiation of Sn to form Li_xSn. Further alloying occurs between 0.3 – 0.1 V vs. Li/Li^+ [18-20]. Five distinct peaks were obtained during the first anodic scan. The peaks at 0.45 V, 0.7 V, 0.75 V, and 0.8 V vs. Li/Li^+ are attributed to the delithiation of Li_xSn alloy to form Sn. The peak at 1 V vs. Li/Li^+ is attributed to the dealloying of Sb to form back SnSb.

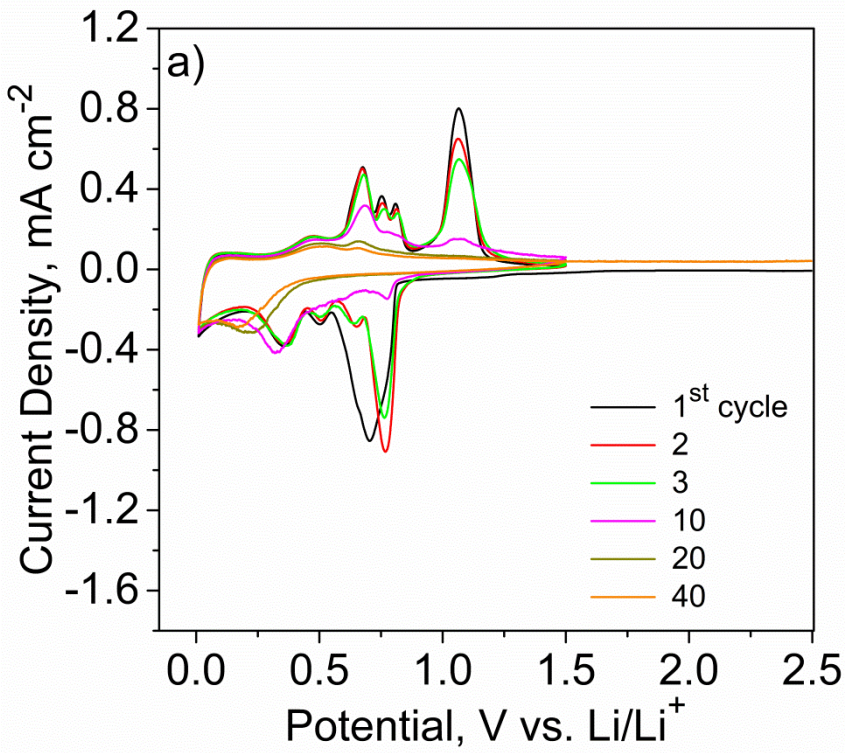

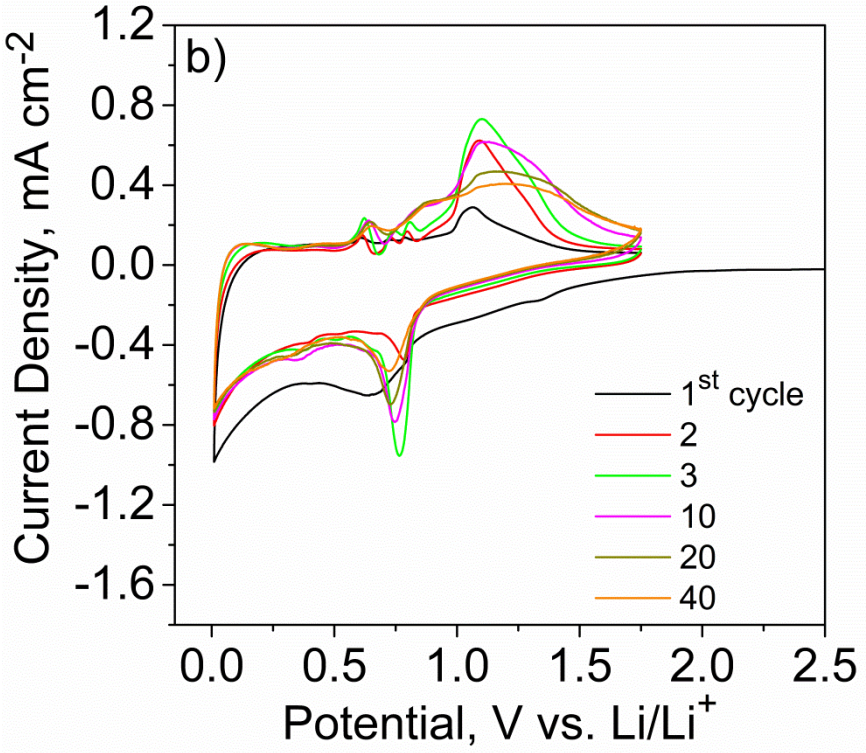

Fig. 6.4 Cyclic voltammograms of (a) as-formed SnSb and (b) SnSb (PS-*b*-PHEA) recorded at scan rate of 0.1 mV s^{-1} over the potential window of 0.01 V – 1.75 V vs. Li/Li^+.

The anodic/cathodic peaks were reversibly obtained for the first five cycles. The peak intensity corresponding to lithium reaction with Sb is diminishing for as-formed SnSb (Fig. 6.4a) suggests in the loss of capacity contribution from Sb. The capacity loss is attributed to the loss of the active material and electrical contact as the result of large volume change during alloying/dealloying mechanism and the formation of SEI film. In contrast, the alloying/dealloying peaks for SnSb (PS-*b*-PHEA) (Fig. 6.4b) are observed up to 40 cycles. The stability of the peaks is attributed to the thermoplastic elastomer coating film. PS-*b*-PHEA is stretchable and can tolerate a mechanical stress caused by the large volume expansion without breakage (Scheme 2). Thus, results in stable mechanical and electrical connections among the SnSb particles during cycling.

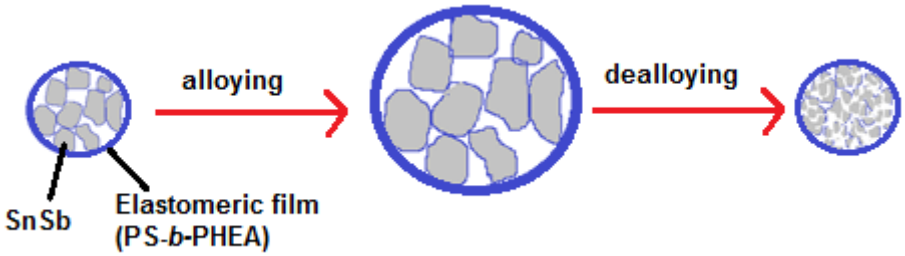

Scheme 6.2. The stretchable behavior of the PS-*b*-PHEA elastomer coating during alloying/de-alloying mechanism of SnSb particles.

The electrochemical performance of SnSb (PS-*b*-PHEA) was evaluated using deep charge/discharge galvanostatic cycling (Fig. 6.5). Fig. 6.5a shows the discharge capacity vs. cycle number for as-formed SnSb and SnSb (PS-*b*-PHEA) cycled at C/20 in the potential window of 0.01 – 1.75 V vs. Li/Li^+. It can be seen clearly that the SnSb (PS-*b*-PHEA) has superior cyclability than as-formed SnSb with reversible capacity of 700 mAh g^{-1} after 65 cycles. The stable capacity obtained is attributed to the PS-*b*-PHEA film ability to stretch without cracking and formation of stable SEI film. The capacity fading obtained for as-formed SnSb is attributed to the large volume change leading to the loss

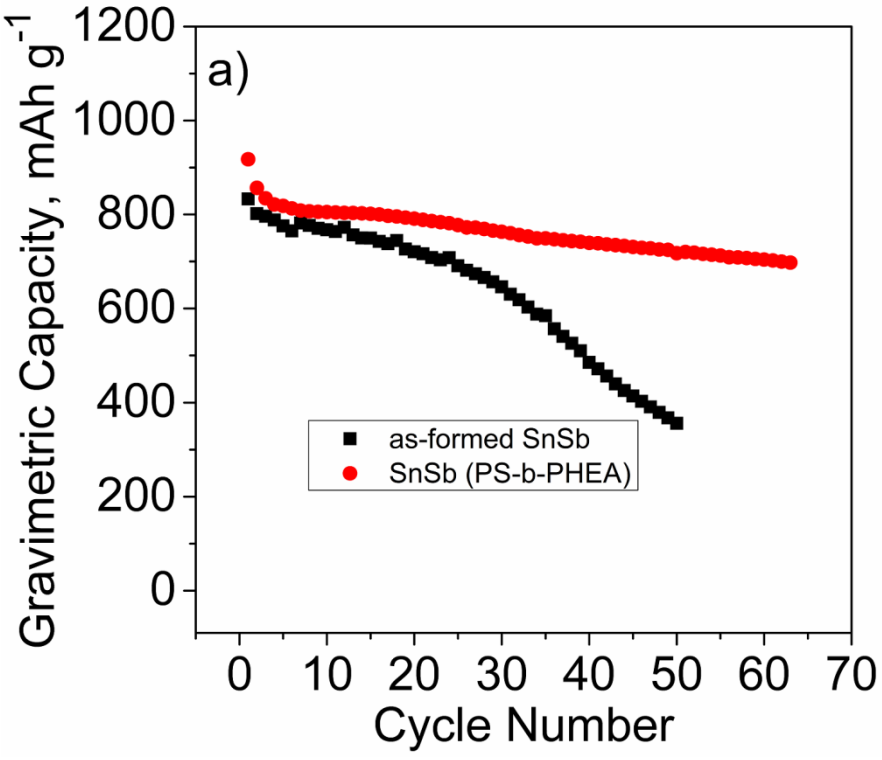

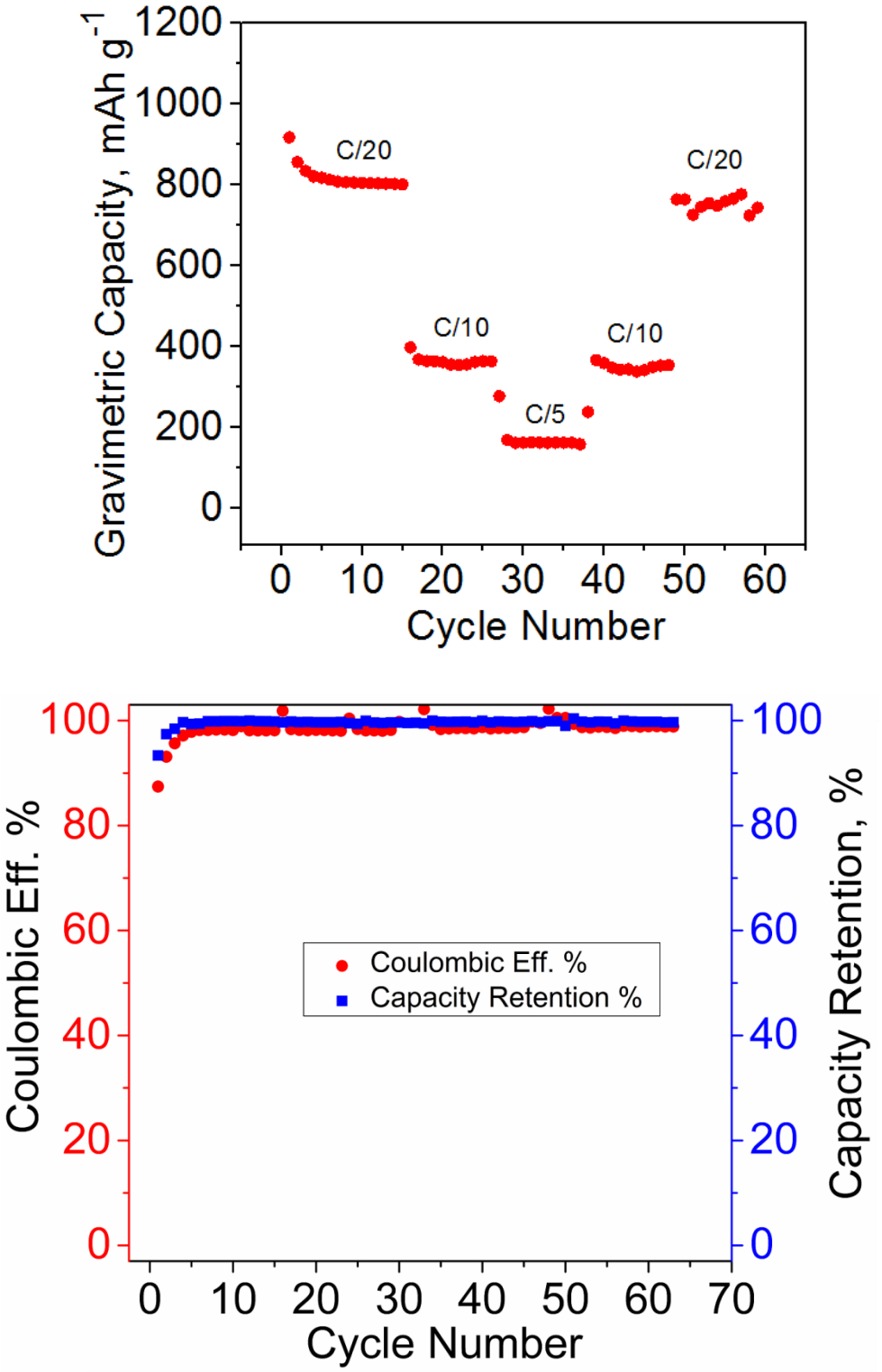

Fig. 6.5 (a) Cycle stability for as-formed SnSb and SnSb (PS-*b*-PHEA) at C/20. (b) Cycling performance at multiple C-rates and (c) coulombic efficiency-and-capacity retention vs. cycle number at C/20 for SnSb (PS-*b*-PHEA).

of electrical contact and failure in electrode mechanical stability. Moreover, the capacity is also influenced by the continuous formation of thick SEI film on the newly created electrode surface.

To study the operational stability of SnSb (PS-*b*-PHEA), the cycling life performance has been studied at multiple C-rates, Fig. 6.5b. A stable gravimetric capacity of 800 mAh g^{-1}, 368 mAh g^{-1}, and 170 mAh g^{-1} is obtained at C/20, C/10, and C/5, respectively. When the kinetics is subsequently restored to C/10 and C/20 a capacity values of 344 mAh g^{-1} and 770 mAh g^{-1} is obtained, respectively. The excellent rate capability is attributed to PS-*b*-PHEA film which ensures fast lithium-ion transfer while keeping the mechanical stability of the SnSb micro-particles.

Coulombic efficiency (CE) and capacity retention are important criteria for evaluating the electrochemical performance of electrodes for LIBs [5, 21, 22]. The CE obtained at the first cycle was 87 % and in later cycles reached more than 98 % while discharge capacity retention of more than 95 % was obtained (Fig. 6.5c). These values indicate a relatively stable SEI formation on the surface of the electrode even after 65 cycles.

To provide further evidence for the contribution of elastomer film on the electrochemical performances, the morphology of the electrode with cycling was monitored using SEM. Fig. 6.6 a and b shows the as-formed SnSb electrode and the SnSb electrode (65 µm) covered with a thin layer (2 µm) of the conductive elastomer film, respectively, before cycling. The SnSb (PS-*b*-PHEA) displayed a flat and smooth morphology (Fig. 6.6b). After electrochemical cycling (50 cycles at a rate of C/20), the SnSb (PS-*b*-PHEA) electrode surface became rough containing small cracks and lumps (Fig. 6.6c). This is caused by the underlying SnSb being deformed and continuous Sn agglomeration when subjected to repeated volume expansion and contraction processes. No significant cracks or delaminations were observed. For comparison, the SEM image of as-formed SnSb after 50 cycles is shown in Fig. 6.6d. The electrode surface is characterized by large cracks and pits containing different sizes of particles. This is due

to the repeated volume change, which results in the pulverization of the SnSb particles, and thus, poor cycling stability (Fig. 6.5 a).

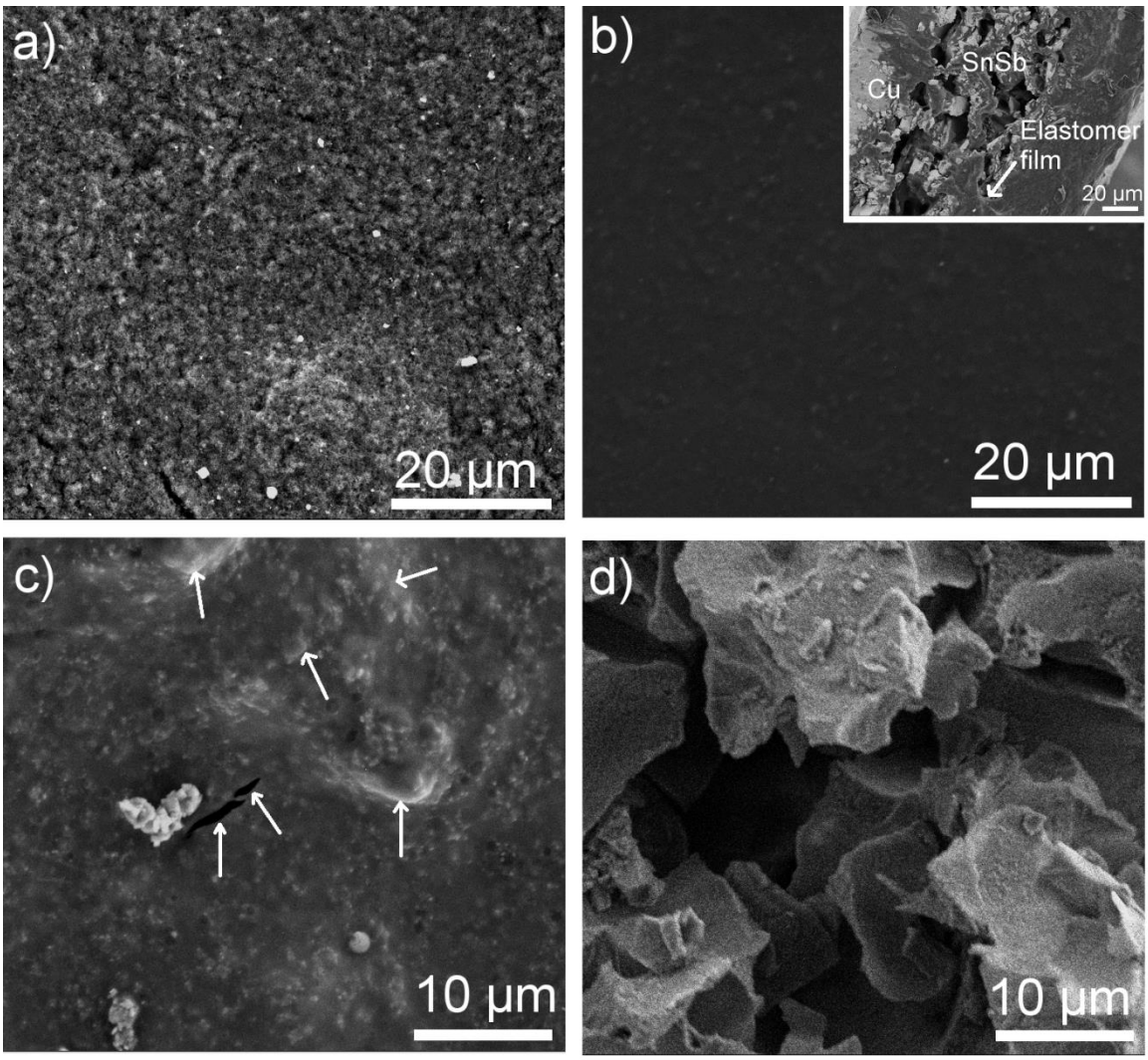

Fig. 6.6 SEM image of (a) SnSb and (b) SnSb (PS-b-PHEA) before cycling. Inset: cross-sectional SEM image of SnSb (PS-b-PHEA) electrode. (c) SnSb (PS-b-PHEA) and SnSb electrode morphology after 50 cycles at C/20.

6.4 Conclusion

In this work, we investigate the enhanced electrochemical performance of SnSb electrode coated with thin thermoplastic elastomer film (PS-*b*-PHEA). The excellent cycle life performance and rate capability obtained is attributed to the high failure strain

characteristics of the PS-*b*-PHEA elastomer film. The elastomer film can accommodate the large volume expansion during lithium alloying/dealloying reaction with SnSb and control the SEI growth. As a result the SnSb electrode is mechanically stable for at least 50 cycles. Moreover, the use of elastomer polymer coating can extend to other high capacity electrode materials that suffer from large volume changes and unstable SEI formation, such as Si, during cycling.

6.5 References

[1] H.A. Wilhelm, C. Marino, A. Darwiche, L. Monconduit, B. Lestriez, Significant electrochemical performance improvement of TiSnSb as anode material for Li-ion batteries with composite electrode formulation and the use of VC and FEC electrolyte additives, Electrochem. Commun., 24 (2012) 89-92.

[2] S.S. Zhang, A review on electrolyte additives for lithium-ion batteries, J. Power Sources, 162 (2006) 1379-1394.

[3] C. Xu, F. Lindgren, B. Philippe, M. Gorgoi, F. Björefors, K. Edström, T.r. Gustafsson, Improved performance of the silicon anode for Li-ion batteries: understanding the surface modification mechanism of fluoroethylene carbonate as an effective electrolyte additive, Chem. Mater., 27 (2015) 2591-2599.

[4] K. Abe, H. Yoshitake, T. Kitakura, T. Hattori, H. Wang, M. Yoshio, Additives-containing functional electrolytes for suppressing electrolyte decomposition in lithium-ion batteries, Electrochim. Acta, 49 (2004) 4613-4622.

[5] C. Wang, H. Wu, Z. Chen, M.T. McDowell, Y. Cui, Z. Bao, Self-healing chemistry enables the stable operation of silicon microparticle anodes for high-energy lithium-ion batteries, Nat. Chem., 5 (2013) 1042-1048.

[6] H. Sopha, G.D. Salian, R. Zazpe, J. Prikryl, L. Hromadko, T. Djenizian, J.M. Macak, ALD Al2O3-Coated TiO2 Nanotube Layers as Anodes for Lithium-Ion Batteries, ACS Omega, 2 (2017) 2749-2756.

[7] H. Wu, G. Yu, L. Pan, N. Liu, M.T. McDowell, Z. Bao, Y. Cui, Stable Li-ion battery anodes by in-situ polymerization of conducting hydrogel to conformally coat silicon nanoparticles, Nature communications, 4 (2013) 1943.

[8] L.J. Fu, H. Liu, C. Li, Y.P. Wu, E. Rahm, R. Holze, H.Q. Wu, Surface modifications of electrode materials for lithium ion batteries, Solid State Sci., 8 (2006) 113-128.

[9] P. Yu, J.A. Ritter, R.E. White, B.N. Popov, Ni-Composite Microencapsulated Graphite as the Negative Electrode in Lithium-Ion Batteries I. Initial Irreversible Capacity Study, J. Electrochem. Soc., 147 (2000) 1280-1285.

[10] M. Huang, L. Li, S. Zheng, Mesoporous silica with block copolymer templates: Modulation of porosity via block copolymer reaction with silica, Microporous and Mesoporous Mater., 225 (2016) 9-25.
[11] D. Benoit, S. Grimaldi, S. Robin, J.-P. Finet, P. Tordo, Y. Gnanou, Kinetics and mechanism of controlled free-radical polymerization of styrene and n-butyl acrylate in the presence of an acyclic β-phosphonylated nitroxide, J. Am. Chem. Soc., 122 (2000) 5929-5939.
[12] N. Greesh, R. Sanderson, P. Hartmann, Preparation of poly (styrene-b-2-hydroxyethyl acrylate) block copolymer using reverse iodine transfer polymerization, J. Appl. Polym. Sci., 126 (2012) 1773-1783.
[13] J.K. Choi, D.K. Lee, Y.W. Kim, B.R. Min, J.H. Kim, Composite polymer electrolyte membranes comprising triblock copolymer and heteropolyacid for fuel cell applications, J. Polym. Sci. Part B Polym. Phys., 46 (2008) 691-701.
[14] E. Vargün, A. Usanmaz, Polymerization of 2-hydroxyethyl acrylate in bulk and solution by chemical initiator and by ATRP method, Journal of Polymer Science Part A: Polymer Chemistry, 43 (2005) 3957-3965.
[15] J. Yang, M. Wachtler, M. Winter, J.O. Besenhard, Sub-Microcrystalline Sn and Sn-SnSb Powders as Lithium Storage Materials for Lithium-Ion Batteries, Electrochem. Solid-State Lett., 2 (1999) 161-163.
[16] F.J. Fernández-Madrigal, P. Lavela, C.P. Vicente, J.L. Tirado, J.C. Jumas, J. Olivier-Fourcade, X-ray diffraction, 7Li MAS NMR spectroscopy, and 119Sn Mössbauer spectroscopy study of SnSb-based electrode materials, Chem. Mater., 14 (2002) 2962-2968.
[17] L. Aldon, A. Garcia, J. Olivier-Fourcade, J.-C. Jumas, F.J. Fernández-Madrigal, P. Lavela, C.P. Vicente, J.L. Tirado, Lithium insertion mechanism in Sb-based electrode materials from 121Sb Mössbauer spectrometry, J. Power Sources, 119 (2003) 585-590.
[18] P. Antitomaso, B. Fraisse, L. Stievano, S. Biscaglia, D. Aymé-Perrot, P. Girard, M.T. Sougrati, L. Monconduit, SnSb electrodes for Li-ion batteries: the electrochemical mechanism and capacity fading origins elucidated by using operando techniques, J. Mater. Chem. A, 5 (2017) 6546-6555.

[19] H. Zhao, C. Yin, H. Guo, W. Qiu, Microcrystalline SnSb alloy powder as lithium storage material for rechargeable lithium-ion batteries, Electrochem. Solid-State Lett., 9 (2006) A281-A284.

[20] H. Mukaibo, T. Osaka, P. Reale, S. Panero, B. Scrosati, M. Wachtler, Optimized Sn/SnSb lithium storage materials, J. Power Sources, 132 (2004) 225-228.

[21] J.-M. Tarascon, M. Armand, Issues and challenges facing rechargeable lithium batteries, Nature, 414 (2001) 359-367.

[22] H. Wu, G. Chan, J.W. Choi, I. Ryu, Y. Yao, M.T. McDowell, S.W. Lee, A. Jackson, Y. Yang, L. Hu, Y. Cui, Stable cycling of double-walled silicon nanotube battery anodes through solid-electrolyte interphase control, Nat Nano, 7 (2012) 310-315.

Publications

1. A.T. Tesfaye, R. Gonzalez, J.L. Coffer, T. Djenizian, Porous silicon nanotube arrays as anode material for Li-ion batteries, ACS Appl. Mater. Interfaces, 7 (2015) 20495-20498.
2. A.T. Tesfaye, O. Mashtalir, M. Naguib, M.W. Barsoum, Y. Gogotsi, T. Djenizian, Anodized Ti_3SiC_2 as an anode material for Li-ion microbatteries, ACS Appl. Mater. Interfaces, 8 (2016) 16670-16676.
3. A.T. Tesfaye, Y. Gogotsi, T. Djenizian, Tailoring the morphological properties of anodized Ti_3SiC_2 for better power density of Li-ion microbatteries, Electrochem. Commun., 81 (2017) 29-33.
4. A.T. Tesfaye, Y.D. Yücel, M.K.S. Barr, L. Santinacci, F. Vacandio, F. Dumur, S. Maria, L. Monconduit, T. Djenizian, The electrochemical behavior of SnSb as an anode for Li-ion batteries studied by electrochemical impedance spectroscopy and electron microscopy, Electrochimi. Acta (Accepted).